

The solubility of sulfur and chlorine in H₂O-
bearing dacites of Krakatau and basalts of Mt.
Etna

Von der Naturwissenschaftlichen Fakultät
der Gottfried Wilhelm Leibniz Universität Hannover

zur Erlangung des Grades

DOKTOR DER NATURWISSENSCHAFTEN

Dr. rer. nat.

genehmigte Dissertation

von

Dipl.-Geowiss. Oliver Beermann

geboren am 28.01.1978 in Immenstadt/Allgäu

2010

Referent: Prof. Dr. Marcus Nowak (Eberhard Karls Universität Tübingen)

Koreferent: Prof. Dr. François Holtz (Leibniz Universität Hannover)

Mitglieder der Prüfungskommission:

Prof. Dr. Andrea Hampel (Vorsitzende)

Prof. Dr. Marcus Nowak

Prof. Dr. François Holtz

Tag der Promotion: 07.07.2010

Erklärung zur Dissertation

Hiermit erkläre ich, dass die Dissertation „The solubility of sulfur and chlorine in H₂O-bearing dacites of Krakatau and basalts of Mt.Etna” selbstständig verfasst und alle benutzten Hilfsmittel, sowie evtl. zur Hilfestellung herangezogene Institutionen vollständig angegeben wurden.

Die Dissertation wurde nicht schon als Diplom- oder ähnliche Prüfungsarbeit verwendet.

Hannover, den 07.07.2010

Oliver Beermann

Abstract

The sulfur concentration at FeS- and anhydrite-saturation was determined in hydrous basaltic melts (primitive Etna basalt of the 2001-2002 eruption) at $T = 1050\text{-}1250^\circ\text{C}$, $P = 200$ MPa and $f\text{O}_2$ ranging between FMQ and FMQ+2.2. Experiments at 1050°C were performed by using Au sample containers. Since sulfur is highly corrosive to noble metal commonly used as sample container material (eg., AuPd, Pt) for hydrous experiments at $T > 1050^\circ\text{C}$, a double capsule technique was developed for conduction of experiments at $1150\text{-}1250^\circ\text{C}$. Therefore an OL sample container closed with an OL piston (made of single crystal San Carlos olivine) was embed in an AuPd-capsule, which closed the experimental system. Due to Fe/Mg exchange reactions with the OL container/piston, the MgO content of the product melts increase almost linear as a function of temperature from ~ 5.5 wt.% MgO at 1050°C to ~ 13.5 wt.% MgO at 1250°C , allowing the simulation of temperature evolution for an olivine-saturated basaltic melt.

The precipitation of FeS was observed at FMQ to FMQ+0.3 and anhydrite precipitated at FMQ+1.4 to FMQ+2.2. The S concentration in the melt increases almost linear with temperature from 0.12 ± 0.01 to 0.39 ± 0.02 wt.% S at FeS-saturation and from 0.74 ± 0.01 to 1.08 ± 0.04 wt.% S at anhydrite-saturation, if T increases from $1050\text{-}1250^\circ\text{C}$. When $f\text{O}_2$ decreases from FMQ+1 to FMQ+0.5 the S solubility decreases for ~ 25 rel.% at high temperatures ($1150\text{-}1250^\circ\text{C}$) and for ~ 35 rel.% at 1050°C . When $f\text{O}_2$ increases from FMQ+1 to FMQ+1.5 the S solubility increases for about 30 rel.% at high temperatures ($1150\text{-}1250^\circ\text{C}$) and for about 45 rel.% at 1050°C . The fact that the increase in S solubility is higher by changing $f\text{O}_2$ from FMQ+1 to more oxidizing can be explained by the increase of sulfate species and their high contribution to the total S solubility.

A simple empirical model for the estimation of magmatic temperatures, the sulfur solubility and $f\text{O}_2$ in olivine-saturated basaltic magmas was designed by using the melt MgO content as a temperature index. Applied to natural melts of Mt.Etna representing $f\text{O}_2 \sim \text{FMQ}+1$

(Métrich & Clochiatti, 1989) the magmatic temperature and the sulfur solubility at FMQ+1 was estimated to be ~1025-1125°C and ~0.25-0.4 wt.% S for juvenile S-rich melts and ~1025°C and ≤ ~0.1 wt.% S for partially degassed melts. Since juvenile S-rich melts representing lower T (~1025-1050°C) contain up to 0.35 wt.% S and partly degassed melts (T < ~1050°C) contain ≤ ~0.2 wt.% S the magmatic system of Mt.Etna possibly reflects slightly higher fO_2 than FMQ+1.

Fluid saturated sulphur- and chlorine partitioning experiments were conducted at 1050°C between Cl-H₂O- and Cl-S-H₂O fluid and primitive basaltic melts of Mt.Etna at 100 and 200 MPa and ~FMQ+0.5 to FMQ+4 and between Cl-H₂O- or S-H₂O fluid and dacitic melts of Krakatau at 200 MPa and ~FMQ+0.5. At the investigated range of system composition sulfur and chlorine show a non-ideal partitioning-behavior.

In Cl-free/poor systems the sulfur content at FeS-saturation (FMQ+0.5) was determined to be 0.04 wt.% S in the dacitic melts and range between 0.09 ± 0.01 to 0.13 ± 0.01 wt.% S in the basaltic melts. The S content at anhydrite saturation in the Cl-poor basaltic melt is 0.85 ± 0.02 wt.% S at FMQ+2 and 0.74 ± 0.01 wt.% S at FMQ+4 and 200 MPa and 0.60 ± 0.01 wt.% S at FMQ+2.5 and 0.64 ± 0.01 wt.% S at FMQ+4 and 100 MPa.

The maximum chlorine concentration, observed at highest Cl content in the system (~3-3.6 wt.% Cl) in the sulfate-poor and S-free melts, was determined to be 2.26 ± 0.02 wt.% Cl at 200 MPa and 2.20 ± 0.04 wt.% Cl at 100 MPa in the basaltic melts and 1.42 ± 0.03 wt.% in the dacitic melts (at 200 MPa). The sulfur partitioning coefficients between fluid and melt (K_d^S) in the basaltic melt systems range between ~1 and 96 ± 16 at 200 MPa and ~1 to 73 ± 12 at 100 MPa in sulfate dominated systems (FMQ+2 to FMQ+4) and ~164 ± 16 to 236 ± 32 at 200 MPa in the sulfide dominated system (FMQ+0.5). In the dacitic melt systems K_d^S range between 532 ± 38 and 745 ± 47 at FMQ+0.5. These results are in contrast to those of Keppler (2010) obtaining constant K_d^S of sulfur in haplogranitic melts (at fixed P-T-X- and redox conditions), indicating an ideal partitioning-behavior of sulfur in such simplified melt system.

The partitioning coefficients of chlorine (K_d^{Cl}) range between ~ 0 and 19 ± 2 in the basaltic melt systems for all P and fO_2 investigated and between ~ 0 and 34 ± 5 in the dacitic melt systems.

Mutual effects of chlorine and sulfur were observed in the sulfate-dominated systems ($FMQ \geq +2$). The addition of chlorine decreases the S content in the melt for about 0.1-0.2 wt.% at highest Cl content in the system (3-3.6 wt.% Cl), where the maximum decrease of about 23-27 rel.% is observed at anhydrite-saturation and $FMQ+4$. The chlorine concentration in the melt decreases, if the sulfur content in the system is higher than 0.5 wt.% S, where the maximum decrease of ~ 35 rel.% is observed at high S- and Cl contents in the system (~ 2 wt.% S and ~ 3 wt.% Cl) and high fO_2 ($FMQ+4$).

In the sulfate-bearing systems chlorine significantly decreases the CaO concentration (and to a minor content Na_2O and K_2O) in the melt, which can be explained by the increasing solubility of $CaSO_4$ in Cl-bearing aqueous fluids as quantified by Newton & Manning (2005) and Webster et al. (2009). An enrichment of Ca^{2+} in the fluid is indicated by the observed strong parabolic increase in Cl melt content with increasing Cl concentration in the system, being more pronounced compared to S-free or sulfate-poor systems.

The S/Cl ratio in the fluid was correlated to the S concentration in the coexisting melt with respect to a fixed Cl melt content, being almost constant at 0.15-0.2 wt.% Cl in the melts of Mt.Etna. This correlation was applied to in situ measured S/Cl ratios of emitted gases at Mt.Etna's 2002-2003 eruption (Aiuppa et al., 2004). S/Cl ratios during passive degassing of S/Cl ~ 7 require a melt S content of ~ 0.3 wt.% S, which is similar to that of juvenile S-rich melts. A S/Cl ratio of $\sim 0.4-2$ representing higher explosive stages, require a melt S content of $\sim 0.1-0.2$ wt.% S, which is similar to that of the partly degassed melt melts (e.g. Spilliaert et al., 2006a, 2006b).

Keywords: Sulfur, Chlorine, Volatile partitioning, Basaltic melt, Magma degassing

Zusammenfassung

Die Schwefelkonzentrationen in wasserhaltigen basaltischen Schmelzen (primitiver Basalt des Etna der Eruption 2001-2002) wurden unter Sättigung von FeS und Anhydrit experimentell bei $T = 1050\text{-}1250^\circ\text{C}$, $P = 200\text{ MPa}$ und $f\text{O}_2$ von FMQ bis FMQ+2.2 bestimmt. Für alle 1050°C Experimente wurde Gold (Au) als Kapselmaterial verwendet. Aufgrund der hohen Korrosivität von Schwefel gegenüber den meisten als Kapselmaterial für wasserhaltige Experimente oberhalb 1050°C verwendeten Edelmetallen (z.B., AuPd, Pt), wurde eine Doppelkapsel-Technik in Experimenten bei $1150\text{-}1250^\circ\text{C}$ angewendet und weiterentwickelt. Dabei dienten OL-Container., verschlossen mit einem OL-Stempel (hergestellt aus San Carlos Olivin Einkristallen) als Probenbehälter, die in AuPd-Kapseln eingeschweißt wurden. Aufgrund von Fe/Mg-Austauschreaktionen zwischen Schmelze und OL-Container/-Stempel, steigt der MgO-Gehalt der Schmelzen annähernd linear mit der Temperatur von $\sim 5.5\text{ Gew.}\%$ MgO bei 1050°C bis $\sim 13.5\text{ Gew.}\%$ MgO bei 1250°C an. Hierdurch können Temperaturänderungen in OL-gesättigten Schmelzen simuliert werden. FeS-Sättigung der Schmelze wurde bei FMQ bis FMQ+0.3 und Anhydrit-Sättigung der Schmelze bei FMQ+1.4 to FMQ+2.2 beobachtet. Die Schwefelkonzentration der Schmelze steigt annähernd linear mit der Temperatur von 0.12 ± 0.01 bis $0.39 \pm 0.02\text{ Gew.}\%$ S bei FeS-Sättigung und von 0.74 ± 0.01 bis $1.08 \pm 0.04\text{ Gew.}\%$ S bei Anhydrit-Sättigung im T-Intervall von $1050\text{-}1250^\circ\text{C}$ an.

Es wurde die Änderung der Schwefelkonzentration unter um $\pm 0.5\text{ log}$ Einheiten variierender $f\text{O}_2$ ausgehend von FMQ+1 abgeschätzt. Eine Verringerung der $f\text{O}_2$ von FMQ+1 auf FMQ+0.5 bewirkt eine Verringerung der Schwefellöslichkeit von $\sim 25\text{ rel.}\%$ bei hohen Temperaturen ($1150\text{-}1250^\circ\text{C}$) und $\sim 35\text{ rel.}\%$ bei 1050°C . Ein Anstieg der $f\text{O}_2$ von FMQ+1 auf FMQ+1.5 erhöht die Schwefellöslichkeit um $\sim 30\text{ rel.}\%$ bei hohen Temperaturen ($1150\text{-}1250^\circ\text{C}$) um $\sim 45\text{ rel.}\%$ bei 1050°C . Die größere Änderung der Schwefellöslichkeit ausgehend von

FMQ+1 hin zu oxidierenderen Bedingungen kann durch die Zunahme von Sulfat-Spezies und deren großen Beitrag zur Schwefellöslichkeit erklärt werden (Jugo et al., 2009, subm.).

Es wurde ein vereinfachtes empirisches Modell erstellt, um magmatische Temperaturen, die Schwefellöslichkeit und die fO_2 in olivingsättigten basaltischen Systemen abzuschätzen. Hierzu wurde der MgO-Gehalt der Schmelze als Temperaturindex benutzt. Die Anwendung dieses Modells auf die natürlichen, relativ oxidierenden Schmelzen des Etna (FMQ+1, Métrich & Clochiatti, 1989) ergibt Temperaturen und Schwefellösungen von ~ 1025 - 1125°C und ~ 0.25 bzw. 0.4 Gew.% S für die juvenilen schwefelreichen Schmelzen, sowie $\sim 1025^\circ\text{C}$ und $\leq \sim 0.1$ Gew.% S für teilentgaste Schmelzen. Aufgrund der hohen Schwefelkonzentrationen natürlicher Schmelzen des Etna bis zu 0.35 Gew.% S bei ~ 1025 - 1050°C und bis zu 0.2 Gew.% S bei ~ 1025 - 1050°C , kann für das magmatische System des Etna eine höhere fO_2 als FMQ+1 angenommen werden.

Fluidgesättigte Schwefel- und Chlor-Verteilungsexperimente bei 1050°C wurden zwischen Cl-H₂O- bzw. Cl-S-H₂O-Fluid und primitiver Schmelze des Etna Basalt bei 100 und 200 MPa und \sim FMQ+0.5 bis FMQ+4 sowie zwischen dazitischer Schmelze des Krakatau und Cl-H₂O- bzw. S-H₂O-Fluid bei 200 MPa und \sim FMQ+0.5 durchgeführt. Die Verteilung von Schwefel und Chlor zwischen Fluid und Schmelze zeigt ein nicht lineares Verhalten.

Die S-Konzentration bei FeS-Sättigung (FMQ+0.5) in Cl-freien/-armen Systemen wurde auf 0.04 Gew.% S in dazitischen Schmelzen und 0.09 ± 0.01 bis 0.13 ± 0.01 Gew.% S in basaltischen Schmelzen bestimmt. Die S-Konzentration bei Anhydrit-Sättigung in Cl-armen basaltischen Schmelzen ergibt Gehalte von 0.85 ± 0.02 Gew.% S bei FMQ+2 und 0.74 ± 0.01 Gew.% S bei FMQ+4 und 200 MPa, sowie 0.60 ± 0.01 Gew.% S bei FMQ+2.5 und 0.64 ± 0.01 Gew.% S bei FMQ+4 und 100 MPa.

Die maximalen Cl-Konzentrationen von 2.26 ± 0.02 Gew.% Cl bei 200 MPa und 2.20 ± 0.04 Gew.% Cl bei 100 MPa in basaltischen Schmelzen und 1.42 ± 0.03 Gew.% in dazitischen

Schmelzen (200 MPa) wurden unter geringen Sulfatkonzentrationen in der Schmelze oder in S-freien Schmelzen bei den höchsten untersuchten Cl-Gehalten im System (~3-3.6 Gew.% Cl) beobachtet. Der Verteilungskoeffizient von Schwefel (K_d^S) in basaltischen Systemen variiert zwischen ~1 bis 96 ± 16 bei 200 MPa und zwischen ~1 bis 73 ± 12 bei 100 MPa in Sulfatreichen Systemen (FMQ+2 to FMQ+4) und von ~164 ± 16 bis 236 ± 32 bei 200 MPa in Sulfidreichen Systemen (FMQ+0.5). In dazitischen Systemen variiert K_d^S zwischen 532 ± 38 and 745 ± 47 bei FMQ+0.5. Diese Ergebnisse stehen im Gegensatz zu den von Keppler (2010) erhaltenen konstanten Werten für K_d^S (bei konstanten P-T-X- und Redoxbedingungen) in haplogranitischen Schmelzen, was auf ein ideales Verteilungsverhalten von Schwefel in einem solchen vereinfachten System hinweist.

Der Verteilungskoeffizient von Chlor (K_d^{Cl}) wurde auf ~0 bis 19 ± 2 in basaltischen Systemen für alle untersuchte P- und fO_2 -Bedingungen und auf ~0 bis 34 ± 5 in dazitischen Systemen bestimmt.

Eine gegenseitige Beeinflussung von Chlor und Schwefel wurde ausschließlich in Sulfatreichen Systemen (FMQ \geq +2) beobachtet. Hier führt die Zugabe von 3-3.6 Gew.% Cl in das System zu einer Abnahme der in der Schmelze gelöstem Schwefel von 0.1-0.2 Gew.% S, bei einer maximalen Abnahme von ~23-27 rel.% unter Anhydrit-Sättigung bei FMQ+4.

Schwefel (als Sulfat) beeinflusst die Konzentration von Chlor in der Schmelze bei >0.5 Gew.% S im System. Die maximale Abnahme der Cl-Konzentration von ~35 rel.% wurde bei hohen S- und Cl-Gehalten im System (~2 Gew.% S and ~3 Gew.% Cl) und hoher fO_2 (FMQ+4) beobachtet.

In Sulfatreichen Systemen führt die Zugabe von Chlor zu einer signifikanten Abnahme der Gehalte an CaO (in geringerem Maße auch Na₂O und K₂O) der Schmelze, was mit erhöhter Löslichkeit von CaSO₄ in chlorhaltigen wässrigen Lösungen erklärt werden kann, wie z.B. von Newton & Manning (2005) und Webster et al. (2009a) quantitativ bestimmt. Es wird angenommen, dass ein erhöhter Ca²⁺-Gehalt im Fluid zu einem verstärkt ausgeprägt

parabolischem Anstieg der Cl-Konzentration in der Schmelze mit steigender Cl-Konzentration im System, verglichen zu S-freien oder Sulfat-armen Systemen, führt.

Das S/Cl-Verhältnis im Fluid wurde mit der S-Konzentration der koexistierenden Schmelze korreliert, unter Berücksichtigung eines konstanten Cl-Gehaltes in der Schmelze, zutreffend für natürliche Schmelzen des Etna (0.15-0.2 Gew.% Cl). Angewendet auf in situ gemessene S/Cl-Verhältnisse der während der 2002-2003 Eruption des Etna freigesetzten Gase (Aiuppa et al., 2004) ergibt sich für Phasen passiver Entgasung ($S/Cl \sim 7$) eine S-Konzentration der Schmelze von ~ 0.3 Gew.%, übereinstimmend mit dem S-Gehalt juveniler S-reicher Schmelzen, und für Phasen höherer Explosivität ($S/Cl \sim 0.4-2$) eine S-Konzentration der Schmelze von $\sim 0.1-0.2$ Gew.% S, übereinstimmend mit dem S-Gehalt teilentgaster Schmelzen (Spilliaert et al., 2006a, 2006b).

Schlagerworte: Schwefel, Chlor, Volatile, Basalt, magmatische Entgasung

Danksagung

Ich möchte mich bei Prof. Dr. Marcus Nowak für die Betreuung meiner Arbeit bedanken. Weiterhin danke ich vor allem Dr. Roman Botcharnikov für die immense fachliche Unterstützung.

Einen ganz besonderen Dank an Otto Diedrich (nicht nur) für die 1A Probenpräparation(en), Dipl.-Geowiss. Wanja Dziony, Dipl.-Geowiss. Erik Wolff, sowie PD Dr. Jürgen Koepke für die Betreuung an der Mikrosonde.

Im Folgenden halte ich mich kurz, möchte mich vor allem für große Unterstützung bedanken, die ich in all der Zeit vom Institut für Mineralogie erhalten habe.

Vor allem vielen Dank an Adrian, André und Erik für die Korrekturlesungen. Einen großen Dank an Jan Stelling (meinen Ex-Büroteiler), Sabine für den Kaffee, Christoph für die Computerbastelleien, und vielen Ehemaligen, die mich (auch auf Exkursionen) begleitet haben.

Der Deutschen Forschungsgemeinschaft (DFG) danke ich für die Finanzierung dieses Projektes (Projektnr. NO378/4-1 -4-2).

Zum Schluss gilt mein ganz besonderer Dank meiner Familie, von der ich immer bedingungslose Unterstützung erhalten habe!

Table of Contents

Chapter I: Temperature dependence of sulfide and sulfate solubility in olivine-saturated basaltic magmas at 200 MPa.....	5
1. Introduction	5
2. Experimental methods.....	6
2.1 Starting materials.....	6
2.1.1 Glass composition and preparation	6
2.1.2 Sulfur source	8
2.2 Experimental techniques	8
2.2.1 Preparation of Au capsules for 1050°C experiments	9
2.2.2 Double-capsule technique for HT/HP- experiments	9
2.2.3 Olivine containers: Preparation and loading sequence	11
2.3 Experimental runs	13
3. Analytical methods.....	14
3.1 Electron microprobe analyses (EMPA).....	14
3.1.1 Glass analysis	15
3.1.2 Analysis of OL containers.....	16
3.1.3 FeS, PdS and CaSO ₄ analyses	16
3.2 Determination of sulfur speciation in the glasses.....	17
3.3 Determination of oxygen fugacity in the experiments	18
3.4 Determination of sulfur fugacity in FeS-saturated experiments	19
3.5 Determination of H ₂ O concentration in the glasses	19
4. Results	20
4.1 Description of experimental products	20
4.2. Composition of S-bearing phases and Fe-oxides	21
4.3 Composition of OL containers	22
4.4 Major element composition of experimental glasses	23
4.5 Concentrations of dissolved H ₂ O	26
4.6 Redox conditions in the experiments	27
4.7 Concentrations of dissolved S in basaltic glasses - dependence on T and <i>f</i> O ₂	28
5. Discussion	30
5.1 Attainment of equilibrium: Fe-Mg exchange reactions between OL containers and basaltic melts	30

5.2	Sulfide and sulfate solubility in OL-saturated basaltic magmas.....	31
5.2.1	S concentration of the FeS-saturated melts as a function of T, fO_2 and fS_2	31
5.2.2	S concentration in the melt at PdS-saturation	34
5.2.3	S concentration in the melt at anhydrite-saturation	34
5.3	Sulfur speciation and redox conditions of sulfide- and sulfate- saturated melts	35
5.4	Redox and temperature control on S solubility in basaltic magmas	38
5.5	Application of the experimental data to natural magmatic systems	40
6.	Conclusions.....	43

Chapter II: Sulphur and chlorine partitioning between aqueous fluid

	and silicate melt at 1050°C	45
1.	Introduction.....	45
2.	Experimental techniques.....	46
2.1	Starting glass.....	46
2.2	Sample preparation	47
2.3	Experimental methods.....	47
3.	Analytical methods	55
3.1	Electron microprobe analysis (EMPA).....	55
3.1.1	Analysis of glasses, FeS and mineral phases	55
3.2	Determination of sulfur speciation and fO_2	55
3.3	Determination of H ₂ O concentration in the glasses.....	56
3.4	Determination of fluid composition.....	57
4.	Results	60
4.1	Description of experimental products	60
4.2	Oxidation state of experimental glasses.....	61
4.3	Sulfur fugacity at FeS-saturation	62
4.4	Major element composition of experimental glasses (melts).....	63
4.4.1	Concentration of alkalis (Na ₂ O, K ₂ O and CaO) in the melt	63
4.4.2	MgO and FeO concentration in the melt.....	65
4.5	H ₂ O, Cl and S concentrations of melt and fluid phase.....	67
4.5.1	Effect of chlorine on the H ₂ O concentration in the melt.....	68
4.5.2	Mutual effects of chlorine and sulfur on S and Cl concentration in the melt	69
4.5.3	Effect of Cl on the S concentration in the melt.....	72
4.5.4	Effect of S on the Cl concentration in the melt.....	73

4.5.5	Correlation between Cl and S concentrations in the melt	74
5.	Discussion	75
5.1	S and Cl partitioning between melt and fluid.....	75
5.2	Cation extraction from the melt into the fluid.....	78
5.3	The effect of cation extraction on S and Cl fluid/melt-partitioning.....	80
5.4	Implication to the natural magmatic system of Mt.Etna	84
6.	Conclusions	79
References	91
Appendix	105

Chapter I: Temperature dependence of sulfide and sulfate solubility in olivine-saturated basaltic magmas at 200 MPa

1. Introduction

The knowledge of S solubility depending on T, P, fO_2 and cH_2O being relevant for storage conditions of most basaltic magma chambers (e.g., 1050-1250°C, 100-500 MPa, fO_2 ~FMQ to FMQ+3, 1-6 wt.% H_2O) requires experimental simulation of natural conditions and data on equilibrium partitioning of S between fluid and melt. Numerous fundamental experimental studies were published concerning the sulfur solubility in basaltic-like melts (e.g., Haughton et al., 1974; Katsura & Nagashima, 1974; Wendtland, 1982; Luhr, 1990; Holzheid & Grove, 2002, O'Neill & Mavrogenes, 2002; Jugo et al., 2005a, Liu et al., 2007; Moune et al., 2009), but none of them cover the wide range of storage conditions relevant for most basaltic magmas. The main reasons for the scarcity of data are experimental difficulties by handling (hydrous) S-bearing systems that are highly corrosive to the noble metal containers for experimental samples, generally used at high T and P.

Thus, the available sample capsules are limited to material being less reactive to S: e.g., (1) graphite (allowing only $fO_2 < \sim FMQ -2$); (2) Au (limiting T to $\leq \sim 1050^\circ C$, because of Au melting point $\sim 1064^\circ C$, 1 atm); (3) AuPd (only allows short run-durations $\leq \sim 4$ h, not sufficient to attain equilibrium conditions); (4) olivine (OL) capsule made out of a single crystal OL (challenging to keep close in hydrous S-bearing systems). This encouraged us to develop an approach allowing conduction of hydrous S-bearing experiments by using OL-capsules, because they promise to be mostly successful in terms of material failure. Therefore, we developed a “mini-autoclave” made of an olivine piston fitting tightly into an olivine capsule which works as

a sample container (San Carlos olivine). Such a design minimizes direct contact and reaction between S-bearing phases and noble metal capsule.

The main objective of this work was investigation of the effect of temperature (ranging from 1050 to 1250°C) on S solubility at both reducing (~FMQ) and oxidizing (~FMQ+2) conditions, because of two aspects: (1) S in silicate melts occurs mainly as sulfide (S^{2-}) at reduced conditions (\leq ~FMQ) and as sulfate (S^{6+}) at oxidizing conditions (\geq ~FMQ+2) (Carroll and Rutherford, 1988; Wallace and Carmichael, 1994; Jugo et al., 2005b, *subm.*) (2) the large expected difference between sulfide and sulfate solubility (being about ~4-10 times higher for sulfate (S^{6+})) (e.g., Carroll & Rutherford, 1985, 1987; Luhr, 1990; Jugo et al., 2005a, Parat et al., 2008). Moreover, the investigated temperature range represents conditions in magmatic systems undergoing progressive cooling and differentiation. Thus, the obtained results will provide quantitative constraints on the geochemical behavior of sulfur in natural basaltic systems.

2. Experimental methods

2.1 Starting materials

2.1.1 Glass composition and preparation

The starting material was prepared from a natural rock sample from the 2001 eruption of Mt. Etna (collected at the S-side near Rifugio Sapienza, 1892 m a.s.l. and provided by Max Wilke). The sample represents primitive trachybasaltic lava erupted from the upper vents as described by Métrich et al. (2004). The same composition has been already used in former studies focused on the solubility of H₂O-Cl- and H₂O-Cl-F-bearing fluids as well as on the S speciation in basaltic magmas (Stelling et al., 2008; Chevychelov et al., 2008b; Jugo et al., *subm.*, respectively).

The natural rock sample was crushed in a steel mortar and fused in a platinum crucible for 3 h at 1600°C in an a 1-atm furnace. The obtained melt was quenched by placing the crucible in a water bath. To ensure homogeneity, the quenched melt (glass) was crushed again, ground in an agate mortar, refused for 0.5 h at the same conditions and subsequently quenched in a water bath. The glass was subsequently ground and sieved to a grain size <200 μm.

Since the experiments were planned for hydrous conditions, the starting glass was pre-saturated with H₂O. The dry glass powder was loaded together with distilled water (~10 wt.% bulk H₂O) in Au₈₀Pd₂₀ capsules and run in an internally heated pressured vessel (IHPV) at 200 MPa, 1200°C and at log *f*O₂ ~FMQ+4.2, which represents the intrinsic redox conditions imposed by the IHPV and prevailing in the water-saturated system (Berndt et al., 2002; Schuessler et al., 2008). The capsules were run for about 4 h and rapidly quenched. The synthesized and quenched glass was again crushed in an agate mortar and sieved to a grain size <200 μm. Water concentration was determined by Karl-Fischer-Titration (KFT, Behrens, 1995) to be 4.77 ± 0.03 wt.%.

Table 1: Chemical composition of the anhydrous and hydrous starting glass (in wt.%)

SiO ₂	TiO ₂	Al ₂ O ₃	FeO _{tot}	MnO	MgO	CaO	Na ₂ O	K ₂ O	P ₂ O ₅	Cl	S	Total	A/CNK	H ₂ O
anhydrous composition (n = 20):														
48.26 (33)	1.77 (07)	16.37 (23)	10.46 (43)	0.17 (07)	5.96 (18)	10.81 (34)	3.45 (15)	1.96 (09)	0.59 (02)	0.06 (00)	b.d.	99.84 (70)	0.60	n.d.
hydrous composition* (n = 15):														
45.92 (25)	1.73 (04)	15.92 (20)	10.04 (38)	0.18 (03)	5.70 (14)	10.28 (26)	3.33 (11)	1.90 (06)	0.55 (04)	0.06 (00)	b.d.	96.08 (67)	0.60	4.77 (03)
*hydrous composition normalized to 100:														
48.03 (26)	1.81 (05)	16.65 (20)	10.50 (40)	0.18 (03)	5.96 (15)	10.76 (27)	3.49 (12)	1.99 (06)	0.57 (05)	0.06 (00)	b.d.	100	0.60	-

Notes: n is the number of analyses. Number in parenthesis is 1 σ standard deviation of the mean. FeO_{tot} is the total iron content. A/CNK is the molar ratio of Al₂O₃/(CaO + Na₂O + K₂O). H₂O content was determined by Karl-Fischer-Titration (KFT).

The chemical compositions of both starting glasses, i.e., anhydrous (used for 1050°C experiments) and hydrous (used for experiments in OL containers at 1150-1250°C, see below) were determined by electron microprobe analysis (Table 1).

2.1.2 Sulfur source

Three different sources of S were used in the experiments: (1) sulfide-saturated systems were investigated using FeS or PdS as sulfide-bearing source material; (2) sulfate-saturated systems were studied using CaSO₄ as sulfate-bearing source, and (3) elemental S was added to the system in the experiments at 1050°C. The mass of initially added sulfur was in the range from 0.38 to 0.70 mg sulfur-equivalent for FeS or PdS, 0.59-0.69 mg for CaSO₄ and 0.94 to 0.97 mg elemental S, resulting in initial bulk sulfur concentrations ranging from 1.20 to 3.16 wt.% (with respect to the total mass of starting glass material, charged in the olivine container, and to the mass of added S). The experimental starting masses and mass relations are reported in Table 2.

Table 2: Starting mass relations in experimental charges

Run#	m glass [mg]	m H ₂ O _{incl} [mg]	m H ₂ O _{added} [mg]	S source	m S source [mg]	c PdO [wt.%]	c FeO [wt.%]	c CaO [wt.%]	m S [mg]	bulk S [wt.%]	bulk H ₂ O [wt.%]	fluid XS molar	fluid XH ₂ O molar
0_15_2 ox	43.65	-	5.19	S	0.94	-	-	-	0.94	1.89	10.43	0.09	0.91
0_15_2 red	46.71	-	6.11	S	0.97	-	-	-	0.97	1.80	11.36	0.08	0.92
S2	29.54	1.41	-	PdS	1.87	4.04	-	-	0.43	1.38	4.49	0.15	0.85
S8	30.65	1.46	-	FeS	1.04	-	1.70	-	0.38	1.20	4.61	0.13	0.87
S18	27.16	1.30	-	FeS	1.13	-	2.07	-	0.41	1.46	4.58	0.15	0.85
S19	31.14	1.49	-	FeS	1.56	-	2.48	-	0.57	1.74	4.54	0.18	0.82
S20	30.13	1.44	-	FeS	1.69	-	2.76	-	0.62	1.94	4.52	0.19	0.81
S21	30.45	1.45	-	FeS	1.75	-	2.82	-	0.64	1.98	4.51	0.20	0.80
S23	31.69	1.51	-	CaSO ₄	2.89	-	-	3.44	0.68	1.97	4.37	0.20	0.80
S24	31.18	1.56	-	CaSO ₄	2.95	-	-	3.56	0.69	2.04	4.36	0.21	0.79
S26	16.17	0.81	-	CaSO ₄	2.51	-	-	5.53	0.59	3.16	4.13	0.30	0.70

Notes: m is the weighed mass. c is the concentration in wt%. Bulk S is the concentration of S, taking the total loaded mass of starting material into account. H₂O_{incl} is the mass of H₂O included in the water presaturated starting glass. H₂O_{added} is the mass of added H₂O by using dry starting glass. S source is the sulphur source material used for the experiments. XS and XH₂O are the molar ratios of bulk S/(bulk S + bulk H₂O) or bulk H₂O/(bulk H₂O + bulk S), respectively.

2.2 Experimental techniques

Owing to a very aggressive nature of S and S-bearing phases (fluids or melts) which easily react with the noble metal capsules, two different experimental approaches have been used in this study. At temperature of 1050°C, the experiments have been conducted in Au capsules that can withstand reaction with S even at relatively high amounts of charged sulfur. At

temperatures above the melting point of gold (i.e., more than $\sim 1060^\circ\text{C}$ at 200 MPa), a new technique has been developed and applied. The basaltic glass powder and S starting material were loaded in olivine (OL) containers sealed in outer $\text{Au}_{80}\text{Pd}_{20}$ capsules as described in detail below.

2.2.1 Preparation of Au capsules for 1050°C experiments

At 1050°C , one sulfide-saturated and one CaSO_4 -saturated experiment were performed. About 45 mg of anhydrous basaltic powder were charged together with ~ 0.95 mg elemental S and ~ 5 -6 mg deionised H_2O into Au-capsules (length of 15 mm, inner/outer diameter 2.8/3.2 mm). The total initial amount of added volatiles was ~ 12 and 13 wt.% and the load amount of S was 1.8 and 1.89 wt.% S, respectively with respect to the total charge mass (Table 2). The capsules were weighed before and after welding and stored for > 6 h at $\sim 110^\circ\text{C}$ and 1 atm in a drying furnace allowing check for possible leaks by subsequent weighting.

2.2.2 Double-capsule technique for HT/HP- experiments

A few experimental studies were published using OL containers to minimize reaction of experimental charge with capsule material, e.g., Ehlers et al. (1992) and Gaetani & Grove (1999), both at 1atm; Holzheid & Grove, 2002 (at 0.9-2.7 GPa) and Brey et al., 2008 (at 6-10 GPa), both in piston cylinder apparatus. The experiments of Gaetani & Grove (1999) and Holzheid & Grove (2002) were S-bearing and anhydrous. To the best of our knowledge OL containers have not been successfully applied to volatile-rich (H_2O and S) systems at high temperatures and moderate pressures of 200 MPa so far.

For a successful application of OL containers in volatile-rich systems following requirements must be maintained: (1) OL container should sustain high pressure and temperature without cracking; (2) OL container should be relatively well sealed to avoid/minimize loss of volatiles from the system; (3) temperature and pressure inside the OL container must be the same

as the outside conditions applied in the experiment; (4) the possible reaction between OL container and investigated silicate melt should not produce any exotic phases or dramatic unexpected changes in melt composition.

To satisfy all those requirements, we have developed a “mini-autoclave”, composed of an olivine piston fitting tightly into the olivine container as illustrated in Fig.1. Olivine powder was placed outside the OL container to serve as a medium transducing pressure from $\text{Au}_{80}\text{Pd}_{20}$ capsule wall of the capsule to the OL piston.

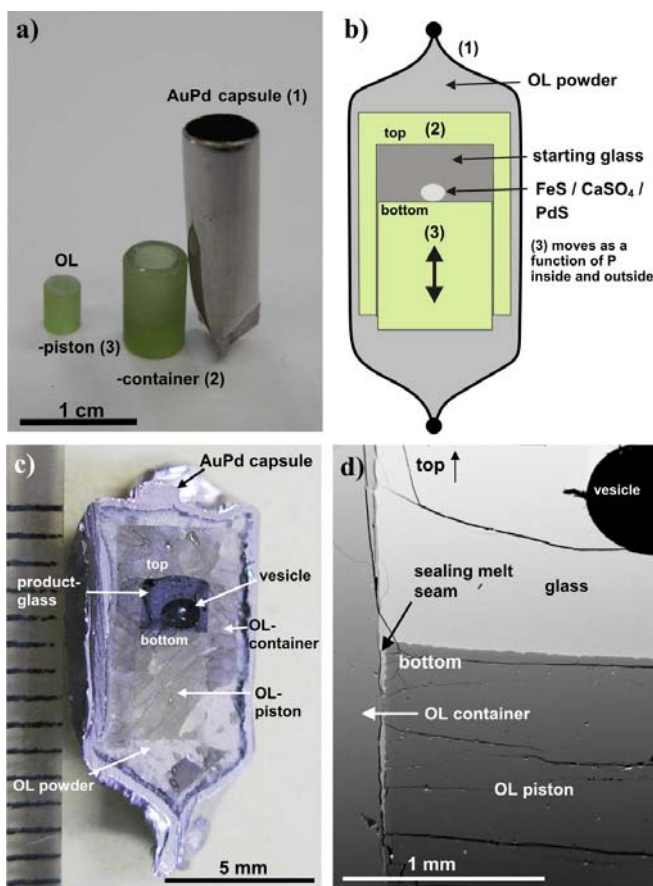


Fig.1: Photograph of the AuPd capsule (1) (a), the OL container (2) and the OL piston (3); sketch of the double-capsule setup and illustration of the piston moving as a function of P inside and outside the container (b); photograph of a longitudinal cut capsule, after the experimental run (c); BSE-picture of the sealing melt-seam located between OL piston and the wall of the OL container (d); “top” and “bottom” describe the orientation of the double-capsule during the experimental run (b-d).

Such a design allows compensation of volume change inside the olivine container due to movement of the piston depending on the difference in pressure inside the container and superimposed pressure at pressurization and heating stage of the experiment. On the other hand, it minimizes the migration of fluids, in particular S, from the inner part of the container, and hence, the reaction of S with outer $\text{Au}_{80}\text{Pd}_{20}$ capsule. The cracking of the OL container is not a serious problem until no fluid escape occurs through such cracks, which was not observed in our experiments. Desired temperature can be easily achieved inside the containers due to small size

of the capsules, sufficiently high thermal conductivity of olivine, and long run duration. Because we investigated basaltic composition in our study, the use of olivine containers provided conditions corresponding to olivine-saturated basaltic magmas which are typical for many basaltic volcanoes. Hence, the formation of exotic phases is not expected, whereas possible changes in melt and olivine compositions with changes in temperature should represent compositional evolution of olivine-saturated basalts. Thus, the simulated systems can be used as a direct manifestation of natural basaltic magmas. Moreover, the olivine-melt assemblage ideally represents the melt inclusions trapped in olivine phenocrysts that are usually used to investigate magma storage conditions.

2.2.3 Olivine containers: Preparation and loading sequence

The olivine containers and pistons were drilled out from natural Mg-rich single-crystal olivine (San Carlos olivine with a forsterite number (Fo#) of 90-96 (where Fo# is the molar proportion of Mg / (Fe + Mg), in %). The typical size of the containers was 4.8 mm (outer diameter), 3 mm (inner diameter), 8 mm length and 5.5 mm inner borehole length. The OL pistons were 4 mm long with a diameter of 2.9 mm. The OL containers were firstly filled with the S source (PdS, FeS or CaSO₄) and subsequently with 20-45 mg H₂O-saturated basaltic glass powder. After charging, they were closed with the OL piston and inserted into outer Au₈₀Pd₂₀ capsules (15-20 mm in length with an outer/inner diameter of 5.4/5.0 mm). Finally, the OL containers were covered by OL powder. The loading sequence and preparation procedure are illustrated in Fig. 1.

Since OL containers were not completely sealed by closing the OL piston, S could potentially escape from OL containers and react with the outer noble metal capsule leading to experimental failure. Hence several charging procedures were tested to optimize separation of S from the outer Au₈₀Pd₂₀ capsule. In the first test, additional basaltic glass powder was placed outside at the seam between piston and OL capsule, to produce a sealing “silicate melt plug”

during heating to the experimental temperature. It turned out however, that at the experimental conditions small amounts of melt from the inner part of the OL container moved along the seam between piston and the wall of OL container providing a self-sealing material which increases the distance for possible S diffusion from the inner space of the container to the outside part of the double capsule assemblage, and hence, preventing reaction with $\text{Au}_{80}\text{Pd}_{20}$ capsule and keeping S activity in the system almost constant (Fig. 1d). Our successful runs show that the system silicate melt-S-source-fluid within OL containers reaches local equilibrium and remains quasi-closed (at least no S loss from the $\text{Au}_{80}\text{Pd}_{20}$ capsules was observed) after up to 46 hours of the experiments. Thus, these test experiments have demonstrated that an additional plug composed of glass powder is not required.

Another test was conducted in attempt to separate the sample powder from the S source material (e.g., FeS) in order to: (1) increase the migration distance for S to escape from the container; (2) minimize possible contamination of the melt with Fe or Ca from the S sources. To do this, an olivine disc was placed in between the FeS and glass powder. Although the run durations in these experiments were relatively long (e.g., 46 h at 1200°C), the experimental glasses, separated from FeS by OL disk, showed inhomogeneous distribution of S concentrations decreasing from the separating disk to OL piston (e.g., from ~ 1200 to 300 ppm S along a distance of ~ 1.5 mm). On the contrary, in the experiments with direct contact between silicate melt and FeS, S concentrations were systematically higher and showed quite homogeneous distribution along the sample (e.g., $\sim 3000 \pm 300$ ppm S at 1150 and 1200°C). Thus, the separation of the melt and S source by OL disk was not successful indicating that another approach should be developed, if necessary.

Finally, it must be noted that the OL piston should be closed from the bottom of the OL container, oriented vertically as shown in Fig.1b-d. This will limit the ability of S-bearing fluids to escape by buoyancy difference between fluid and silicate melt during the run.

Mostly homogeneous, inclusion- and impurity-poor natural OL crystals were used for container and piston material. This is of major importance with respect to resistance against directional stresses, in particular occurring at experimental pressurization, heating and quenching. The outer Au₈₀Pd₂₀ capsules were welded shut by graphite arc welding, keeping the capsules cooled in a water bath. The welded double capsules were checked for leaks before and after the experiments by cooling in a refrigerator and subsequently throwing them into boiling water. Thus, it was possible to localize very tiny leaks, even if they are invisible under the binocular, by the formation of gas bubbles from the expanding gas inside.

2.3 Experimental runs

A suitable apparatus simulating most geologic relevant conditions of the upper crust (e.g., for magma storage and conditions at magma ascent) is an internally heated gas pressure vessel (e.g., Holloway, 1971; Holloway et al., 1992; Roux & Lefèvre, 1992; Berndt et al., 2002). The experiments were conducted in two different types of vertically mounted IHPV: one IHPV was pressurized with pure Ar gas as a pressure medium, where the intrinsic redox conditions correspond to $\log fO_2 \sim FMQ+4.2$ at water saturated conditions (Berndt et al., 2002; Schuessler et al., 2008). The other vessel allows addition of desired amounts of H₂ to the Ar gas. The partial pressure of H₂ in the vessel can be monitored by a Shaw-membrane during the run (Table 3). All experiments were conducted at pressure of 200 MPa. Pressure was controlled by a calibrated digital pressure transducer (Burster Type 8221) with an uncertainty of 1 MPa. Temperatures of the experiments were varied as 1050, 1150, 1200 and 1250°C and controlled over a length of ~30 mm using four S-type (Pt-Pt₉₀Rh₁₀) thermocouples (a detailed description of the sample holder and the vessel is given by Berndt et al., 2002). Observed temperature fluctuations were less than 5°C in all experimental runs. However, the estimated error in temperature is within +/- 10°C. Run durations were 6-46 h for OL-container runs (1150 to 1250°C) and 72 h for runs in

Au capsules at 1050°C (Table 3). All experiments were stopped by rapid quench technique with a cooling rate of ~150°C/s (Berndt et al., 2002).

3. Analytical methods

After experimental runs, the capsules were mounted in epoxy and a slice was cut longitudinally through the centre (thickness ~1 mm). This slice, representing a vertical section of the double capsule setup (as shown in Fig. 1c), was fixed on an object plate and polished to a thin section used for optical microscopy and electron microprobe analysis. The thin sections for microprobe analysis of the product glasses, obtained in the Au-capsule runs, were prepared by taking three pieces of each sample to ensure representativeness.

The experimental products were composed of silicate glasses, FeS, PdS or PdFeS, CaSO₄ and fluid phase. The presence of fluid was indicated by at least one of the following criteria: (1) weight loss after opening the capsule, (2) the smell of H₂S by opening the capsules after runs at reduced conditions, (3) vesicles observed in the glass of OL-container runs or (4) “wet” fluid being still present inside the Au capsules. The exact composition of the fluid was not determined due to small or sometimes negligible amount of the fluid after experiments and due to the fact that the fluid phase was unquenchable. The compositions of glasses, OL containers/pistons, FeS and CaSO₄ were determined using electron microprobe, KFT and FTIR methods.

3.1 Electron microprobe analyses (EMPA)

All electron microprobe analyses were conducted using Cameca SX 100 electron microprobe at the Institute for Mineralogy, Leibniz University of Hannover. For all analyses the acceleration voltage of the electron beam was set to 15 kV.

3.1.1 Glass analysis

Experimental glasses were analysed using a 20 μm defocused beam. For analysis of main elements, the beam current was adjusted to 4 nA and counting times of peak and background were 8 s for Si, Ti, Al, Mg, Ca, Fe and Mn and 4 s for Na and K in order to minimize migration of alkalis. A systematic analytical study demonstrated that no alkali loss occurs at these analytical conditions for the same glass composition (Stelling et al., 2008). Sulfur, Cl and P_2O_5 were analysed at 40 nA beam current and with counting times for peak and background of 60 s for S, Cl and P resulting in a detection limit of about 60, 80 and 300 ppm, respectively. Sulfur concentrations were measured using $\text{SK}\alpha$ peak position determined by the method described below in §3.2. The chemical composition of the product glasses is listed in Table 3.

Table 3: Experimental conditions, listing of run products and chemical composition of product glasses (in wt.%)

Run#	Sulfide-saturated runs							Sulfate-saturated runs				
	0_15_2 red	S2	S8	S18	S19	S20	S21	0_15_2 ox	S23	S24	S26	
n	14	30	20	15	16	15	15	14	15	17	40	
Capsule type:	Au	OL	OL	OL	OL	OL	OL	Au	OL	OL	OL	
T [°C]	1050	1200	1200	1200	1150	1150	1250	1050	1200	1250	1150	
PH_2 [bar]	8.9	i.c.	i.c.	i.c.	i.c.	i.c.	i.c.	i.c.	i.c.	i.c.	i.c.	
$\text{S}^{6+}/\Sigma\text{S}^*$	0.16	0.66	0.16	0.08	0.16	0.11	0.08	0.95	0.82	0.82	0.71	
$\log f_{\text{O}_2}$ [bar]*	-9.7	-6.8	-7.8	-8.2	-8.4	-8.6	-7.6	-7.8	-6.5	-5.9	-7.3	
Δ FMQ*	0.3	1.3	0.3	0.0	0.3	0.1	0.0	2.2	1.7	1.7	1.4	
P [MPa]	193	200	200	200	200	200	200	200	200	200	200	
run-time [h]	54	22	24	24	56	56	38	54	24	18	35	
SiO_2	46.68 (38)	46.98 (51)	45.93 (26)	45.79 (26)	46.03 (43)	46.2 (03)	45.38 (33)	48.16 (38)	43.51 (44)	43.74 (44)	45.57 (04)	
TiO_2	1.67 (05)	1.63 (05)	1.58 (07)	1.53 (04)	1.61 (05)	1.64 (06)	1.41 (06)	1.63 (04)	1.41 (06)	1.32 (05)	1.62 (07)	
Al_2O_3	16.05 (26)	14.96 (24)	14.53 (22)	14.47 (02)	15.05 (26)	15.26 (18)	13.19 (21)	16.23 (21)	12.82 (15)	12.16 (28)	15.08 (18)	
FeO_{tot}	7.72 (42)	9.02 (52)	10.01 (35)	9.77 (43)	10.38 (28)	10.19 (36)	10.71 (46)	6.83 (42)	9.28 (36)	9.42 (34)	9.14 (34)	
MnO	0.17 (02)	0.17 (02)	0.30 (04)	0.14 (08)	0.13 (07)	0.24 (08)	0.21 (08)	0.16 (02)	0.16 (11)	0.16 (08)	0.17 (09)	
MgO	5.56 (15)	9.85 (24)	9.61 (19)	10.49 (17)	8.47 (02)	8.24 (16)	13.47 (26)	5.45 (17)	12.03 (02)	13.61 (27)	7.62 (24)	
CaO	10.31 (27)	9.67 (24)	9.34 (02)	9.32 (34)	9.81 (03)	9.87 (35)	8.41 (25)	8.96 (02)	11.1 (24)	10.74 (21)	14.41 (28)	
Na_2O	3.50 (18)	3.07 (22)	3.04 (16)	2.94 (21)	3.09 (23)	3.07 (19)	2.58 (23)	3.15 (17)	2.36 (21)	2.39 (18)	2.59 (18)	
K_2O	1.84 (07)	1.77 (09)	1.72 (08)	1.62 (13)	1.80 (09)	1.80 (09)	1.48 (01)	1.72 (12)	1.32 (05)	1.36 (07)	1.5 (07)	
P_2O_5	0.51 (03)	0.55 (02)	0.49 (02)	0.48 (02)	0.49 (03)	0.52 (02)	0.46 (02)	0.48 (06)	0.43 (02)	0.43 (02)	0.48 (03)	
Cl	0.06 (00)	n.d.	n.d.	0.06 (00)	0.06 (00)	0.07 (00)	0.05 (00)	0.04 (00)	0.04 (00)	0.04 (01)	0.06 (01)	
S	0.12 (01)	0.22 (00)	0.30 (04)	0.30 (03)	0.31 (06)	0.27 (07)	0.39 (02)	0.74 (01)	1.04 (03)	1.08 (04)	0.75 (04)	
Total	94.17 (78)	97.9 (111)	96.71 (69)	96.91 (62)	97.23 (72)	97.38 (72)	97.74 (101)	93.54 (08)	95.49 (78)	96.45 (68)	99.00 (68)	
A/CNK	0.61	0.61	0.61	0.61	0.61	0.61	0.62	0.7	0.5	0.49	0.47	
MFM	6.16	7.98	8.57	9.07	8.03	7.88	11.13	4.94	10.43	11.65	8.19	
Mg#	61.9	72.3	67.5	69.4	64.0	63.5	72.4	69.2	76.5	78.3	67.9	
$\text{Fe}^{3+}/\Sigma\text{Fe}$						0.22 (03)	0.23 (03)		0.31 (03)	0.29 (03)		
$\text{H}_2\text{O KFT}$ [wt.%]	4.84 (10)							5.48 (08)				
$\text{H}_2\text{O b.d.}$ [wt.%]	6.0 (7)	2.8 (1)	3.4 (6)	3.5 (5)	3.2 (6)	3.1 (6)	2.8 (9)	6.6 (7)	4.8 (7)	3.9 (6)	1.4 (7)	
$\text{H}_2\text{O IR}$ [wt.%]	5.85 (18)	1.71 (16)	1.71 (15)	n.d.	n.d.	n.d.	n.d.	n.d.	2.72 (25)	2.62 (24)	0.88 (08)	
Phases	gl. FeS	gl. PdS, PdFeS	gl. FeS	gl. FeS	gl. FeS	gl. FeS	gl. FeS	gl. FeS	gl. anh, spl	gl. anh	gl. anh	gl. anh

Notes: PH_2 is the measured hydrogen pressure in the vessel by the shaw membrane-technique; i.c. means intrinsic redox-conditions prevailing in the vessel without adding H_2 to the Ar gas (FMQ+4.2 at water saturation). The $\text{S}^{6+}/\Sigma\text{S}$ ratio was determined by S K α peak shift (Carroll & Rutherford, 1988), detailed description in the text. $\log f_{\text{O}_2}$ [bar] derived from $\text{S}^{6+}/\Sigma\text{S}$ ratios using the method of Wallace & Carmichael (1994) (detailed description is given in the text). Δ FMQ is $\log f_{\text{O}_2}$ [bar] relative to that of the FMQ-buffer reaction. MFM is the compositional parameter (Liu et al., 2007) describing the melt based upon cation mole fractions: $\text{MFM} = \text{Na} + \text{K} + 2(\text{Ca} + \text{Mg} + \text{Fe}^{2+}) / [\text{Si} \times (\text{Al} + \text{Fe}^{3+})]$. Mg# is the Mg-number: molar $\text{Mg}/(\text{Mg} + \text{Fe}^{2+})$ ratio $\times 100$. For MFM and Mg#, Fe^{2+} and Fe^{3+} were calculated by Kress & Carmichael (1991) with f_{O_2} derived from $\text{S}^{6+}/\Sigma\text{S}$ ratio. $\text{Fe}^{3+}/\Sigma\text{Fe}$ is the ratio of Fe^{3+} to total Fe, determined by Mössbauer spectroscopy. * Error of $\text{S}^{6+}/\Sigma\text{S}$ ratio is about 0.13 resulting in an error of f_{O_2} on ~ 0.8 log units for the reduced glasses (\sim FMQ) and ~ 0.4 for the oxidizing glasses (\sim FMQ+1.5) (detailed description in the text).

3.1.2 Analysis of OL containers

All OL containers were analysed in order to determine compositional changes due to potential chemical reactions with either silicate melt, or S-source, or S-bearing fluid. To do this, analytical traverses with a 5 μm step and with a total length of 50 μm were measured across to the interface between OL container/piston and silicate glasses. The analyses of OL were performed using a focused beam, 15 nA beam current for measurement of Si, Ti, Al, Mg, Ca, Fe, Mn, Na and K and 40 nA for analysing S (if any), respectively. Counting times of peak and background were 4 s for Na and K, 10 s for S and 8 s for all other elements.

3.1.3 FeS, PdS and CaSO₄ analysis

Analyses of sulfides were conducted using three different settings. FeS phases were analysed either, for (1) Fe and S only and in some cases for (2) Fe, S and in addition for Na, Si, Al, Ca, K, Ti, Mg and Mn to provide accuracy of analyses, in particular for phases smaller than 10 μm . The third setting was applied for measurements of PdFeS phases focussing on the determination of (3) Fe, S and Pd. For all three settings, the beam was focused and adjusted to 15 nA for analysing Fe, Pd, Si, Ti, Al, Mg, Ca, Fe, Mn, Na and K and 40 nA for analysing S, respectively. The counting times on peak and background were 10 s for S and Pd, 4 s for Na and K and 8 s for all other elements. Only one anhydrite crystal was analysed quantitatively using the same beam setup as for OL analyses. All other sulfates have been qualitatively identified by EDX analysis.

Table 4: Chemical composition of sulfide products (in wt.%)

Run#	0_15_2 red	S2	S2	S8	S8	S18	S19	S20	S21
n	4	9	12	5	4	6	4	8	
S source	S	PdS	PdS	FeS	FeS	FeS	FeS	FeS	FeS
product	FeS	PdS	PdFeS	FeS one small*	FeS one big*	FeS	FeS	FeS	FeS
comment*		dark*	light*						n.d.
wt.% at.									
Si	n.d.	n.d.	n.d.	n.d.	n.d.	0.04 (02)	0.02 (00)	0.08 (11)	
Ti	n.d.	n.d.	n.d.	n.d.	n.d.	0.03 (01)	0.01 (00)	0.04 (02)	
Al	n.d.	n.d.	n.d.	n.d.	n.d.	0.01 (01)	0.00 (01)	0.02 (04)	
Fe _{tot}	60.08 (76)	0.62 (68)	4.56 (154)	54.71 (145)	59.25 (157)	60.05 (93)	60.04 (18)	60.33 (76)	
Mn	n.d.	n.d.	n.d.	n.d.	n.d.	0.12 (3)	0.15 (02)	0.10 (06)	
Mg	n.d.	n.d.	n.d.	n.d.	n.d.	b.d.	b.d.	0.03 (04)	
Ca	n.d.	n.d.	n.d.	n.d.	n.d.	0.07 (07)	0.02 (01)	0.08 (07)	
Na	n.d.	n.d.	n.d.	n.d.	n.d.	0.08 (07)	0.05 (04)	0.04 (06)	
K	n.d.	n.d.	n.d.	n.d.	n.d.	0.06 (04)	0.06 (02)	0.06 (05)	
Pd	n.d.	76.82 (99)	84.00 (203)	0.05 (04)	0.29 (40)				
S	37.17 (87)	23.77 (22)	12.18 (333)	32.21 (126)	35.61 (111)	34.85 (57)	35.60 (26)	34.34 (86)	
Total	97.25 (127)	101.21 (48)	100.74 (91)	86.97 (261)	95.15 (128)	95.32 (127)	95.96 (21)	95.12 (113)	
Fe#	48.1 (60)			49.4 (56)	48.9 (116)	49.7 (35)	49.2 (24)	50.2 (53)	
log fS ₂ (B, L)	-0.08	1.80		0.62		0.29	0.28	0.09	0.51

Notes: Fe_{tot} total Fe as Fe²⁺. Fe# is the molar ratio of Fe_{tot}/(Fe_{tot} + S) x 100, assuming all iron is present as Fe²⁺; * comment describes the product sulfide phase, where: “dark” and “light” means the gray-scale intensity in BSE-picture at one sulfide-bleb (intergrown phase, described in the text); “one small” and “one big” means analysis of one FeS each sized < ~ 20 μm and ~ 600 μm, respectively; log fS₂ (B; L) is log fS₂ [bar], calculated by Bockrath et al. (2004) and Liu et al. (2007).

3.2 Determination of sulfur speciation in the glasses

In order to determine sulfur speciation in silicate glasses, we followed the “classical” approach of Carroll & Rutherford (1988) who proposed to use wavelength dispersive spectrometry (WDS) of the electron microprobe to analyse proportions of S species in silicate melts:

$$\frac{S^{6+}}{\Sigma S} = \frac{\Delta \lambda(S K\alpha)_{glass}}{\Delta \lambda(S K\alpha)_{CaSO_4}} \quad (1)$$

where $\Delta \lambda(S K\alpha)_{glass}$ and $\Delta \lambda(S K\alpha)_{CaSO_4}$ are shifts in peak position of S K α in the sample and in the sulfate standard (CaSO₄, anhydrite), respectively, relative to the peak position of S K α in sulfide standard (FeS, pyrrhotite).

To determine S K α peak shift, we measured λ with a LPET-crystal (where 2 d = 8.75 Å) over a sin θ range of 0.61308 to 0.61507 every 0.00001 sin θ (200 steps) with a dwell time of 1000 ms. The S peak position $\lambda(S K\alpha)$ of the standards CaSO₄ and FeS were measured three times each before the analysis of each sample using an automatic peak search routine of the

Cameca software (beam conditions: 15 kV acceleration voltage, 15 μ A beam current and 2 μ m defocused beam). The peak search on the glass samples was conducted with an acceleration voltage of 15 kV, 40 μ A beam current and 20 μ m defocused beam. The electron beam was continuously moved over the sample to minimize the beam damage and artificial reduction of the S which may occur, in particular, at high-intensity beam energies (Wilke et al., 2008). At least three measurements were done for each sample to prove reproducibility of the method.

Peak positions were determined by fitting a four parameter Gaussian function, where the determined errors for each fit were about 0.02-0.03 $\lambda \text{ \AA} \times 10^{-3}$. For each sample, λ (S K α) was in the range from 0.18 to 0.44 $\text{\AA} \times 10^{-3}$. Thus, taking the whole range of S-peak position between CaSO₄ and FeS standard, averaged to $3.32 \pm 0.18 \text{ \AA} \times 10^{-3}$, into account, total errors in S⁶⁺/ Σ S ratios are about 0.13, which is approximately 2 times higher than those determined by Carroll & Rutherford (1988) and Wallace & Carmichael (1994). This difference might be due to the different measurement strategies (continuous movement of the sample vs. scanning and measuring stepwise; difference in the beam current density).

For the quantitative analysis of S concentrations in silicate glasses, we used the determined peak positions of S K α for each individual sample.

3.3 Determination of oxygen fugacity in the experiments

The analytical approach on S speciation in glasses can be used to calculate the oxygen fugacity prevailing in the system using the empirical model of Wallace & Carmichael (1994):

$$\log \left(\frac{X_S^{6+}}{X_S^{2-}} \right) = a \log fO_2 + \frac{b}{T} + c \quad (2),$$

where $X_S^{6+} = S^{6+}/\Sigma S$; $X_S^{2-} = 1 - S^{6+}/\Sigma S$; T is temperature in K; a, b, and c are regression coefficients (a = 1.02, b = 25410 K, and c = -10.0). According to the uncertainty in determination

of S speciation, the error of calculated $f\text{O}_2$ is about 0.8 log units for reduced glasses ($\sim\text{FMQ}$) and about 0.4 log units for the oxidizing ones ($\sim\text{FMQ}+1.5$).

3.4 Determination of sulfur fugacity in FeS-saturated experiments

The $f\text{S}_2$ for the FeS-saturated experiments was calculated by the method of Bockrath et al. (2004) modified by Liu et al. (2007) with extension to a thermodynamic pressure correction. It must be noted that this model is valid at $f\text{O}_2$ in the range from FMQ-1.5 to FMQ-2.5, because the $f\text{O}_2$ was calibrated in the system buffered by graphite and CO-CO₂ gas mixture. Hence, the applicability to the redox conditions of this study is not validated. Determination of $f\text{S}_2$ from the composition of FeS as proposed by Toulmin & Barton (1964) was difficult, because of large compositional variations in the quenched FeS phases (Table 4). However, in experiment at 1050°C (exp.0_15_2 red, no FeS was added as a S-source) we obtained small FeS globules yielding $N_{\text{FeS}} = 0.96 \pm 0.01$ (N_{FeS} is the molar fraction of FeS in pyrrhotite FeS-FeS₂) resulting in $\log f\text{S}_2$ [bar] $\sim -1.0 \pm 0.9$ (Toulmin & Barton, 1964). This value is comparable within the uncertainty with $\log f\text{S}_2$ [bar] value of $\sim -0.1 \pm 0.5$ determined using the model of Bockrath et al. (2004) corrected by Liu et al. (2007).

3.5 Determination of H₂O concentration in the glasses

The concentration of dissolved H₂O in all run product glasses was determined by application of the “by-difference” method (e.g., Devine et al., 1995). During each analytical EMPA session, the total analytical sum of every analysis was calibrated against analyses of a series of basaltic glasses with known water contents (Berndt et al., 2002). The errors of this approach are relatively large and are about 0.5 wt% H₂O. The glasses synthesized in Au capsules were also measured by Karl-Fischer-Titration (KFT), which is a coulometric quantitative method

to analyse the total mass of H₂O contained in the glass (Behrens, 1995). It must be noted that the H₂O concentrations of glasses, containing anhydrous phases (e.g., anhydrite, spinel) might be slightly underestimated. The methodological uncertainties of KFT analyses are estimated to be about 1-2 % relative (0.06 to 0.02 wt.% absolute) for the analysed samples (Table 3).

The H₂O concentrations in most of the samples were also measured by IR spectroscopy, using an IR microscope Bruker A594 connected to an FTIR spectrometer Bruker IFS88. Double-polished glass sections (200 µm thickness) were analysed in the Near-Infrared region and the absorption bands at ~4500 cm⁻¹ and at ~5200 cm⁻¹ were used to determine the concentrations of OH-groups and molecular H₂O, respectively. For the calculation of water species concentrations we used an approach described in detail by Ohlhorst et al. (2001). For samples S18, S19 and S20, it was not possible to record reliable spectra because the sample glass of run S18 was mingled with fine grained FeS and IR-transmittance of glasses obtained at runs S19 and S20 were too low.

4. Results

4.1 Description of experimental products

All experimental products consist of hydrous, S-rich glasses varying significantly in composition regarding MgO, FeO, CaO and K₂O concentrations. Depending on S-source material, melts in OL-container runs coexisted with: (1) FeS or PdS/PdFeS phases (if FeS or PdS added), presumably liquids at experimental conditions owing to their rounded shapes and (2) anhydrite (if CaSO₄ added) as illustrated in Fig. 2a,b. In the Au-capsule runs (elemental S added), FeS phase was present at reduced conditions (~FMQ+0.3), while anhydrite and ~ 3 vol.% spinel crystallized at oxidized conditions (~FMQ+2.2) as shown in Fig. 2c,d. In the OL-

container runs, anhydrite was observed as spinifex textured phase. The coexistence of FeS- or PdFeS globules with melts and fluid bubbles in the experimental products indicate that S was partitioned between fluid, silicate melt and FeS/PdFeS liquid (hereafter PdFeS is described as PdS).

A presence of the free fluid in the systems was ensured by weight loss after piercing of the capsule and by the strong smell of H₂S in some reduced runs. In addition, weight loss of opened capsules after drying for > 1h at 110°C confirms that fluid was present in part as a liquid in the quenched capsules.

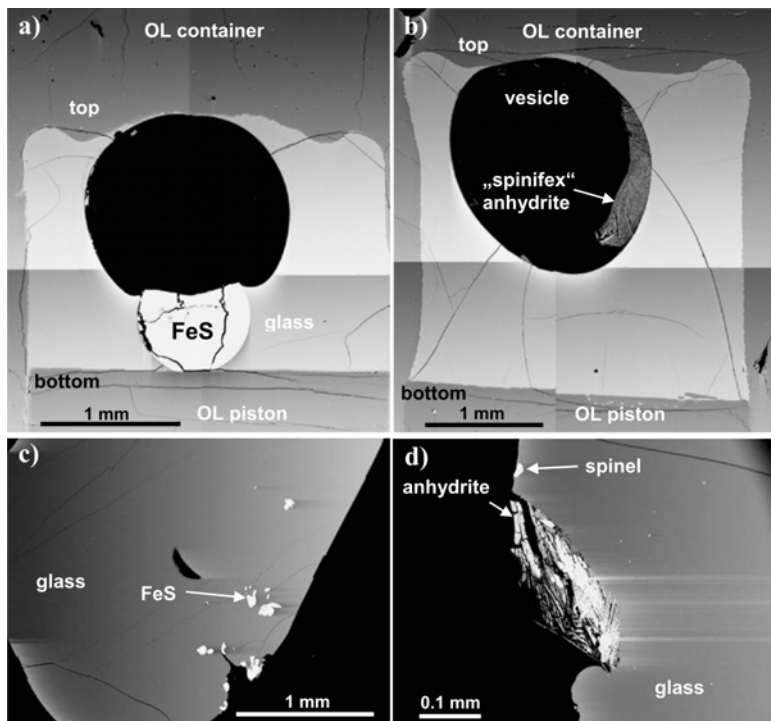


Fig.2: BSE-pictures of two OL capsule runs (a,b): exp. S 20, 1150°C, ~FMQ+0.1, FeS added (a) and exp. S23, 1200, FMQ+1.7, CaSO₄ added (b). Each experiment show similar condensed S-bearing phase than added as S-source: FeS (a), anhydrite (b). BSE-pictures of two Au-capsule runs (c,d): exp. 0_15_2 red, 1050°C, ~FMQ+0.3 (c); exp. 0_15_2 ox, 1050°C, ~FMQ+2.2 (d). In both experiments elemental sulfur was added as S-source. The condensed S-bearing phases were FeS at ~FMQ+0.3 (c) and anhydrite at ~QFM+2.2, with coexisting spinel (d).

4.2 Composition of S-bearing phases and Fe-oxides

The chemical composition of all analysed S-bearing phases is listed in Table 4. All obtained FeS phases are solely composed of Fe and S (with respect to main elements). The lowest molar Fe/S-proportion, expressed as Fe# (where $Fe\# = 100 * Fe / [Fe + S]$), is 48.1 ± 0.6

as observed in experiment at 1050°C, whereas FeS phases at higher temperatures in OL-containers have slightly higher Fe# in the range from 49 to 50 (± 1). However, taking total average sum of FeS ~ 95 -97 into account and considering that we used natural rock sample in the experiments, FeS phases may contain other siderophile elements (e.g., Ni, Pd, Pt) that were not analysed. Furthermore, Energy Dispersive X-ray analysis (EDX) indicates that FeS phases contain noticeable amounts of oxygen but these amounts can not be quantified by EDX. Intergrowths of PdS and PdFeS phases observed in the experiment S2, where PdS was added as S-source presumably indicate that sulfide phases are affected by phase unmixing during quench (e.g., observed by Holzheid & Grove, 2002; Ballhaus et al., 2006; Brenan, 2008). The molar Pd/S-ratio ($\text{Pd\#} = 100 * \text{Pd} / [\text{Pd} + \text{S}]$) is determined to be $\text{Pd\#} = 48.3 \pm 0.4$ and the PdFeS phase contains about 62 ± 2 wt.% Pd, 7 ± 1 % wt.% Fe and 31 ± 1 wt.% S.

Sulfate-bearing phases were determined qualitatively by EDX analyses, because of analytical uncertainties in measurements of μm -size spinifex structures of CaSO_4 . Peak positions of recorded EDX-spectra indicate that these phases are composed solely of Ca, S and O and hence are suggested to be anhydrite.

Only a single crystal of Fe-oxide (spinel) was found together with anhydrite phase in experimental products produced at 1050°C and oxidizing conditions. The spinel is composed of 6 wt.% Al_2O_3 , 3 wt.% TiO_2 , 8 wt.% MgO and 75 wt.% FeO (FeO as total iron).

4.3 Composition of OL containers

The diffusive concentration gradients of Mg and Fe (expressed as forsterite content, i.e., $\text{Fo\#} = 100 \times \text{Mg} / (\text{Mg} + \text{Fe})$ [molar]) are observed in the walls of the OL containers up to distances of 20 ± 5 μm from the OL-melt interface (Fig. 3a).

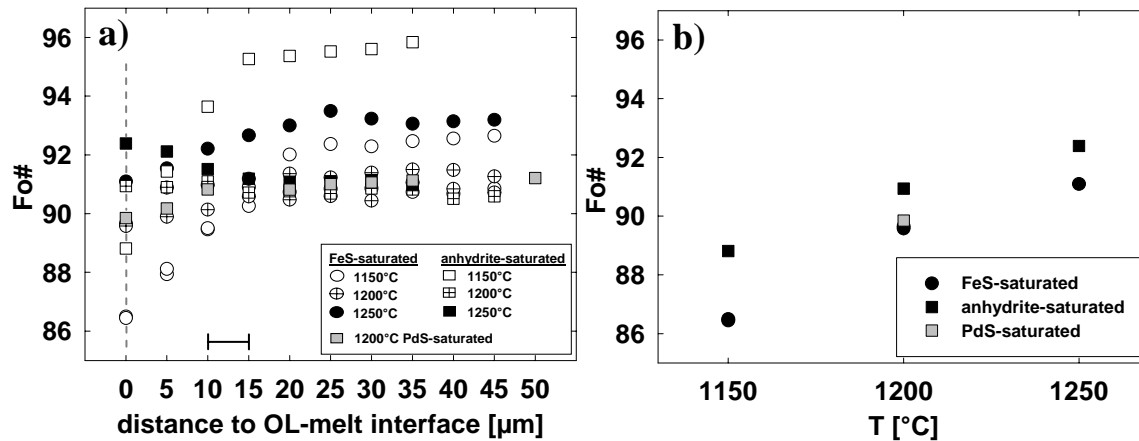


Fig.3: The forsterite content shown as Fo# (with $Fo\# = 100 \times Mg/(Fe+Mg)$ [molar]) in the OL-capsules at different distances to OL-glass interface (a) and Fo# at a distance $<5 \mu m$ to OL-glass interface (b). The uncertainty of the position of the electron beam-spot shown in (a) was about $5 \mu m$ (indicated by less accurate OL-analyses for a distance $<5 \mu m$ to the glass interface). The vertical gray dashed line illustrates the position of OL-melt interface within the uncertainty of $5 \mu m$.

Thus, due to reaction between OL and melt, olivine rims become generally enriched in FeO (e.g., 4-11 wt.% FeO at exp. S26) and depleted in MgO (e.g., observed maximum in exp. S26: 53 to ~ 48 wt.% MgO) towards the OL-glass interface. The composition of OL in most experiments remains almost constant at distances $> 20 \pm 5 \mu m$ and corresponds to the initial composition of San Carlos olivine used for OL containers. At the interface with basaltic glass, the Fo# changes as a function of experimental temperature (Fig. 3b) and the most significant change in OL composition is observed in low-temperature runs (at $1150^\circ C$). It is remarkable that Fo# in anhydrite-saturated systems is in general about 1-2 units higher than in FeS-saturated systems indicating differences in the activity of Fe as a function of redox conditions.

4.4 Major element composition of experimental glasses

The major element compositions of experimental glasses are reported in Table 3. All samples have homogeneous glass composition. It varies from basalt to trachybasalt and the main compositional variations are observed for MgO, FeO, CaO and K_2O due to variations in

experimental temperature, added S-source and the material of the sample container (OL or Au) as reported in Table 3.

All glasses produced in OL containers are enriched in MgO (~8-14 wt.% MgO in OL containers vs. ~6 wt.% MgO in the starting glass). The MgO content correlates positively with temperature showing an approximately linear relationship (Fig. 4a).

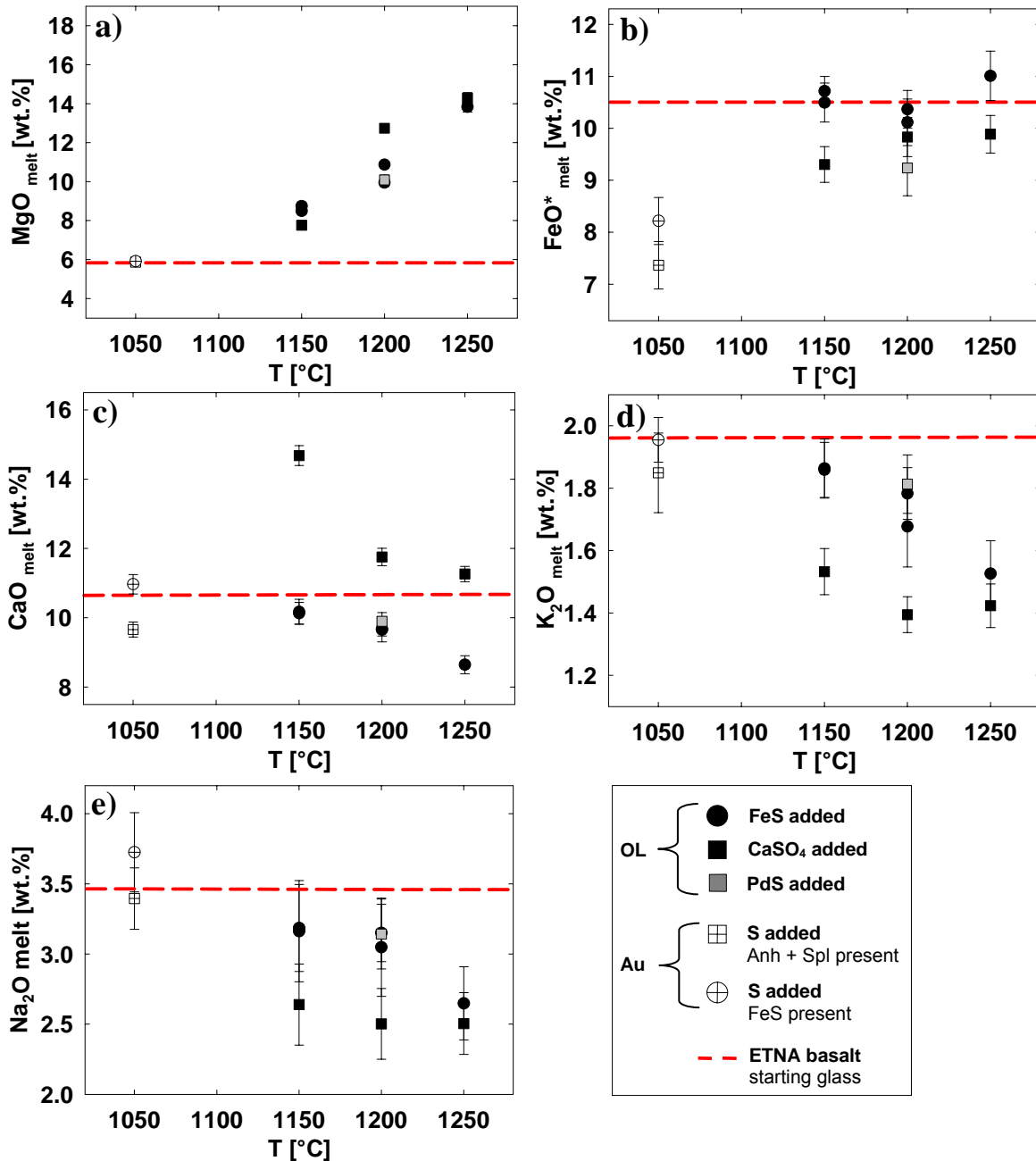


Fig.4: Concentrations of MgO (a), FeO (b), CaO (c), K₂O (d) and Na₂O (e) in the product glasses shown in dependence of temperature. The red dashed lines represent the concentration of the respective melt component in the Etna basalt starting glass. Note that the crossed symbols at 1050°C represent Au-capsule runs.

Melts in low temperature runs (1050°C) were significantly depleted in FeO for ~20 rel.% (FeS-saturated) and ~ 30 rel.% (anhydrite-saturated) as shown in Fig.4b. The lower FeO concentrations are due to formation of Fe-bearing phases like FeS and Fe-oxides (FeS at reducing conditions and spinel at oxidizing conditions). However, the FeO concentrations (10 to 11 wt.% FeO) in the glasses with added FeS are quite similar to that of the starting glass (~10.5 wt.% FeO), whereas glasses with added anhydrite are depleted in FeO by ~5-10 rel. %. The concentration of CaO in experimental glasses decreases with temperature in FeS-saturated experiments. Figure 4c, illustrates that at 1050°C the CaO content is similar to that of the starting material (11 wt.% CaO), whereas at 1250°C the glass contains about 20 rel. % less. On the contrary, the anhydrite-saturated glasses are either significantly enriched in CaO up to ~35 rel.%, if CaSO₄ was used as a S-source (OL-container runs) or depleted for about ~9 rel.% in CaO content, if elemental S was added as shown in Fig. 4c. Although the absolute CaO concentrations are different, trends of decreasing CaO with increasing temperature are observed for both FeS- and CaSO₄-saturated systems (Fig.4c).

It is noteworthy, that the highest CaO concentration is observed in the system with the highest added amount of CaSO₄ (exp. S26, 1150°C) (CaO-enrichment of about ~ 35 rel. %, as mentioned before). Most of the product glasses are depleted in K₂O and K₂O concentration negatively correlates with temperature. The lowest concentrations of K₂O (1.4-1.5 wt.% K₂O, depletion of ~ 25 rel.%) is observed in glasses coexisting with anhydrite phase (exp. S23, 1200°C and exp. S24, 1250°C). At 1050°C, the K₂O concentrations are similar to that of the starting glass. A similar trend as for K₂O is observed for Na₂O. At 1050 °C, Na₂O concentrations are similar to that in the starting glass and Na₂O decreases by ~25 rel. % with T in glasses coexisting with anhydrite phase.

4.5 Concentrations of dissolved H₂O

The H₂O concentrations of product glasses are listed in Table 3. The H₂O concentrations determined using “by difference” method range from 1.4 ± 0.7 (in S24 sample) to a maximum of 6.0 ± 0.7 (exp. 0_15 red) and 6.6 ± 0.7 wt.% H₂O (exp. 0_15 ox) in experiments conducted in the Au-capsules. However, H₂O concentrations determined by FTIR and KFT are about 1-2 wt.% less when compared with the “by difference” data (Fig. 5). It should be noted, that the bulk H₂O concentrations in Au-capsule runs (~ 11 wt.% bulk H₂O) was more than 2 times higher than that for OL-container runs (~ 4.7 wt.% bulk H₂O), where H₂O pre-saturated starting glass was used (Table 1).

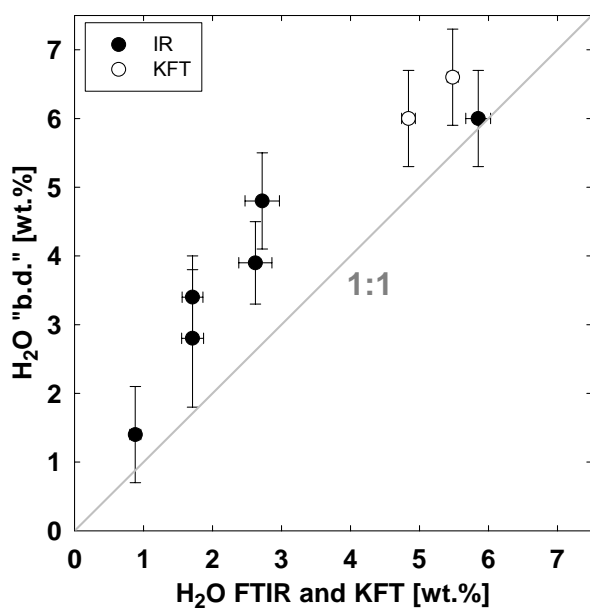


Fig.5: Measured H₂O concentrations of experimental glasses by KFT (Karl-Fischer-Titration) and FTIR (Fourier-Transformation Infrared Spectroscopy) plotted vs. H₂O concentrations determined by the “by difference”-method using electron microprobe analyses (EMPA).

Furthermore, in OL-container runs the anhydrite-saturated glasses ($\sim 3.9 \pm 0.6$ wt.% H₂O in exp. S24 and $\sim 4.8 \pm 0.7$ wt.% H₂O in exp. S23; except 1.4 ± 0.6 wt.% H₂O at S26) contain about 1-2 wt.% more H₂O than the FeS-saturated ones (from 2.8 ± 1.0 wt.% H₂O in exp. S2 to 3.5 ± 0.5 H₂O in exp. S18). The H₂O concentration profiles in the sealing-melt plug and in the sealing-melt seam (as illustrated in Fig.1d) were measured for exp. S2 and S8 using “by-difference” method to determine the extent of possible water loss from the OL container (Fig.

6a). The measured water concentrations show similar values, although in the exp. S8, the glass plug has slightly higher H₂O contents than the glass inside the OL-container (5.3 ± 0.7 vs. 3.4 ± 0.6 wt.% H₂O, respectively). Furthermore, H₂O concentrations increase in outward direction (Fig.6a). This indicates that outside the sample chamber H₂O was not in equilibrium with the hydrous S-rich fluid phase.

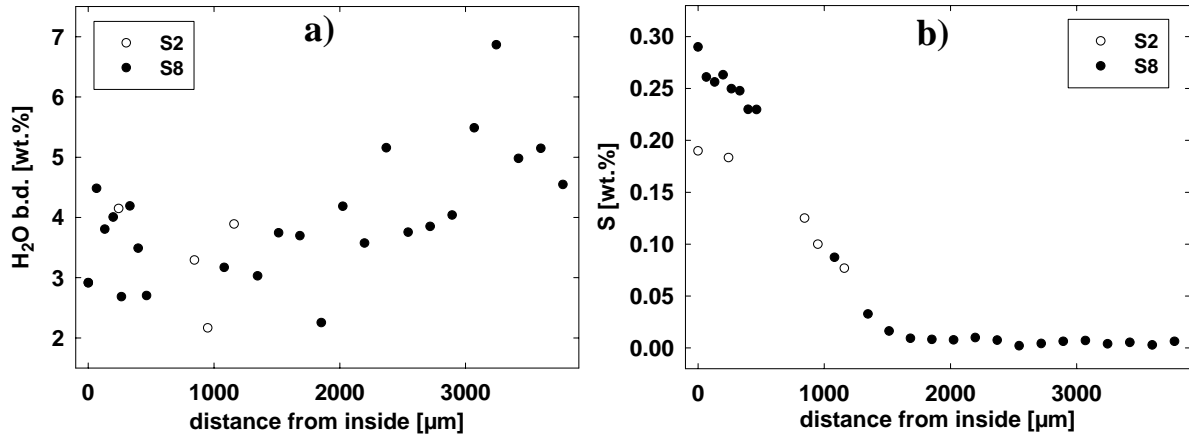


Fig.6: Measured profiles along the sealing-melt seam (exp. S2: PdS-saturated and S8: FeS-saturated) up to the sealing-melt plug (S8). Both experiments were performed at 1200°C, 48 h run duration. The H₂O concentrations were determined by the “by difference”-method using the EMPA (a). The S-concentrations in the glasses were also measured within the same profiles (b) “distance from inside” means the distance from the analyzed point from the profile start at the beginning of the sealing-melt seam close to the end of the sample chamber.

4.6 Redox conditions in the experiments

The experimental redox conditions (fO_2) were estimated from the $\Delta \lambda$ (S K α) peak shift as described above and the results are listed in Table 3. The FeS-saturated glasses are significantly more reduced than the anhydrite-saturated ones. The S⁶⁺/ΣS ratio ranges between 0.08 and 0.16 in FeS-saturated glasses resulting in calculated variations of $\log fO_2$ in the range from ~FMQ to FMQ+0.3 (± 0.4 log units) and between 0.71 and 0.95 in anhydrite-saturated glasses resulting in $\log fO_2$ values in the range from ~FMQ+1.4 to FMQ+2.2 (± 0.2 log units). In addition, for the experiment 0_15 red, the $\log fO_2$ was determined to be ~FMQ+0.3, whereas the fO_2 , calculated from the measured partial pressure of hydrogen (PH₂) using Shaw membrane of the IHPV, was

$\sim\text{FMQ}+0.7$ (assuming water-saturated conditions). The $\text{S}^{6+}/\Sigma\text{S}$ ratio of the PdS-saturated glass (exp. S2) was determined to be 0.66 resulting in $\log f\text{O}_2 \sim\text{FMQ}+1.2$ (± 0.2 log units) and thus, reflecting more oxidizing conditions than that of the FeS-saturated experiments.

The fugacities of sulfur range from about -0.1 to 0.6 at FeS-saturation (calculated by Bockrath et al., 2004, corrected by Liu et al., 2007) as reported in Table 4.

4.7 Concentrations of dissolved S in basaltic glasses - dependence on T and $f\text{O}_2$

In order to check the possible loss of S from the OL container, S concentrations were measured in the sealing-melt plug outside the OL container (as described above) in exp. S8 (FeS-saturated). The concentration of sulfur in the glass of the sealing-melt plug was below detection limit. The concentration profiles measured in the sealing-melt seam in inward to outward direction at exp. S2 (PdS-saturated) and exp. S8, both conducted at 1200°C , are illustrated in Fig.6b. Starting at the beginning of the seam close to the sample chamber, the S concentration in exp. S2 decreases for a distance of about $1200 \mu\text{m}$ (about $1/3$ of piston length) from 0.22 to 0.08 wt.% S. The S concentration in exp. S8 decreases from 0.30 ± 0.04 wt.% S to the values below detection limit over a length of about $2400 \mu\text{m}$ (while the total profile length was $4800 \mu\text{m}$). Thus, although S diffuses from the interior of OL containers through the sealing-melt seam, the S loss is a relatively slow process even at high temperatures. Due to the small sectional area of the melt seam ($\sim 0.46 \text{ mm}^2$) being about $\sim 7\%$ to that of the sample chamber it is expected that the total mass of potential S-loss should be low. Therefore an attainment of local equilibrium inside the container can be assumed.

The S concentrations of product glasses range between 0.12 ± 0.01 and 1.08 ± 0.04 wt.% S and they are strongly dependent on run temperature and oxidation state of the glass shown in Fig.7a and 7b, respectively (see also Table 3).

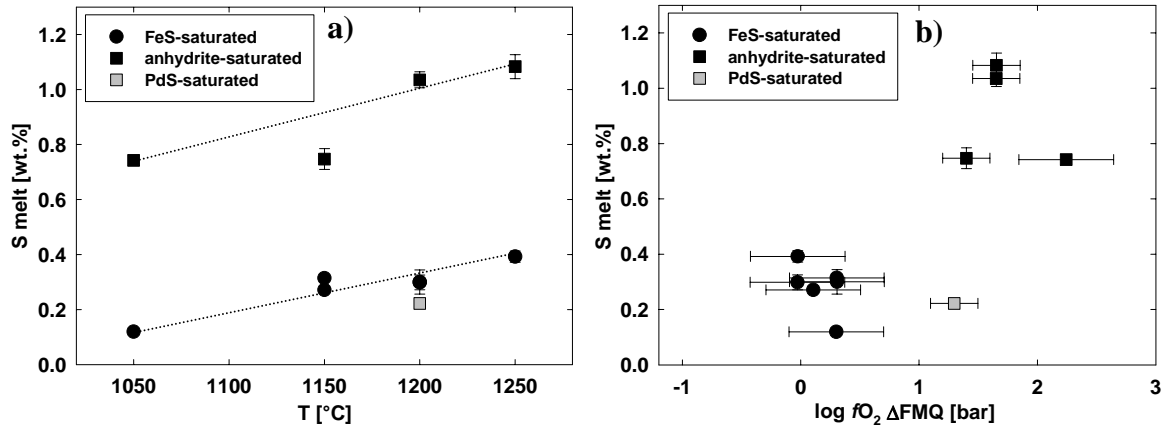


Fig.7: S concentration of experimentally obtained FeS-saturated, anhydrite-saturated and PdS-saturated basaltic glasses vs. experimental temperature (a) and fO_2 (by S K α peak shift) in $\Delta\log$ FMQ [bar] (b).

At anhydrite-saturated conditions (i.e., at $\log fO_2$ from \sim FMQ+1.4 to FMQ+2.2), S concentrations in melts are about 4-5 times higher, than that at FeS-saturated conditions (\sim FMQ). At both conditions, S concentration in glass correlates positively with temperature (Fig.7a). In FeS-saturated glasses, S concentration increases linearly from 0.12 ± 0.01 to 0.39 ± 0.02 wt.% S with increasing temperature from 1050°C to 1250°C. In anhydrite-saturated systems, a similar temperature dependence is observed with S concentration in the glass increasing from 0.74 ± 0.01 wt.% S at 1050°C to a maximum of 1.08 wt.% S at 1250°C. The PdS-saturated glass obtained at 1200°C contains slightly lower S content when compared with the FeS-saturated glass at the same temperature (0.22 vs. 0.30 ± 0.04 wt.% S, respectively). It is noteworthy, that the oxidation state of PdS-saturated glass was determined to be about 1 log higher than that of the FeS-saturated glass at 1200°C (Fig.7a). The reproducibility of the experimental data on S solubility was verified by two duplicated FeS-saturated runs conducted at 1150°C and 1200°C. The basaltic glasses obtained at both temperatures show S concentrations within the uncertainty of analytical methods (i.e., 0.27 ± 0.01 and 0.31 ± 0.01 wt.% S at 1150°C; 0.30 ± 0.04 and 0.30 ± 0.03 wt.% S at 1200°C) as evident from Fig.7a.

5. Discussion

To our knowledge, we present the first experimental data for sulfide and sulfate solubility in hydrous basaltic melts in the temperature interval from 1050 to 1250°C being relevant for storage conditions of most natural basaltic magmas (e.g., for Mt.Etna magma: Archambault & Tanguy, 1976; Clocchiatti & Métrich, 1984; Métrich 1985; Kamenetzkiy et al., 1986; Métrich & Clochiatti, 1989).

5.1 Attainment of equilibrium: Fe-Mg exchange reactions between OL containers and basaltic melts

The achievement of local equilibrium conditions between OL (capsule, piston, disk) and melt phases at OL-melt interface is indicated by the observation that $K_D^{\text{Fe-Mg}/\text{OL-melt}}$ values ($K_D^{\text{Fe-Mg}/\text{OL-melt}} = [X_{\text{FeO}}^{\text{OL}} * X_{\text{MgO}}^{\text{melt}}] / [X_{\text{FeO}}^{\text{melt}} * X_{\text{MgO}}^{\text{OL}}]$, [molar]) are calculated to be in the relatively narrow range between 0.25 and 0.34 as illustrated in Fig. 8. The $K_D^{\text{Fe-Mg}/\text{OL-melt}}$ values converge at the interface to the value of ~0.3 which is in agreement with the prediction of Roeder & Emslie (1970) for the OL – melt equilibrium.

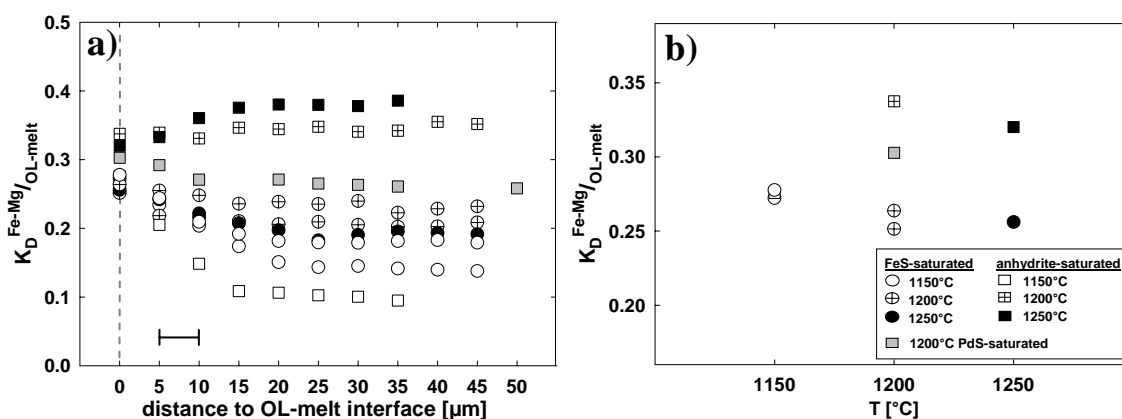


Fig.8: Distribution coefficient of Fe and Mg between OL and melt $K_D^{\text{Fe-Mg}/\text{OL-melt}}$ calculated by Roeder & Emslie (1970) ($K_D^{\text{Fe-Mg}/\text{OL-melt}} = [X_{\text{FeO}}^{\text{OL}} * X_{\text{MgO}}^{\text{melt}}] / [X_{\text{FeO}}^{\text{melt}} * X_{\text{MgO}}^{\text{OL}}]$, [molar]) as a function of distance to OL-melt interface (a) and as a function of temperature at OL-melt interface (b); other symbols s. Fig.3.

However, $K_D^{\text{Fe-Mg}/\text{OL-melt}}$ varies with temperature, $f\text{O}_2$ (Fig.8) and melt composition. Using the model of Toplis (2005) which provides correction for $K_D^{\text{Fe-Mg}/\text{OL-melt}}$ according to the melt SiO_2 , Na_2O and K_2O concentrations, H_2O content, T and P, the calculated $K_D^{\text{Fe-Mg}/\text{OL-melt}}$ values are in the range from 0.27 to 0.28 at FeS-saturation and from 0.26 to 0.29 at anhydrite-saturation. These values agree with the data from previous experimental crystal-melt equilibrium studies ($K_D^{\text{Fe-Mg}/\text{OL-melt}}$ of $\sim 0.25\text{-}0.35$) using basaltic compositions (e.g., Gaetani & Grove, 1998; Gaetani & Watson, 2002; Berndt et al., 2005; Feig et al., 2006, 2010; Botcharnikov et al., 2008). For instance, Berndt et al. (2005) proposed an expression for the relationship between Fo# of OL and Mg# of the melt ($\text{Mg\# melt} = \exp[(\text{Fo\#} + 71.8)/37.54]$) which can be satisfactorily applied to our data. Thus, we can conclude that the investigated systems provide constraints on the equilibrium solubility of sulfide and sulfate in olivine-saturated magmas as a function of temperature.

5.2 Sulfide and sulfate solubility in OL-saturated basaltic magmas

5.2.1 S concentration of the FeS-saturated melts as a function of T, $f\text{O}_2$ and $f\text{S}_2$

The concentration of S in basaltic melts coexisting with FeS increases with increasing temperature, oxygen and sulfur fugacities as illustrated in Figs.9, 10 and 11, respectively. The obtained data are compared with experimental results on sulfur solubility in basaltic melts from other studies showing a general agreement on the effects of T, $f\text{O}_2$ and $f\text{S}_2$ on concentrations of dissolved S. It must be emphasized that the difference in T dependence of S solubility between the results of our study at 200 MPa and the data obtained at 1 GPa in graphite-bearing systems (Jugo et al., 2005a; Liu et al., 2007), as shown in Fig.9, can be explained simply by the difference in the redox conditions (Fig.10).

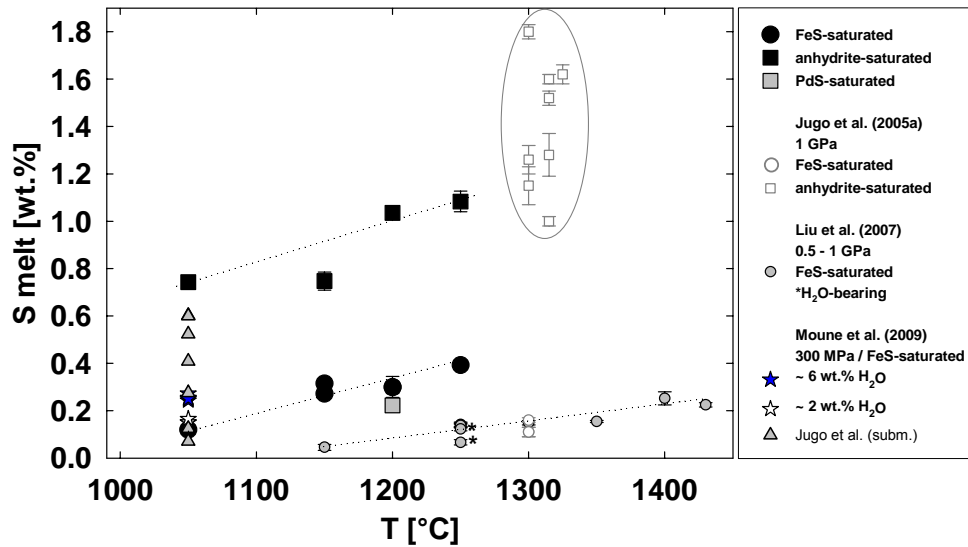


Fig.9: S concentration of experimentally obtained FeS-saturated and anhydrite-saturated basaltic glasses vs. experimental temperature. Data of Jugo et al. (2005a) and Liu et al. (2007) are mainly anhydrous, data of Moune et al. (2009) contain ~2 and ~6 wt.% H₂O. The dashed lines are “guides to the eye” illustrating the increase of S solubility with temperature being approximately similar in our study for both FeS-saturation and anhydrite-saturation (~0.15 wt.% S/100°C), where the T-dependence on S solubility for FeS-saturated data of Liu et al. (2007) (small grey filled dots) is less. It is noteworthy, the FeS-saturated data of Jugo et al. (2005a) at 1300°C (small open gray dots) fit to data of Liu et al. (2007). The grey ellipse covers data of Jugo et al. (2005a) for anhydrite saturation.

It is noteworthy that there is a theoretically slight positive effect of P on fS_2 (~0.3 log units higher at 1 GPa compared to 200 MPa (Liu et al., 2007)), however the lower absolute values of S concentration and the different slope of the trend can be in contrast attributed to the negative pressure effect on sulfide solubility (Mavrogenes and O'Neill, 1999). At the moment, it is not possible to unambiguously distinguish between the effects of both factors, i.e., fO_2 and P. It must be also noted that the experiments in piston cylinder apparatus (Jugo et al., 2005a; Liu et al., 2007) were conducted in graphite-saturated systems, implying that carbon species may affect the fugacity of S species in the system and hence, S solubility in the melt. Such an effect is confirmed by the general positive trend of S concentration versus fS_2 shown in Fig.11. Moreover, based on the experimental data on sulfide solubility in basaltic melts of Mt.Etna (Liu et al., 2007) and Hekla volcano (Moune et al., 2009) it was suggested that at given conditions water can have a positive effect on concentrations of dissolved S (Moune et al., 2009).

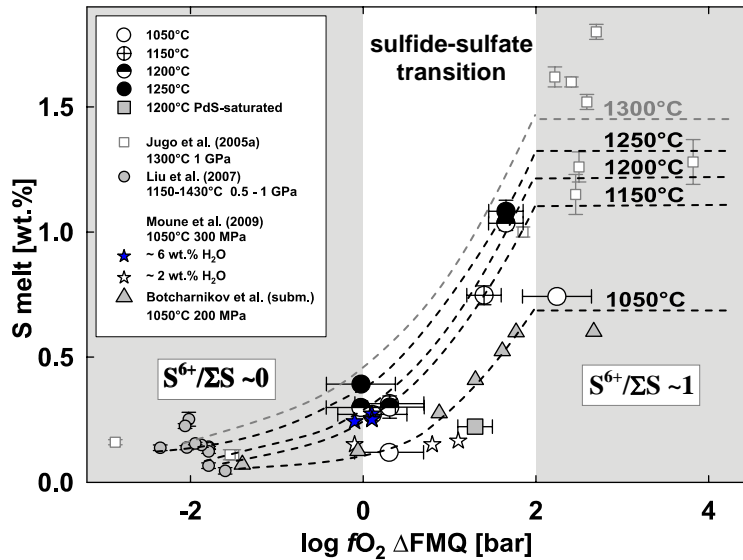


Fig.10: S solubility in basaltic melts as a function of fO_2 . Also plotted are data for Etna basalt of Liu et al. (2007) and Botcharnikov et al., *subm.* and Jugo et al. (2005a) for microbasalt-basalt and Moune et al. (2009) for Hekla basalt. Based on the data of Botcharnikov et al., *subm.*, we estimated the increase in S solubility with fO_2 at fixed T, as represented by the dashed lines.

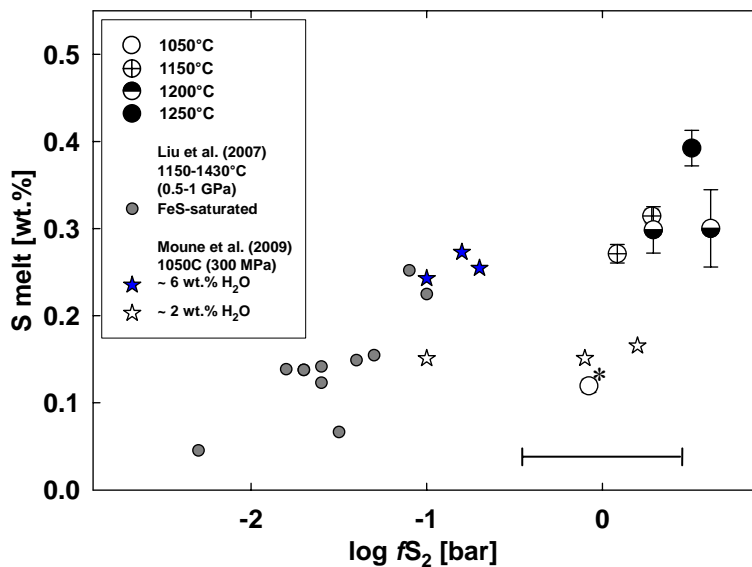


Fig.11: S concentration at FeS-saturation in basaltic melts as a function of fS_2 , calculated by Bockrath et al. (2004) corrected by Liu et al. (2007). Data are shown for our experiments and those of Liu et al. (2007) and Moune et al. (2009); * fS_2 additionally calculated by the method of Toulmin & Barton (1964) to be -1.0 ± 0.9 (exp. 0_15_2 red, 1050°C, \sim FMQ+0.3).

Our S solubility data at 1050°C, 200 MPa and $\log fO_2 \sim$ FMQ+0.3 (exp. 0_15_2 red with 4.84 ± 0.10 wt.% H_2O) are similar to the data of Moune et al (2009) at 1050°C, 300 MPa and $\log fO_2 \sim$ FMQ for Hekla basalt containing ~ 2 wt.% H_2O but significantly lower than that for basalt containing ~ 6 wt.% H_2O (Fig.9). The observed difference in the data obtained at similar conditions can be attributed to the difference in the compositions of investigated basaltic melts, i.e., Hekla basalts are significantly enriched in FeO (11.5-14.4 wt.% FeO) when compared with the basalt from Mt.Etna (10.5 wt.% FeO). This may explain the higher S solubility because Fe concentration of the melt is known to be a factor positively influencing S solubility at given

conditions (e.g., O'Neill & Mavrogenes, 2002). Nevertheless, the fact that most basalts from the studies of Jugo et al. (2005a) and Liu et al. (2007) with the same or similar FeO content were nominally water-free can explain in part the observed lower solubility values of S in water-poor melts.

5.2.2 S concentration in the melt at PdS-saturation

The determined S concentrations in melts at given T (1200°C) is about 30 rel. % lower at PdS-saturation than at FeS-saturation, although the PdS-saturated experiment shows higher $S^{6+}/\Sigma S$ ratio ($\sim 66 \pm 13$ % vs. $\sim 8-16 \pm 13$ %). A possible reason for lower S concentrations at PdS saturation can be a difference in fS_2 imposed by the PdS-saturated system related to the FeS-saturated system. This is confirmed, for instance, by the experiments of Mysen & Popp (1980) who adjusted fS_2 in the system by using PtS-Pt-, Ag_2S -Ag- and Cu_2S -Cu-buffer assemblages. Although it was not possible to determine the fS_2 in PdS-saturated system, we can suggest that it was sufficiently lower than that in FeS-saturated systems explaining lower S solubility.

5.2.3 S concentration in the melt at anhydrite-saturation

The $CaSO_4$ -saturated basalts also show a positive dependence of S solubility on temperature with a trend parallel to that in FeS-saturated systems (Fig.9). There are only few data in the literature on sulfate solubility in basaltic magmas. Jugo and coauthors (2005a) reported S solubility values after experiments at T = 1300-1325°C and P=1 GPa. However, as illustrated in Figs.9 and 10, their data show an extremely wide scattering from 1 to 1.8 wt% S at given conditions. This scattering can be presumably attributed to the fact that authors used AuPd capsules in experiments with duration of 2 to 6 h only. Despite the high temperature of the runs, these short-time experiments seem to be insufficient to achieve equilibrium in terms of S partitioning between coexisting phases. Thus, the actual equilibrium S solubility at high

temperatures ($>1250^{\circ}\text{C}$) and pressures (>200 MPa) is still needed to be determined. Consequently, the application of recent models on anhydrite solubility in basaltic magmas, based on those experimental data (e.g., Jugo, 2009; Li & Ripley, 2009), should be done with caution (see also §5.4).

5.3 Sulfur speciation and redox conditions of sulfide- and sulfate-saturated melts

The observed higher solubility of S in anhydrite-saturated magmas in comparison with that of the FeS-saturated magmas is attributed to a generally higher solubility of S sulfate species in most silicate melts (e.g., Carroll and Rutherford, 1987, 1988; Luhr, 1990; Jugo et al., 2005a,b; submitted) except some exotic silica-rich compositions as reported by Scaillet and Macdonald (2006). Several recent studies have proven that S is present in silicate melts as two main species S^{2-} and S^{6+} (e.g., Wilke et al., 2008; Evans et al., 2009; Metrich et al., 2009; Jugo et al., *subm.*), whereas other species (e.g., Metrich et al., 2002) are analytical artifacts or they are present in negligible amounts (e.g., Wilke et al., 2008). The transition from sulfide- to sulfate-dominated speciation of S in silicate melts with increasing $f\text{O}_2$ occurs over a very narrow range of redox conditions. The entire species transformation in melts completes in the range of $\log f\text{O}_2$ between FMQ to FMQ+2 (Jugo et al., *subm.* and references therein).

The results of this study indicate that the transition from FeS-saturation to anhydrite-saturation occurs at $\log f\text{O}_2$ from $\sim\text{FMQ}+0.3$ (± 0.4 log units) to $\sim\text{FMQ}+1.4$ (± 0.2 log units) as illustrated in Fig.12. It must be noted that both S-bearing phases can coexist at the redox conditions of sulfide-sulfate transition as observed in many natural volcanic rocks [e.g., dacites-trachyandesites of Pinatubo (Westrich & Gerlach, 1992), trachyandesites of El Chichón volcano (Luhr, 1984), andesites of the Fish Canyon System (Huerto Andesite), San Juan Volcanic Field (Parat et al., 2005)]. Moreover, coexisting FeS and anhydrite were reproduced in experiments

with El Chichón trachyandesite (Carroll & Rutherford, 1987) and with Huerto andesite (Parat et al., 2008).

Because our data on $\log fO_2$ were calculated from the determined S speciation, we made an attempt to estimate the redox conditions by an independent method. The ratios of Fe^{3+} to total iron ($Fe^{3+}/\Sigma Fe$) in the sample glasses were determined for the two FeS-saturated runs (exp. S20, S21) and for the two anhydrite-saturated runs (exp. S23, S24) using Mössbauer milliprobe at Bayerisches Geoinstitut (Bayreuth, Germany). The analytical technique is described in detail by Botcharnikov et al. (2005). The $Fe^{3+}/\Sigma Fe$ ratios were measured to be 0.22 and 0.23 ± 0.03 in glasses at FeS-saturation (S20, S21, respectively) and to be 0.31 and 0.29 ± 0.03 at anhydrite-saturation (S23, S24). Based on the determined $Fe^{3+}/\Sigma Fe$, the oxygen fugacity was calculated using the equation of Nikolaev et al. (1996) and the model of Kress and Carmichael (1991). The calculated fO_2 values are reported in Table 5 and plotted in Fig.12. It is remarkable that the model of Nikolaev et al. (1996) predicts redox conditions similar to those calculated from the S speciation data (eq.2) for the FeS-saturated systems, whereas the model of Kress and Carmichael (1991) shows better agreement for the systems saturated with anhydrite.

Table 5: Comparison of fO_2 determined by S ($K\alpha$) peak shift at EMPA and calculated fO_2 using the models of Nikolaev et al. (1996) and Kress & Carmichael (1991) based on Fe^{3+}/Fe_{tot} -ratio ($Fe/\Sigma Fe$) determined by Mössbauer spectroscopy.

Run#	EMPA ΔQFM	N ΔQFM	K & C ΔQFM	Mössbauer $Fe^{3+}/\Sigma Fe$
FeS-saturated				
S20	0.1 (8)	0.1	0.8 (5)	0.22 (3)
S 21	0.0 (8)	0.3	1.2 (5)	0.23 (3)
anhydrite-saturated				
S23	1.7 (3)	1.1	1.9 (10)*	0.31 (3)
S24	1.7 (3)	0.9	1.7 (10)*	0.29 (3)

Notes: ΔQFM is the $\log fO_2$ [bar] relative to that of the QFM-buffer reaction. N is the result of the equation of Nikolaev et al. (1996). K & C is the result by the equation of Kress & Carmichael (1991). $Fe^{3+}/\Sigma Fe$ is the ratio of Fe^{3+} to total Fe. *error can exceed 1 log unit at $fO_2 > \sim FMQ + 1$.

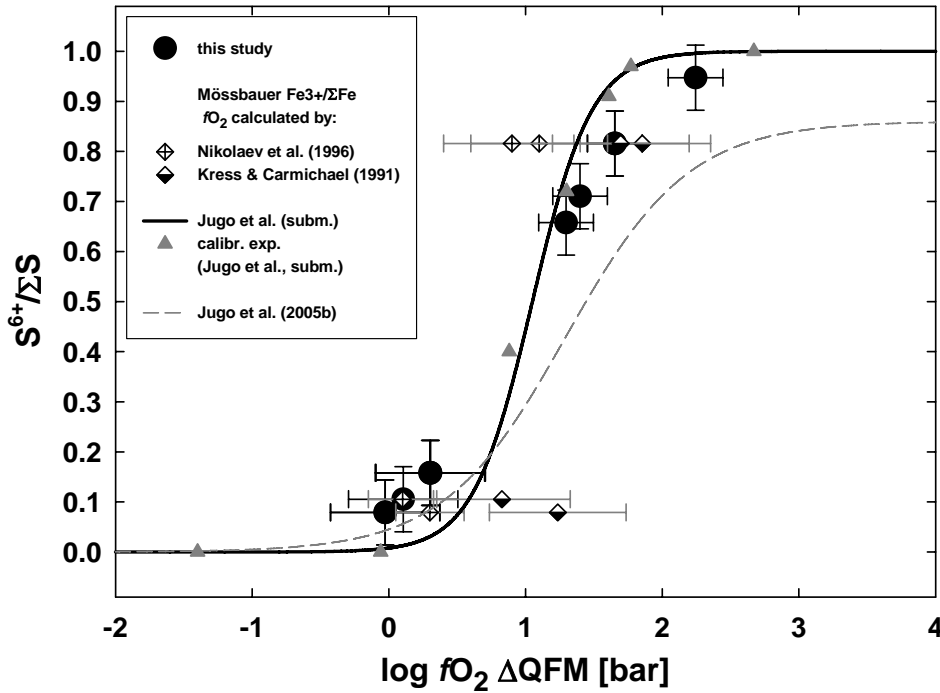


Fig.12: Comparison of fO_2 deriving from $S^{6+}/\Sigma S$ ratios ($S^{6+}/\Sigma S$ ratios via S $K\alpha$ peak shift-method given by Carroll & Rutherford, 1988 and fO_2 calculated by the method of Wallace & Carmichael, 1994) and fO_2 calculated by the eq. of Nikolaev et al. (1996) (crossed diamonds) and Kress & Carmichael (1991) (bottom filled diamonds) using $Fe^{3+}/\Sigma Fe$ ratios determined by Mössbauer spectroscopy. Note that our data show a good correspondence to the S-speciation curve provided by Jugo et al. (subm.) deriving from XANES analysis, where the grey triangles represent experimental data used for calibration of the curve. Also shown is the S-speciation curve of Jugo et al. (2005b) obtained by S $K\alpha$ peak shift (thin gray dashed curve).

Thus, owing to a common large deviation of the modelled fO_2 values from those determined experimentally (about 1 logarithmic unit; see comparison of the data by Partzsch et al., 2004), we can conclude that the estimates on fO_2 from Mössbauer data are in general agreement with the calculations from S speciation by equation (2).

Furthermore, our data show a good correspondence with the recent experimental data and the model provided by Jugo et al. (subm.). It was demonstrated that the S speciation data obtained by S ($K\alpha$) peak shift method using EMPA may overestimate $S^{6+}/\Sigma S$ ratio at $\log fO_2 < \sim FMQ+0.7$ and significantly underestimate $S^{6+}/\Sigma S$ ratio at $\log fO_2$ above $\sim FMQ+1$ due to the beam damage. The new trend of S speciation as a function of $\log fO_2$ curve was derived from the measurements by XANES and can be expressed as (Jugo et al., subm.):

$$S^{6+}/\Sigma S = 1/(1+10^{(2.1-2\Delta FMQ)}) \quad (3),$$

Both the EMPA and the XANES curves are plotted in Fig.12 to illustrate the difference between actual and apparent speciation of S. It must be noted that the data obtained in our study agree within the uncertainties with the new model derived from XANES analysis demonstrating, however, a tendency to overestimate and underestimate the $S^{6+}/\Sigma S$ ratio at reducing and oxidizing conditions, respectively. The better agreement with the model is attributed presumably to the analytical technique used in this study, i.e., to the fact that the electron beam was continuously moved over the glass sample to minimize the imposed beam damage. This approach obviously shows reliable results.

5.4 Redox and temperature control on S solubility in basaltic magmas

Several models were proposed in the literature in attempt to predict the solubility of S in natural magmas. However, due to a relatively small number of available data covering a wide range of magmatic conditions and compositions, the calibration and hence the success of the models is significantly limited. Figure 13 illustrates the comparison between measured and predicted concentrations of dissolved sulfur using two recent models (Liu et al., 2007; Li & Ripley, 2009) for sulfide- and sulfate-saturated basaltic magmas. Both models significantly underestimate S concentrations in sulfide-saturated basaltic liquids (Fig.13a), whereas the model of Li & Ripley (2009) overestimates S content in anhydrite-saturated magmas (Fig.13b). The observed significant discrepancy between the experimental data and the models indicates that the models should be recalibrated for more accurate predictions of S solubility.

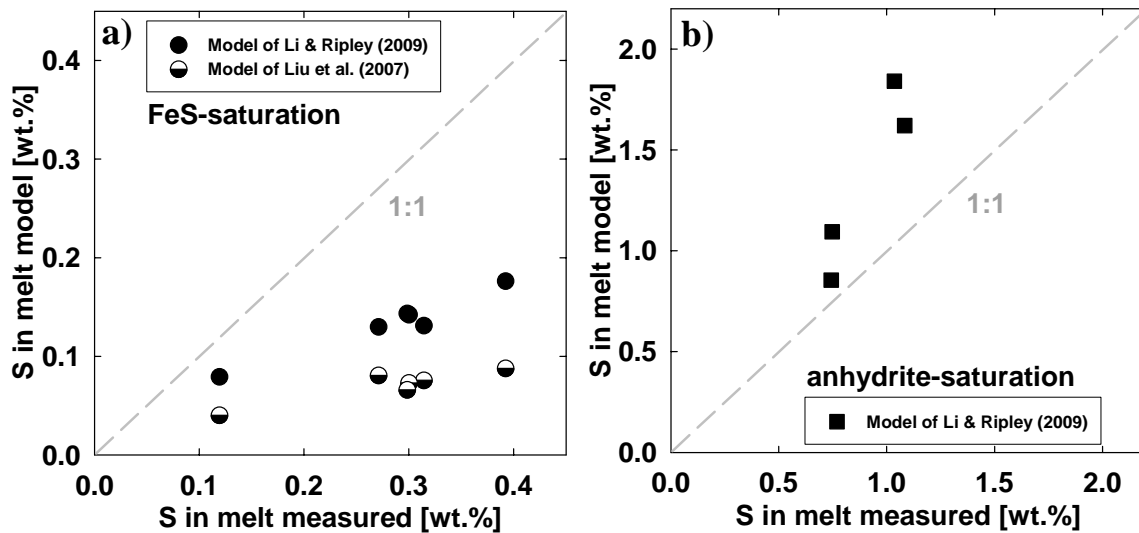


Fig.13: Comparison between the measured S concentration in our sulfide- and sulfate saturated melts and the predicted concentrations of dissolved sulfur by using the models of Liu et al. (2007) and Li & Ripley (2009) for sulfide-saturated (a) and the model of Li & Ripley (2009) for sulfate-saturated basaltic magmas.

The experimental data obtained at different temperatures and for different melt compositions, illustrated in Fig.10, show solubility trends as a function of fO_2 and temperature. The trends for our data are interpretative and they are constrained following the general logic in the evolution of trends from other studies, mainly from the recent work of Jugo et al. (subm.). This diagram clearly illustrates (1) an exponential increase in S solubility with fO_2 and (2) a strong positive dependence of the S concentration on temperature. The exponential shape of the trends is attributed to a rapid change in S speciation at sulfide-sulfate transition and to the significantly higher sulfate solubility in melts when compared with that of sulfide, as discussed above. This compilation of the data gives estimates on the effects of temperature and redox conditions on the behavior of S species in basaltic melts and provides general constraints on the solubility laws of S, necessary to evaluate conditions and to interpret magmatic processes in natural systems.

5.5 Application of the experimental data to natural magmatic systems

Our results demonstrate that at geologically relevant storage conditions of basaltic magmas (i.e., $T \sim 1050\text{-}1250^\circ\text{C}$, $P \sim 200\text{-}300$ MPa and $\sim 1\text{-}6$ wt.% H_2O dissolved in the melt) the solubility of sulfide and sulfate in basaltic melts is strongly dependent on T and $f\text{O}_2$. For instance, cooling a S-saturated basaltic magma for about 100°C in the T range from 1050°C to 1250°C at constant $f\text{O}_2$ is expected to reduce S concentration in the magma by ~ 0.15 wt.% S (Figs. 9 and 10). Such a dramatic decrease in S solubility will trigger precipitation of S-rich mineral or melt phases or/and effective S degassing from the magma. The processes of S release from the melt will be even enhanced due to progressive magma crystallization with decreasing temperature because S solubility decreases with change in melt composition from basalt to rhyolite. This scenario of magma evolution at Hekla volcano was discussed in detail by Moune et al. (2009) based on the experimental solubility data and composition of melt inclusions. It was shown that S content of sulfide under-saturated basalts increased with differentiation to basaltic andesite until the sulfide saturation was reached. With further magma evolution, S concentration in the melt was controlled by sulfides and later by magma degassing (Moune et al., 2006, 2009). Moreover, since the solubility of S is also a function of redox conditions, the variation in $f\text{O}_2$ for about 0.5 log units around FMQ+1 will change S solubility depending on the direction of the $f\text{O}_2$ change. At high temperatures ($1150\text{-}1250^\circ\text{C}$), the S solubility decreases by about ~ 25 rel.% and decreases for about 35 rel.% at 1050°C by changing $f\text{O}_2$ from FMQ+1 to FMQ+0.5 (Fig.10). If $f\text{O}_2$ increases from FMQ+1 to FMQ+1.5 the S solubility increases for about 30 rel.% at high temperatures ($1150\text{-}1250^\circ\text{C}$) and increases for about 45 rel.% at 1050°C . The fact that the increase in S solubility is higher by changing $f\text{O}_2$ from FMQ+1 to more oxidizing can be explained by the increase of sulfate species and their high contribution to the total S solubility (Jugo et al., 2009, *subm.*)

The fact that our experiments simulated temperature evolution of olivine-saturated S-rich basaltic melts has an advantage for the application of our results to the understanding of

magmatic processes in olivine-bearing magmas. Hence, the results are of great importance for the interpretation of compositional signatures in olivine-hosted melt inclusions representing preserved small volumes of original magmas. In particular, there is a large database on the major-element and volatile composition of basaltic melts trapped in melt inclusions in olivines from Mt.Etna (e.g., Métrich & Clocchiatti, 1989; Métrich et al., 1993, 2004; Spilliaert et al., 2006; Métrich & Wallace, 2008; Corsaro et al., 2009). Here we provide estimates on the temperatures and redox conditions of magmas from Mt.Etna using our experimental data and compare them with the data obtained by other methods.

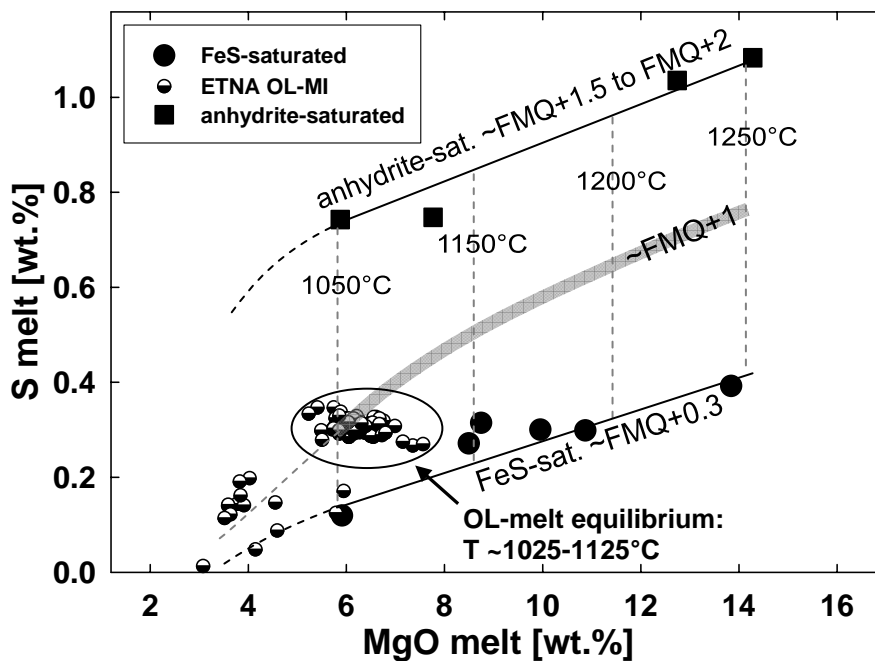


Fig.14: MgO melt as an indicator for T with respect to OL-saturated basaltic melts of Mt.Etna vs. the S solubility at FeS-saturation (\sim FMQ+0.3) and anhydrite-saturation (\sim FMQ+1.5 to \sim FMQ+2) (black lines). The bold grey curve represents the S solubility at FMQ+1 (as estimated in our study, Fig.10), where the dotted extensions of curve and lines represent the expected trend in S solubility with T decreasing to values below 1050°C. The vertical grey dotted lines representing T isotherms in OL-saturated magmas (as described in the text). The bottom filled dots plot for the composition of natural Mt.Etna OL-MI (olivine melt inclusions) of the 2001-2002 eruption published by Spilliaert et al. (2006a). The ellipse covers volatile-rich primitive MI estimated to be in equilibrium with host OL at T \sim 1025-1125°C. The temperature of Mt.Etna's higher evolved MI and glass embayments depleted in MgO and S, being in some cases sulfide-saturated (Métrich et al., 2004) can be estimated to values \leq \sim 1000°C.

It must be noted that the analysis of S speciation in melt inclusions is a challenging task because of their small size typically in the range of 10-100 μ m. It precludes the direct application

of the technique when the electron beam of EMPA is continuously moved over the fresh, undamaged part of the sample. The XANES facility is difficult to access and this analysis is not a routine method yet. Hence, the redox conditions of magmas trapped in melt inclusions can not be easily evaluated. In the Fig.14 we propose a simple empirical method for the estimation of magmatic temperatures and fO_2 in olivine-saturated basaltic magmas. Since MgO content of the melt is a direct manifestation of the magma temperature in OL-saturated systems, it can be used as a temperature index. Note that the MgO content of our experimental glasses and OL-saturated samples investigated by Jugo et al. (subm.) does not show significant variation as a function of redox conditions. Thus, vertical lines in Fig.14 can be assumed as representing isotherms in OL-saturated magmas. The expected change in redox conditions with temperature and MgO of the melt is shown as a thick grey line illustrating conditions at $\log fO_2 \sim FMQ+1$. This estimate is based on the solubility values of S at various T and fO_2 and, hence, is valid for S-saturated conditions.

Juvenile volatile-rich melts of Mt.Etna (which are free of condensed S-bearing phases) contain about 0.3-0.35 wt.% S and 2.3 wt.% H_2O (and 0.2 wt. % CO_2). Magmatic T and P of primitive volatile-rich magma of Mt.Etna was estimated to be 1100-1150°C and 200-300 MPa, respectively (Archambault & Tanguy, 1976; Clocchiatti & Métrich, 1984; Métrich 1985; Kamenetzkiy et al., 1986; Métrich & Clochiatti, 1989). Those melts are supposed to exist under relatively oxidizing conditions of about FMQ+1 (Métrich & Clochiatti, 1989). Métrich & Clocchiatti (1996) determined $S^{6+}/\Sigma S$ ratios in primitive melts trapped in OL (1989-1990 eruption) to be $\sim 0.44 \pm 0.07$ (by S ($K\alpha$) peak shift method) which also correspond to FMQ+1. A second group of melt inclusions represent partially degassed magma with $\sim 3-5$ wt.% MgO and < 0.15 wt.% S. The concentrations of MgO and S measured in melt inclusions are plotted in Fig.14. An evaluation of T and fO_2 for the natural data by our empirical method is in excellent agreement with the estimates provided by other methods (see above) assuming that parental magmas of Mt.Etna were close to S saturation. It is noteworthy that the second group of melt

inclusions is plotted at lower MgO and S contents indicating lower temperatures and fO_2 moderately varying around FMQ+1. The very low concentrations of S may indicate magma degassing processes. Slightly more reduced conditions than FMQ+1 for strongly S-degassed melts is confirmed by the presence of sulfides (Metrich et al., 2004). A good agreement between the predictions of our empirical method and the predictions from other methods imply that such an approach can be used to evaluate the temperatures and redox conditions of S-rich OL-saturated magmas between 1000 and 1300°C and $\log fO_2$ between \sim FMQ and FMQ+2. The only information which is required are the data on concentrations of MgO and S in basaltic melts.

6. Conclusions

Our developed double capsule technique with an OL sample container closed with an OL piston successfully works as a barrier for hydrous S-rich fluids. Due to Fe/Mg exchange reactions between OL container/piston and the melt, the MgO concentration of the product melts were strongly dependent on temperature increasing almost linear from \sim 5.5 wt.% MgO at 1050°C to \sim 13.5 wt.% MgO at 1250°C. This allowed us to constrain the sulfur solubility of natural OL-saturated melts undergoing processes of magmatic cooling.

We determined the sulfur concentration at anhydrite-saturation (FMQ+1.4 to FMQ +2.2) to be about 2.5 to 6-times higher than the S content at FeS-saturation (FMQ to FMQ+0.3). The sulfur content increases almost linear with temperature from 0.12 ± 0.01 to 0.39 ± 0.02 wt.% S at FeS-saturation and from 0.74 ± 0.01 to 1.08 ± 0.04 wt.% S at anhydrite-saturation, if T increases from 1050-1250°C. Both, our data for the S-concentration (at comparable temperature) and the observed T dependence on S solubility at FeS-saturation is about 2 to 3-times higher than data of former studies (Jugo et al., 2005a; Liu et al., 2007), which can be explained by the \sim 2 log units higher fO_2 and the 2.5 to 5-times lower P for our experiments.

The most recent model concerning the sulfate content at anhydrite-saturation in silicic melt (Li & Ripley, 2009) could not be satisfactorily applied to our data, because of the scarcity of sulfate-solubility data for basaltic melts at geologic relevant P-, T-, redox conditions and melt water contents.

Since the solubility of S is also a function of redox conditions, the variation in fO_2 for about 0.5 log units around FMQ+1 will change S solubility depending on the direction of the fO_2 change, where the increase in S solubility is higher by changing fO_2 from FMQ+1 to more oxidizing conditions, which can be explained by the increase of sulfate species and their high contribution to the total S solubility (Jugo et al., 2009, *subm.*)

We estimated the sulfur solubility as a function of MgO content in the melt at three different redox conditions at $fO_2 \sim$ FMQ+0.3 (reducing conditions), \sim FMQ+1 (moderate oxidizing conditions) and \sim FMQ+1.5 to FMQ+2 (oxidized conditions). This allowed us to constrain the temperature, the sulfur solubility and the fO_2 (if the S content in the melt is known) of natural melts in the OL-bearing magmatic systems. Thus, we determined the magmatic temperature and the sulfur solubility of the moderate oxidized (FMQ+1) OL-bearing melts of Mt.Etna, yielding T \sim 1025-1125°C and respectively \sim 0.25-0.4 wt.% S for juvenile S-rich melts and T lower \sim 1025°C and $\leq \sim$ 0.1 wt.% S for the more evolved S-depleted melts. The S content of the juvenile S-rich melts, representing lower T (up to 0.35 wt.% S at \sim 1025-1050°C) and the S-content of the more evolved S-depleted melts ($\leq \sim$ 0.2 wt.% S) is slightly higher than our estimated values for sulfur-saturation. Hence, we assume the magmatic system of Mt.Etna reflects slightly higher fO_2 than FMQ+1, except for strongly S-depleted FeS-bearing melts, which presumably reflect lower fO_2 than FMQ+1.

Chapter II: Sulphur and chlorine partitioning between aqueous fluid and silicate melt at 1050°C

1. Introduction

Numerous experimental studies concerning the solubility and partitioning of mixed volatiles between hydrous fluid and silicate melt have been limited to binary volatile systems such as S-H₂O (e.g., Carroll & Rutherford, 1985, 1987; Luhr et al., 1990; Clemente et al., 2004; Parat et al., 2005, 2008; Scaillet & McDonald, 2006; Keppler, 2010) and Cl-H₂O (e.g., Métrich & Rutherford, 1992; Webster, 1992; Kravchuk & Keppler, 1994; Webster et al. 1999; Signorelli & Carroll, 2000, 2001, 2002, Webster et al., 2001; Stelling et al., 2008). The effect of pressure and temperature on the chlorine solubility and on the chlorine partitioning between aqueous fluid and silicate melt is difficult to constrain, because the melt components (e.g., alkalis) tend to partition into an aqueous fluid in a larger extent, if the chlorine concentration increases (e.g., Candela & Piccoli, 1995; Williams et al., 1995, 1997; Student and Bodnar, 1999; Stelling et al., 2008). Thus, the fluid complexity increases with increasing chlorine concentration in the melt. The liquid-vapor relations in the system metal chloride-H₂O at elevated pressure and temperature were investigated by numerous studies e.g., Bischoff & Rosenbauer (1985, 1988), Bodnar et al. (1985), Bischoff & Pitzer (1989) and Driesner et al. (2007a, 2007b) for NaCl-H₂O, Bischoff et al., (1996) for CaCl₂-H₂O, Duan et al., (2006) for CaCl₂-MgCl₂-H₂O, Gunter et al. (1983), Chou (1987), Chou et al. (1992) and Sterner et al. (1992) for NaCl-KCl-H₂O. All of these studies have shown that fluid-unmixing occurs at certain temperature, pressure and fluid composition and the critical pressure is shifted to higher values, if the complexity of the fluid composition increases (e.g., Gunter et al., 1983, Chou, 1987, Chou et al., 1992; Sterner et al., 1992; Duan et al., 2006). The field of fluid immiscibility is characterized by the coexistence of a low dense H₂O-rich Cl

vapour phase and high dense Cl-rich brine, where the Cl activity at subcritical conditions remains constant. The strong dependence of fluid properties due to P, T and fluid composition results in a strong P- and T-dependence of the partitioning-behavior of chlorine between Cl-H₂O fluid and (natural multicomponent) silicate melt.

Recent experimental studies on multiple Cl-bearing systems have been limited to Cl-C-O-H-silicate melt (e.g., Botcharnikov et al., 2007; Alletti et al., 2009), Cl-F-O-H-silicate melt (e.g., Mathez & Webster, 2005; Chevichelov et al., 2008a, 2008b; Webster et al., 2009a). Studies concerning S- and Cl-bearing systems have been limited to H-C-O-S-silicate melt (Nicholis & Rutherford, 2006) or Cl-S-O-H-silicate melt (Botcharnikov et al., 2004; Webster et al., 2009b). Botcharnikov et al. (2004) and Webster et al. (2009b) observed a significant decrease in Cl melt concentrations by adding S to the system for rhyolitic and phonolitic to trachytic melt composition. To the best of our knowledge, no experimental study concerning S and Cl partitioning between hydrous fluid and basaltic melt is published so far. Although this is of major interest for interpretation and prediction of magmatic degassing for example at Mt.Etna (e.g., Métrich et al., 1993, 2004; Aiuppa et al., 2002, 2004, 2008; Spilliaert et al., 2006a, 2006b) and other volcanic systems (e.g., Devine et al., 1984; Symonds, 1994; Francis et al., 1995; Self & King 1996; Thordarson et al. 1996; Edmonds et al. 2001, 2002; De Hoog et al. 2001; Webster et al., 2001; Oppenheimer, 2003, 2006).

2. Experimental techniques

2.1 Starting glass

The chemical composition of the basaltic starting material is listed in Chapter I, Table 1. The composition of the dacitic starting glass (Table 6) corresponds to a natural sample (sample

KRA-076) of Krakatau volcano (1883 eruption) given by Mandeville et al. (1996) assigned as andesite.

Table 6: Chemical composition of the synthetic dacitic starting glass, corresponding to the natural sample no. KRA-076 of Krakatau volcano (1883 eruption) given by Mandeville et al. (1996) (in wt.%), n = 20:

SiO ₂	TiO ₂	Al ₂ O ₃	FeO _{tot}	MnO	MgO	CaO	Na ₂ O	K ₂ O	P ₂ O ₅	Total	A/CNK
65.28 (44)	0.94 (05)	16.51 (19)	5.49 (32)	0.15 (12)	1.48 (08)	4.48 (20)	4.27 (23)	1.97 (10)	0.38 (01)	100.95 (62)	0.97

Notes: n is the number of analyses. Number in parenthesis is 1 σ standard deviation of the mean. FeO_{tot} is the total iron content. A/CNK is the molar ratio of Al₂O₃ / (CaO + Na₂O + K₂O).

2.2 Sample preparation

The preparation of the Etna basalt starting glass is described in Chapter I (§ 2.2). The dacitic starting glass of Krakatau was synthesized by fusing a mixture of SiO₂, TiO₂, Al₂O₃, Fe₂O₃, Mn₃O₄, MgO, CaCO₃, Na₂CO₃, K₂CO₃ and (NH₄)H₂PO₄ at 1600 °C for 3 h in an 1 atm furnace. The obtained melt was subsequently quenched in a water bath, ground, remelted for 1 h, ground again and sieved to a grain size < 200 μ m.

2.3 Experimental methods

All experiments were performed under fluid saturated conditions with an initial total fluid concentration (bulk concentration) of ~ 11-13 wt.% for 200 MPa experiments and ~ 9-11 wt.% for 100 MPa experiments, providing mainly constant amounts of dissolved fluid in all experimental runs (the bulk concentration considers the total charge mass of sample powder and fluid). Au-capsules (length of 15 mm, inner/outer diameter 2.8/3.2 mm) were loaded with ~ 40-50 mg of sample powder, various amounts of elemental sulfur, ranging from 0-0.95 mg S (0-2 wt. % bulk S) and ~ 5-6 mg H₂O or HCl (aq) solution for 200 MPa experiments and ~ 4-5 mg HCl (aq) for 100 MPa experiments. Cl concentration of aqueous HCl-solutions ranged between 1.05-29.4 wt. % Cl and were determined using a Mettler DL25 Titrator. Hence, the loaded

amounts of bulk Cl were 0.05-3.5 wt.%, respectively. The loaded mass of S and Cl were chosen by obtaining bulk S and Cl concentrations of ~0.2, 0.5, 1.0 and 1.7-1.9 wt.% bulk S and ~0.06, 0.18, 0.6, 1.8 and 3.5 wt.% bulk Cl in 200 MPa experiments and with respect to less HCl charge for 100 MPa experiments ~0.05, 0.15, 0.55, 1.4 and 3.0 wt.% bulk Cl, respectively (already 0.06 wt.% Cl in the starting glass, Table 1). The capsules were closed by electric arc welding (under cooling with water). To ensure leak tightness and homogeneous fluid distribution, the capsules were heated for > 6 h at ~ 110 °C in an oven. Starting mass relations are shown in Table 7.

Four to five capsules were run simultaneously in an IHPV at T=1050°C and pressure of 200 MPa and 100 MPa, being relevant for magmatic storage conditions of volatile-rich juvenile melt and for slightly more evolved S-depleted melts of Mt.Etna, respectively (e.g., Métrich et al., 2004, Spilliaert et al., 2006a, 2006b). The oxidation state of Mt.Etna magma was determined to be relatively oxidized at ~FMQ+1 (Métrich & Clochiatti, 1989, 1996) or between ~FMQ+1 to ~FMQ+2 (as determined in Chapter I). Thus, the oxygen fugacity in our experiments was chosen to be oxidizing (~FMQ+1 and ~FMQ+4.2) and relatively reducing (~FMQ). Where FMQ+4.2 (at water saturation) is the intrinsic fO_2 imposed by the vessel (Berndt et al., 2002). An oxygen fugacity of FMQ and FMQ+1 was adjusted by adding H₂ to the Ar gas. This allowed us to determine the expected effect of fO_2 on S/Cl partitioning, caused by the strong influence of fO_2 within sulfide-sulfate transition on sulfur solubility (as discussed in Chapter I).

Table 7: Starting mass relations of experimental runs

Run #	m	m	m	c Cl	m	m	m	m	bulk	bulk	bulk	bulk	fluid		
	glass	S	HCl	HCl	H ₂ O	Cl _{added}	Cl _{init.}	Cl _{tot}	S	Cl	H ₂ O	fluid	X S	X Cl	X H ₂ O
	[mg]	[mg]	[mg]	[wt.%]	[mg]	[mg]	[mg]	[mg]	[wt.%]	[wt.%]	[wt.%]	[wt.%]	molar	molar	molar
200 MPa Etna basalt															
0_02_2	40.07	0.08	-	-	5.03	-	0.02	0.02	0.18	0.05	11.13	11.36	0.01	<0.01	0.99
0_05_2	39.87	0.20	-	-	5.04	-	0.02	0.02	0.44	0.05	11.17	11.66	0.02	<0.01	0.98
0_10_2	41.03	0.44	-	-	4.88	-	0.02	0.02	0.95	0.05	10.53	11.52	0.05	<0.01	0.95
0_15_2	40.90	0.85	-	-	5.27	-	0.02	0.02	1.81	0.05	11.21	13.06	0.08	<0.01	0.92
01_02_2	40.75	0.08	5.07	1.05	5.02	0.05	0.02	0.08	0.17	0.17	10.93	11.27	0.01	0.01	0.99
01_05_2	41.24	0.21	4.82	1.05	4.77	0.05	0.02	0.08	0.45	0.16	10.31	10.92	0.02	0.01	0.97
01_10_2	40.87	0.46	4.97	1.05	4.92	0.05	0.02	0.08	0.99	0.17	10.62	11.77	0.05	0.01	0.95
01_15_2	39.10	0.87	4.80	1.05	4.75	0.05	0.02	0.07	1.94	0.16	10.61	12.71	0.09	0.01	0.90
05_02_2	41.21	0.08	4.79	5.09	4.55	0.24	0.02	0.27	0.17	0.58	9.87	10.62	0.01	0.03	0.96
05_05_2	40.06	0.22	5.31	5.09	5.04	0.27	0.02	0.29	0.48	0.65	11.05	12.18	0.02	0.03	0.95
05_10_2	41.93	0.44	5.07	5.09	4.81	0.26	0.03	0.28	0.93	0.60	10.14	11.66	0.05	0.03	0.93
05_15_2	41.51	0.88	5.25	5.09	4.98	0.27	0.02	0.29	1.85	0.61	10.46	12.91	0.09	0.03	0.89
15_02_2	40.55	0.08	5.47	14.37	4.68	0.79	0.02	0.81	0.17	1.76	10.16	12.09	0.01	0.08	0.91
15_05_2	40.74	0.24	5.51	14.37	4.72	0.79	0.02	0.82	0.52	1.75	10.15	12.41	0.03	0.08	0.90
15_10_2	40.22	0.44	5.50	14.37	4.71	0.79	0.02	0.81	0.95	1.76	10.20	12.91	0.05	0.08	0.88
15_15_2	40.05	0.86	5.46	14.37	4.68	0.78	0.02	0.81	1.85	1.74	10.08	13.67	0.09	0.08	0.84
30_02_2	43.38	0.08	5.55	29.42	3.92	1.63	0.03	1.66	0.16	3.38	7.99	11.53	0.01	0.18	0.81
30_05_2	45.53	0.21	5.76	29.42	4.07	1.69	0.03	1.72	0.41	3.34	7.89	11.64	0.02	0.18	0.80
30_10_2	42.31	0.43	5.82	29.42	4.11	1.71	0.03	1.74	0.89	3.58	8.46	12.92	0.05	0.17	0.78
30_15_2	44.79	0.95	5.81	29.42	4.10	1.71	0.03	1.74	1.84	3.37	7.95	13.16	0.10	0.16	0.74
0_15_2 ox	43.65	0.94	-	-	5.19	-	0.03	0.03	1.89	0.05	10.43	12.36	0.09	<0.01	0.91
01_15_2 ox	47.62	0.86	5.44	1.05	5.38	0.06	0.03	0.09	1.59	0.16	9.98	11.73	0.08	0.01	0.91
05_15_2ox	41.81	0.89	5.38	5.09	5.11	0.27	0.03	0.30	1.85	0.62	10.62	13.09	0.09	0.03	0.89
15_15_2ox	46.03	0.93	5.43	14.37	4.65	0.78	0.03	0.81	1.77	1.54	8.88	12.19	0.09	0.08	0.83
30_15_2 ox	46.45	0.92	6.02	29.42	4.25	1.77	0.03	1.80	1.72	3.37	7.96	13.04	0.09	0.16	0.75
0_15_2 red	46.71	0.97	-	-	6.11	-	0.03	0.03	1.80	0.05	11.36	13.21	0.08	<0.01	0.92
01_15_2 red	39.89	0.83	5.00	1.05	4.95	0.05	0.02	0.08	1.81	0.17	10.82	12.80	0.09	0.01	0.91
05_15_2 red	42.16	0.88	5.20	5.09	4.94	0.26	0.03	0.29	1.82	0.60	10.23	12.65	0.09	0.03	0.89
15_15_2 red	43.07	0.94	5.56	14.37	4.76	0.80	0.03	0.82	1.90	1.66	9.60	13.16	0.09	0.08	0.83
30_15_2 red	40.85	0.83	5.50	29.42	3.88	1.62	0.02	1.64	1.76	3.48	8.23	13.46	0.09	0.16	0.75
100 MPa Etna basalt															
0_02_1	41.37	0.09	-	-	4.26	-	0.02	0.02	0.20	0.05	9.32	9.56	0.01	<0.01	0.99
0_05_1	42.47	0.20	-	-	4.53	-	0.03	0.03	0.42	0.05	9.60	10.07	0.02	<0.01	0.98
0_10_1	51.15	0.51	-	-	5.20	-	0.03	0.03	0.90	0.05	9.15	10.09	0.05	<0.01	0.95
0_15_1	37.47	0.77	-	-	3.88	-	0.02	0.02	1.83	0.05	9.21	11.09	0.10	<0.01	0.90
01_02_1	40.16	0.07	3.93	1.05	3.89	0.04	0.02	0.07	0.16	0.15	8.81	9.11	0.01	0.01	0.98
01_05_1	41.30	0.24	3.95	1.05	3.91	0.04	0.02	0.07	0.53	0.15	8.59	9.26	0.03	0.01	0.96
01_10_1	41.29	0.42	4.18	1.05	4.14	0.04	0.02	0.07	0.91	0.15	9.01	10.07	0.05	0.01	0.94
01_15_1	41.24	0.84	4.14	1.05	4.10	0.04	0.02	0.07	1.82	0.15	8.86	10.82	0.10	0.01	0.89

Table 7: Continued

Run #	m glass [mg]	m S [mg]	m HCl [mg]	c Cl HCl [wt.%]	m H ₂ O [mg]	m Cl _{added} [mg]	m Cl _{init.} [mg]	m Cl _{tot} [mg]	bulk S [wt.%]	bulk Cl [wt.%]	bulk H ₂ O [wt.%]	bulk fluid [wt.%]	X S molar	X Cl molar	X H ₂ O molar
05_02_1	41.87	0.08	4.50	5.09	4.27	0.23	0.03	0.25	0.17	0.55	9.19	9.91	0.01	0.03	0.96
05_05_1	41.49	0.20	4.35	5.09	4.13	0.22	0.02	0.25	0.43	0.53	8.97	9.93	0.03	0.03	0.95
05_10_1	40.53	0.42	4.19	5.09	3.98	0.21	0.02	0.24	0.93	0.53	8.81	10.26	0.05	0.03	0.92
05_15_1	41.59	0.86	4.58	5.09	4.35	0.23	0.02	0.26	1.83	0.55	9.24	11.61	0.10	0.03	0.88
15_02_1	41.99	0.08	4.48	14.37	3.84	0.64	0.03	0.67	0.17	1.44	8.24	9.84	0.01	0.08	0.91
15_05_1	44.69	0.22	4.63	14.37	3.96	0.67	0.03	0.69	0.44	1.40	8.00	9.84	0.03	0.08	0.89
15_10_1	40.91	0.39	4.37	14.37	3.74	0.63	0.02	0.65	0.85	1.43	8.19	10.47	0.05	0.08	0.87
15_15_1	40.56	0.79	4.30	14.37	3.68	0.62	0.02	0.64	1.73	1.41	8.07	11.20	0.10	0.08	0.83
30_02_1	52.63	0.11	5.58	29.42	3.94	1.64	0.03	1.67	0.19	2.87	6.75	9.81	0.01	0.18	0.81
30_05_1	40.18	0.19	4.74	29.42	3.35	1.39	0.02	1.42	0.42	3.14	7.42	10.98	0.03	0.18	0.80
30_10_1	41.11	0.39	4.69	29.42	3.31	1.38	0.02	1.40	0.84	3.04	7.17	11.05	0.05	0.17	0.78
30_15_1	37.88	0.77	4.39	29.42	3.10	1.29	0.02	1.31	1.79	3.05	7.20	12.04	0.10	0.16	0.74
0_15_1 ox	42.24	0.81	-	-	4.29	-	0.03	0.03	1.71	0.05	9.06	10.82	0.10	<0.01	0.90
01_15_1 ox	38.44	0.88	3.86	1.05	3.82	0.04	0.02	0.06	2.04	0.15	8.85	11.02	0.11	0.01	0.88
05_15_1 ox	41.50	0.84	3.87	5.09	3.67	0.20	0.02	0.22	1.82	0.48	7.95	10.24	0.11	0.03	0.86
15_15_1 ox	43.99	0.88	4.44	14.37	3.80	0.64	0.03	0.66	1.78	1.35	7.71	10.84	0.11	0.07	0.82
30_15_1 ox	48.09	0.93	4.92	29.42	3.47	1.45	0.03	1.48	1.72	2.74	6.44	10.89	0.11	0.16	0.73
200 MPa	Etna basalt														
0-1050	56.67	-	-	-	5.99	-	0.03	0.03	-	0.05	9.56	9.61	-	<0.01	1.00
1-1050	52.78	-	5.86	5.09	5.56	0.30	0.03	0.33	-	0.56	9.48	9.99	-	0.03	0.97
2-1050	55.56	-	5.63	9.77	5.08	0.55	0.03	0.58	-	0.95	8.30	9.20	-	0.05	0.95
3-1050	51.49	-	6.25	20.43	4.97	1.28	0.03	1.30	-	2.26	8.61	10.82	-	0.12	0.88
4-1050	53.19	-	6.50	29.42	4.59	1.91	0.03	1.94	-	3.25	7.69	10.89	-	0.18	0.82
200 MPa	Krakatau dacite														
KRA 0_0	53.60	-	-	-	9.75	-	-	-	-	-	15.39	15.39	-	-	1.00
KRA 05_0	56.81	-	5.84	5.09	5.54	0.30	-	0.30	-	0.47	8.85	9.32	-	0.03	0.97
KRA 10_0	57.27	-	6.50	9.77	5.87	0.63	-	0.63	-	1.00	9.20	10.19	-	0.05	0.95
KRA 20_0	54.48	-	6.39	20.43	5.08	1.31	-	1.31	-	2.14	8.35	10.50	-	0.12	0.88
KRA 30_0	54.01	-	6.89	29.42	4.86	2.03	-	2.03	-	3.33	7.98	11.31	-	0.17	0.83
KRA 0_0	49.24	-	-	-	5.40	-	-	9.88	-	-	9.88	9.88	-	-	1.00
KRA 0_2	50.24	0.10	-	-	5.37	-	-	9.82	0.18	-	9.64	9.82	0.01	-	0.99
KRA 0_5	50.44	0.30	-	-	5.24	-	-	9.90	0.54	-	9.36	9.90	0.03	-	0.97
KRA 0_10	50.62	0.56	-	-	5.10	-	-	10.06	1.00	-	9.06	10.06	0.06	-	0.94
KRA 0_15	52.46	0.80	-	-	4.97	-	-	9.91	1.37	-	8.54	9.91	0.08	-	0.92

Notes: m is the mass. c Cl is the concentration of Cl in HCl in wt.%; m Cl_{added} is the mass of Cl contained the added mass of HCl solution; m Cl_{init.} is the mass of Cl in the starting material due to the initial Cl concentration of 0.06 wt.% Cl in the starting glass; m Cl_{tot} is the sum of m Cl_{added} and m Cl_{init.}. Bulk S, Cl and H₂O is the concentration of S, Cl and H₂O in wt.%, respectively, with respect to the total loaded starting mass. Bulk fluid is the total sum of bulk S, Cl and H₂O in wt.%. X S, X Cl and X H₂O is the molar ratio of S, Cl and H₂O, respectively in the bulk fluid (defined to be solely composed of the volatile components S and/or Cl and H₂O added to the system).

PH₂ at experiments using an Ar-H₂ mixture was monitored by the shaw-membrane technique. Run durations were 24 to 72 h. All experiments were stopped by quenching the samples rapidly using the rapid quench-technique as described by Berndt et al. (2002). The sample capsules were subsequently weighed and thus checked for leaks as indicated by significant weight loss. Only those runs were assigned to be successful, where the loss of weight was below 0.05 mg. The experimental run conditions are assigned in Table 8.

In addition six Cl partitioning experiments were performed in Au₈₀Pd₂₀ capsules at 200 MPa, 1200°C and ~FMQ+1 using the Etna basaltic starting material and pure AgCl or AgCl-H₂O/HCl mixture as Cl source. The experimental procedure was similar to that of the PtCl₄-charged experiments given by Stelling et al. (2008). Since our study focuses on ternary Cl-S-H₂O-fluid systems, these experiments will be not described in detail. However, in the following these data are shown, because they provide useful information about the partitioning-behavior of chlorine. The starting mass relations, the chemical composition of product glasses and the composition of product fluids for the AgCl- or AgCl-H₂O/HCl-charged experiments (in the following assigned as AgCl-data) are listed in the Appendix at Table D, E and F.

Table 8: Experimental run conditions, chemical composition of experimental product glasses (in wt.%), listing of mineral- and S-bearing phases and phase content (in vol.%)

Run #	S^{2+} [bar]	\log [bar]	Δ [bar]	n	SiO ₂	TiO ₂	Al ₂ O ₃	FeO _{tot}	MnO	MgO	CaO	Na ₂ O	K ₂ O	P ₂ O ₅	Cl	S	Total	H ₂ O KFT	H ₂ O FTIR	Phase cont. [vol.%]	AI CNK	Phases
<i>P=201 MPa, PH₂=1.4 bar, log FO₂=-7.7/FMQ+2.3, 45 h</i>																						
0_02_2	15	46.53 (39)	1.64 (04)	15.85 (23)	8.27 (41)	0.17 (02)	5.87 (20)	10.32 (30)	3.33 (22)	1.84 (07)	0.51 (05)	0.056 (000)	0.150 (000)	94.53 (75)	5.23 (06)	6.50 (03)	1	0.60	Spl			
0_05_2	15	46.21 (39)	1.61 (06)	15.61 (20)	8.36 (41)	0.17 (03)	5.71 (15)	10.23 (23)	3.31 (21)	1.85 (10)	0.54 (04)	0.055 (000)	0.442 (001)	94.09 (81)	5.23 (06)	6.63 (06)	1	0.60	Spl*			
0_10_2	15	45.95 (38)	1.62 (05)	15.54 (17)	8.32 (40)	0.17 (03)	5.68 (10)	10.08 (22)	3.29 (21)	1.82 (09)	0.55 (04)	0.055 (000)	0.704 (001)	93.77 (65)	5.16 (11)	6.27 (04)	1	0.60	Spl*			
0_15_2	15	46.20 (41)	1.62 (07)	15.66 (18)	8.32 (39)	0.18 (03)	5.76 (15)	9.52 (19)	3.10 (18)	1.89 (07)	0.48 (04)	0.047 (000)	0.853 (002)	93.44 (70)	5.13 (10)	6.95 (04)	2	0.65	Spl, Anh			
<i>P=201 MPa, PH₂=1.9 bar, log FO₂=-8.8/FMQ+2.1, 46 h</i>																						
01_02_2	2.0	46.13 (34)	1.65 (04)	15.72 (15)	8.88 (31)	0.18 (04)	5.75 (09)	10.34 (22)	3.44 (20)	1.86 (08)	0.52 (05)	0.170 (000)	0.171 (000)	94.82 (59)	5.19 (14)	n.d.	2	0.59	Spl*			
01_05_2	2.2	46.04 (37)	1.62 (06)	15.58 (21)	8.72 (31)	0.17 (02)	5.77 (15)	10.26 (17)	3.39 (16)	1.82 (05)	0.49 (06)	0.167 (000)	0.424 (001)	94.47 (78)	5.27 (17)	6.95 (04)	2	0.59	Spl*			
01_10_2	2.3	45.42 (49)	1.60 (03)	15.35 (25)	8.66 (32)	0.17 (03)	5.78 (16)	10.06 (20)	3.29 (26)	1.80 (06)	0.50 (04)	0.164 (000)	0.733 (002)	93.53 (64)	5.20 (17)	6.87 (02)	1	0.60	Spl*			
01_15_2	2.4	46.14 (18)	1.58 (05)	15.65 (23)	8.64 (36)	0.18 (03)	5.71 (14)	9.39 (25)	3.09 (22)	1.72 (09)	0.50 (05)	0.145 (000)	0.824 (001)	93.57 (60)	4.79 (12)	6.93 (03)	1	0.65	Spl*, Anh			
<i>P=199 MPa, PH₂=1.3 bar, log FO₂=-7.7/FMQ+2.4, 50 h</i>																						
05_02_2	1.7	45.74 (26)	1.66 (06)	15.56 (26)	8.93 (38)	0.18 (02)	5.71 (14)	10.15 (27)	3.33 (19)	1.82 (08)	0.51 (03)	0.566 (001)	0.105 (000)	94.25 (79)	5.07 (12)	n.d.	1	0.60	Spl			
05_05_2	1.6	45.25 (34)	1.67 (07)	15.57 (21)	9.14 (38)	0.19 (02)	5.79 (13)	10.12 (29)	3.28 (15)	1.79 (08)	0.51 (04)	0.567 (001)	0.392 (001)	94.28 (66)	5.24 (09)	7.15 (05)	0	0.61	-			
05_10_2	1.6	44.63 (39)	1.63 (03)	15.15 (19)	8.92 (49)	0.17 (03)	5.60 (19)	9.93 (22)	3.16 (14)	1.80 (05)	0.50 (04)	0.583 (001)	0.614 (001)	92.69 (75)	5.33 (11)	n.d.	0	0.60	-			
05_15_2	1.7	45.36 (39)	1.63 (04)	15.42 (23)	8.64 (34)	0.16 (03)	5.53 (16)	9.30 (25)	3.09 (20)	1.71 (08)	0.53 (05)	0.532 (001)	0.829 (001)	92.74 (52)	4.98 (07)	n.d.	<1	0.65	Spl, Anh			
<i>P=206 MPa, PH₂=2.2 bar, log FO₂=-8.1/FMQ+1.9, 34 h</i>																						
15_02_2	2.2	44.93 (35)	1.62 (06)	15.29 (18)	9.64 (22)	0.18 (03)	5.82 (10)	10.05 (29)	3.17 (17)	1.70 (07)	0.49 (04)	1.511 (002)	0.205 (001)	94.61 (53)	5.60 (06)	6.98 (06)	0	0.60	-			
15_05_2	2.1	44.53 (32)	1.62 (06)	15.21 (19)	9.39 (40)	0.16 (02)	5.69 (13)	9.95 (20)	3.15 (13)	1.67 (09)	0.50 (04)	1.544 (003)	0.379 (001)	93.79 (46)	5.87 (07)	7.15 (02)	0	0.61	-			
15_10_2	2.0	44.25 (24)	1.66 (03)	15.06 (16)	9.56 (31)	0.17 (03)	5.64 (16)	9.85 (20)	3.16 (20)	1.70 (07)	0.50 (06)	1.528 (004)	0.709 (001)	93.78 (57)	5.53 (11)	7.52 (04)	0	0.60	-			
15_15_2	2.2	44.77 (31)	1.68 (06)	15.27 (26)	9.55 (45)	0.17 (03)	5.63 (16)	9.24 (15)	2.92 (20)	1.60 (09)	0.50 (03)	1.372 (001)	0.790 (001)	93.49 (56)	5.86 (07)	n.d.	<1	0.65	Anh			
<i>P=205 MPa, PH₂=1.6 bar, log FO₂=-7.8/FMQ+2.2, 48 h</i>																						
30_02_2	2.6	45.20 (26)	1.64 (05)	15.45 (17)	9.28 (43)	0.18 (03)	5.82 (19)	10.01 (17)	2.97 (25)	1.49 (06)	0.50 (06)	2.231 (003)	0.037 (000)	94.80 (45)	5.93 (10)	7.33 (05)	0	0.63	-			
30_05_2	2.2	44.38 (28)	1.63 (06)	15.27 (29)	9.28 (42)	0.16 (03)	5.72 (17)	9.84 (21)	3.01 (18)	1.54 (09)	0.50 (05)	2.266 (003)	0.286 (001)	93.88 (84)	5.70 (10)	7.46 (07)	0	0.62	-			
30_10_2	2.2	44.76 (32)	1.61 (08)	15.33 (14)	9.38 (25)	0.17 (02)	5.61 (15)	9.55 (16)	2.79 (09)	1.47 (07)	0.54 (05)	2.211 (006)	0.547 (001)	93.97 (41)	5.89 (16)	7.33 (05)	<1	0.65	Anh			
30_15_2	2.3	45.51 (30)	1.69 (06)	15.52 (18)	9.42 (36)	0.17 (03)	5.66 (14)	8.76 (26)	2.66 (20)	1.39 (08)	0.48 (04)	1.971 (004)	0.634 (003)	93.85 (69)	5.78 (13)	6.67 (04)	<1	0.71	Anh			
<i>P=200 MPa, intrinsic PH₂ log FO₂=-5.8/FMQ+4.2, 54 h</i>																						
0_15_2 ox	2.2	48.16 (38)	1.63 (04)	16.23 (21)	6.83 (42)	0.16 (02)	5.45 (17)	8.96 (20)	3.15 (17)	1.72 (12)	0.48 (06)	0.044 (000)	0.742 (001)	93.54 (80)	5.48 (08)	n.d.	4	0.70	Spl*, Anh ¹			
01_15_2 ox	15	47.67 (47)	1.64 (04)	16.10 (25)	6.97 (34)	0.18 (02)	5.49 (12)	9.28 (20)	3.20 (24)	1.71 (06)	0.47 (06)	0.135 (000)	0.765 (001)	93.61 (92)	5.45 (08)	n.d.	4	0.67	Spl*, Anh			
05_15_2 ox	15	47.47 (22)	1.62 (05)	15.92 (24)	7.15 (39)	0.16 (02)	5.49 (10)	9.09 (22)	2.95 (18)	1.67 (09)	0.47 (05)	0.495 (000)	0.724 (001)	93.22 (78)	5.49 (11)	n.d.	4	0.69	Spl*			
15_15_2 ox	1.9	47.59 (29)	1.63 (04)	15.88 (22)	7.46 (32)	0.16 (03)	5.46 (18)	8.68 (11)	2.82 (20)	1.60 (07)	0.47 (05)	1.018 (001)	0.655 (001)	93.43 (66)	5.28 (10)	n.d.	5	0.72	Spl*, Anh			
30_15_2 ox	1.7	47.24 (13)	1.64 (29)	15.96 (08)	7.94 (15)	0.16 (04)	5.44 (03)	8.39 (05)	2.65 (29)	1.42 (27)	0.45 (02)	1.750 (001)	0.580 (047)	93.62 (07)	5.24 (00)	n.d.	2	0.75	Spl*, Anh			

Table 8: Continued

Run #	S^{Tj}	ΣfO_2	$\log \frac{\Delta}{FMQ}$	n	SiO ₂	TiO ₂	Al ₂ O ₃	FeO _{tot}	MnO	MgO	CaO	Na ₂ O	K ₂ O	P ₂ O ₅	Cl	S	Total	H ₂ O KFT	H ₂ O FTIR	cryst. [vol.%]	A/ CNK	phases	
																							$\log fO_2$ [bar]
<i>P=193 MPa, PH₂=8.9 bar,</i>																							
<i>log fO₂=-9.3/FMQ+0.7, 54 h</i>																							
0_15_2	red	0.16	-9.7	0.3	15	46.68(38)	1.67(05)	16.05(26)	7.72(42)	0.17(02)	5.56(15)	10.31(27)	3.50(18)	1.84(07)	0.51(03)	0.055(000)	0.119(001)	94.17(78)	4.84(10)	5.89(05)	2	0.61	FeS*, Spl, OL*, Cpx*
01_15_2	red				15	47.33(41)	1.74(07)	16.69(25)	7.78(34)	0.18(03)	5.01(14)	10.36(42)	3.59(14)	1.92(11)	0.52(03)	0.172(000)	0.085(001)	95.38(56)	4.34(08)	4.55(19)	6	0.62	FeS*, Spl, OL*, Cpx*
05_15_2	red	0.21	-9.6	0.5	15	46.23(30)	1.69(05)	15.95(13)	8.05(42)	0.18(03)	5.51(19)	10.33(25)	3.39(18)	1.75(06)	0.50(02)	0.568(001)	0.130(001)	94.28(85)	4.78(12)	n.d.(00)	2	0.61	FeS*, Spl
15_15_2	red				15	46.00(35)	1.68(06)	15.64(18)	7.83(39)	0.16(03)	5.67(15)	10.27(26)	3.35(30)	1.75(08)	0.50(03)	1.443(002)	0.111(001)	94.40(53)	4.92(14)	5.90(12)	<1	0.60	FeS, Spl
30_15_2	red				15	45.41(46)	1.65(06)	15.45(19)	8.30(24)	0.19(03)	5.81(16)	10.32(23)	3.46(23)	1.68(08)	0.49(02)	2.235(002)	0.110(001)	95.09(87)	4.43(10)	n.d.(00)	<1	0.59	FeS*
<i>P=99 MPa, PH₂=0.45 bar,</i>																							
<i>log fO₂=-7.2/FMQ+2.9, 72 h</i>																							
0_02_1					15	47.57(42)	1.64(07)	17.63(23)	7.38(48)	0.18(02)	4.89(17)	9.67(23)	3.64(25)	2.05(07)	0.59(03)	0.058(000)	0.134(001)	95.43(79)	3.41(05)	4.64(03)	10	0.68	Cpx*, Spl*
0_05_1		0.89	-8.1	2.0	15	47.73(36)	1.62(05)	16.86(20)	7.65(38)	0.18(02)	5.23(10)	10.03(26)	3.54(16)	1.94(08)	0.52(02)	0.058(000)	0.317(001)	95.68(63)	3.57(11)	4.64(03)	6	0.64	Cpx*, Spl*, OL*
0_10_1					15	47.53(26)	1.61(03)	16.46(24)	7.81(27)	0.19(02)	5.35(15)	10.34(33)	3.35(22)	1.89(08)	0.50(03)	0.057(000)	0.498(003)	95.59(80)	3.48(09)	4.53(02)	4	0.62	Cpx, Spl*
0_15_1		0.87	-8.2	1.9	14	47.95(47)	1.66(05)	16.77(23)	7.82(44)	0.17(03)	5.36(13)	9.94(24)	3.09(22)	1.75(08)	0.52(03)	0.051(000)	0.496(001)	95.58(74)	2.72(08)	4.45(08)	3	0.67	Spl, Anh
<i>P=99 MPa, (PH₂=0.02 bar,</i>																							
<i>log fO₂=-4.5/FMQ+5.6)*, 72 h</i>																							
01_02_1					15	48.36(33)	1.65(04)	17.48(19)	7.48(36)	0.19(03)	5.08(10)	9.84(15)	3.64(17)	2.02(07)	0.57(03)	0.153(000)	0.158(000)	96.63(68)	3.37(05)	4.79(01)	6	0.67	Cpx*, Spl*, OL*
01_05_1					15	47.82(21)	1.66(05)	16.95(21)	7.56(49)	0.18(03)	5.19(16)	10.10(17)	3.54(24)	1.99(07)	0.53(03)	0.152(000)	0.303(001)	95.96(69)	3.95(05)	4.92(02)	10	0.64	Cpx*, Spl*, OL*
01_10_1		0.87	-8.2	1.9	15	47.43(28)	1.64(05)	16.38(19)	7.90(31)	0.18(03)	5.32(14)	10.38(27)	3.31(19)	1.80(07)	0.49(03)	0.137(002)	0.513(001)	95.48(49)	3.29(10)	4.89(04)	5	0.62	Spl*, OL*
01_15_1		0.89	-8.1	2.0	15	48.14(43)	1.63(05)	16.66(24)	8.01(39)	0.18(02)	5.49(16)	9.57(22)	3.19(16)	1.77(07)	0.47(02)	0.130(000)	0.596(001)	95.84(59)	3.36(03)	4.68(07)	2	0.68	Spl*, OL, Anh
<i>P=98 MPa, (PH₂=0.2 bar,</i>																							
<i>log fO₂=-6.5/FMQ+3.6)*, 46 h</i>																							
05_02_1					15	47.81(35)	1.63(07)	16.72(21)	7.07(36)	0.17(03)	5.25(20)	10.03(27)	3.74(21)	2.01(07)	0.56(02)	0.465(001)	0.460(002)	95.91(62)	3.61(08)	4.65(01)	2	0.63	Cpx*, Spl*
05_05_1					15	47.02(39)	1.65(04)	16.49(24)	7.33(26)	0.20(03)	5.40(19)	10.45(23)	3.45(18)	1.88(09)	0.54(02)	0.559(001)	0.506(003)	95.48(78)	3.39(09)	4.70(02)	5	0.62	Cpx*, Spl*, OL*
05_10_1		0.92	-8.0	2.1	15	47.49(51)	1.63(04)	16.53(20)	7.50(29)	0.18(02)	5.43(16)	10.11(21)	3.33(19)	1.78(06)	0.52(03)	0.434(001)	0.538(001)	95.46(88)	3.32(09)	4.60(02)	5	0.64	Spl
05_15_1		0.87	-8.2	1.9	15	49.04(39)	1.65(05)	16.76(30)	7.20(33)	0.19(03)	5.44(13)	9.38(20)	3.22(18)	1.70(05)	0.51(03)	0.395(001)	0.538(001)	96.02(44)	3.36(14)	4.28(02)	3	0.69	Spl*, Anh
<i>P=98 MPa, (PH₂=0.02 bar,</i>																							
<i>log fO₂=-4.5/FMQ+5.6)*, 46 h</i>																							
15_02_1					15	47.24(25)	1.57(08)	16.09(18)	7.84(30)	0.17(02)	5.54(15)	10.22(25)	3.42(19)	1.86(07)	0.50(02)	1.250(001)	0.052(000)	95.75(60)	3.67(13)	4.56(03)	8	0.61	Cpx*, Spl*
15_05_1		0.84	-8.3	1.8	15	46.52(49)	1.54(08)	15.60(37)	7.98(30)	0.16(03)	5.66(13)	10.27(17)	3.28(19)	1.78(06)	0.46(03)	1.255(003)	0.321(002)	94.81(95)	3.74(13)	4.78(04)	2	0.60	Spl*, OL*
15_10_1					15	47.19(48)	1.56(05)	15.79(28)	7.77(41)	0.17(02)	5.70(17)	9.87(27)	3.13(18)	1.64(06)	0.41(02)	1.043(004)	0.418(002)	94.69(72)	3.65(11)	4.63(02)	4	0.63	Spl, Anh
15_15_1		0.87	-8.2	1.9	15	48.68(28)	1.56(07)	16.38(19)	7.65(27)	0.17(03)	5.67(13)	8.91(25)	2.96(18)	1.56(08)	0.38(03)	0.798(006)	0.413(001)	95.13(47)	3.69(12)	4.49(03)	1	0.72	Spl*, Anh
<i>P=102 MPa, PH₂=0.5 bar,</i>																							
<i>log fO₂=-7.3/FMQ+2.8, 68 h</i>																							
30_02_1					15	45.39(39)	1.57(07)	15.54(18)	9.38(32)	0.18(03)	5.72(10)	10.05(21)	3.31(19)	1.67(05)	0.42(02)	2.198(004)	0.050(000)	95.47(64)	3.94(04)	4.93(04)	1	0.61	Spl*
30_05_1		0.92	-7.9	2.1	15	45.53(42)	1.54(05)	15.60(29)	9.38(37)	0.17(03)	5.77(18)	9.93(21)	3.13(28)	1.62(07)	0.44(02)	2.145(010)	0.203(001)	95.46(100)	3.98(03)	n.d.(00)	3	0.63	Spl*
30_10_1					15	45.24(42)	1.56(08)	15.57(25)	9.40(38)	0.17(02)	5.69(16)	9.79(16)	3.04(19)	1.57(07)	0.44(02)	1.993(004)	0.333(001)	94.80(83)	3.90(05)	4.86(06)	2	0.64	Spl, Anh
30_15_1		0.95	-7.8	2.3	15	46.31(42)	1.64(08)	16.00(21)	9.22(35)	0.17(03)	5.64(18)	8.76(24)	2.76(17)	1.42(08)	0.43(02)	1.621(004)	0.433(001)	94.41(66)	3.59(05)	5.10(03)	2	0.73	Spl*, Anh

Table 8: Continued

Run #	$S^{57}/\Sigma S$	$\log \Delta$	$\log fO_2$	$\log fO_2$	n	SiO ₂	TiO ₂	Al ₂ O ₃	FeO _{tot}	MnO	MgO	CaO	Na ₂ O	K ₂ O	P ₂ O ₅	Cl	S	Total	H ₂ O	H ₂ O	H ₂ O	FTIR	cryst. CNK	AI	phases		
		[bar]																		KFT		[vol.%]					
<i>P=100 MPa, intrinsic PH₂</i>																											
<i>log fO₂=-5.9/FMQ+4.2 48 h</i>																											
0_15_1 ox			15	47.52 (37)	1.60 (05)	16.28 (26)	7.79 (32)	0.18 (02)	5.76 (16)	9.74 (23)	3.18 (22)	1.72 (06)	0.46 (02)	0.045 (000)	0.644 (001)	94.92 (75)	3.81 (08)	4.53 (05)	2	0.66						Spl ¹ , OL ¹ , Anh	
01_15_1 ox	0.95	-7.8	2.3	48.41 (48)	1.60 (08)	16.43 (27)	7.67 (32)	0.17 (03)	5.51 (17)	8.74 (23)	3.28 (26)	1.70 (08)	0.50 (03)	0.119 (001)	0.592 (001)	94.73 (75)	4.01 (08)	4.32 (01)	10	0.71						Spl ¹ , Anh ¹	
05_15_1 ox			15	46.74 (32)	1.57 (06)	16.17 (25)	8.21 (32)	0.18 (02)	5.71 (14)	9.21 (22)	3.12 (23)	1.60 (11)	0.48 (03)	0.361 (001)	0.606 (003)	93.95 (69)	3.95 (08)	4.64 (02)	1	0.68						Spl ¹ , Anh	
15_15_1 ox			14	47.11 (35)	1.63 (02)	16.24 (15)	8.04 (36)	0.18 (03)	5.60 (17)	8.86 (12)	3.00 (19)	1.59 (09)	0.47 (03)	0.861 (001)	0.529 (006)	94.10 (89)	3.70 (11)	4.51 (02)	1	0.71						Spl ¹ , Anh	
30_15_1 ox	0.92	-8.0	2.1	47.11 (46)	1.65 (08)	16.32 (19)	9.09 (43)	0.17 (03)	5.69 (12)	8.77 (16)	2.76 (18)	1.46 (08)	0.47 (03)	1.333 (003)	0.436 (004)	95.24 (80)	3.55 (07)	4.40 (01)	2	0.74						Spl ¹ , Anh	
<i>P=203 MPa, PH₂=7.5 bar,</i>																											
<i>log fO₂=-9.2/FMQ+0.9, 24 h</i>																											
0-1050			15	45.67 (22)	1.58 (05)	15.52 (21)	9.75 (25)	0.14 (12)	5.29 (14)	10.16 (33)	3.10 (21)	1.85 (08)	n.d.	0.056 (000)	n.d.	93.12 (72)	5.16 (09)	n.d.	1	0.61						Spl	
1-1050			15	45.55 (37)	1.58 (05)	15.45 (27)	9.73 (57)	0.13 (11)	5.46 (20)	9.96 (38)	3.20 (23)	1.83 (06)	n.d.	0.000 (000)	n.d.	93.43 (109)	5.23 (12)	n.d.	1	0.61						Spl	
2-1050			15	45.43 (30)	1.59 (04)	15.41 (22)	9.56 (45)	0.17 (11)	5.48 (14)	10.01 (18)	3.14 (24)	1.78 (08)	n.d.	0.791 (001)	n.d.	93.34 (60)	5.16 (15)	n.d.	<1	0.61						Spl	
3-1050			15	45.05 (44)	1.55 (06)	15.28 (21)	9.40 (26)	0.17 (12)	5.37 (13)	9.91 (27)	3.11 (24)	1.78 (08)	n.d.	0.000 (000)	n.d.	93.55 (76)	5.49 (13)	n.d.	0	0.61						-	
4-1050			15	45.33 (48)	1.54 (06)	15.10 (18)	9.26 (37)	0.19 (10)	5.42 (16)	9.91 (26)	2.93 (19)	1.60 (05)	n.d.	0.260 (002)	n.d.	93.53 (52)	5.55 (11)	n.d.	0	0.61						-	
<i>P=202 MPa, PH₂=8.6 bar,</i>																											
<i>log fO₂=-9.3/FMQ+0.7, 46 h</i>																											
KRA 0_0			30	61.20 (48)	0.89 (05)	15.62 (29)	5.17 (33)	0.16 (03)	1.37 (07)	4.35 (22)	3.84 (23)	1.86 (10)	0.36 (03)	0.001 (000)	n.d.	94.81 (79)	5.73 (14)	n.d.	<1	0.96						Spl	
KRA 05_0			10	61.11 (46)	0.89 (05)	15.56 (21)	5.03 (29)	0.16 (03)	1.38 (06)	4.25 (19)	3.77 (37)	1.86 (10)	0.37 (03)	0.398 (000)	n.d.	94.76 (73)	5.75 (09)	n.d.	<1	0.98						Spl	
KRA 10_0			30	60.78 (45)	0.87 (06)	15.59 (19)	5.11 (33)	0.16 (03)	1.31 (08)	4.23 (12)	3.81 (28)	1.84 (08)	0.36 (03)	0.807 (002)	n.d.	94.85 (61)	5.90 (09)	n.d.	<1	0.98						Spl	
KRA 20_0			20	60.78 (41)	0.87 (05)	15.65 (19)	4.67 (26)	0.13 (03)	1.30 (08)	4.24 (13)	3.62 (18)	1.73 (09)	0.38 (02)	1.312 (005)	n.d.	94.69 (55)	6.06 (07)	n.d.	0	1.01						-	
KRA 30_0			30	61.13 (35)	0.87 (05)	15.76 (23)	4.18 (28)	0.14 (03)	1.34 (07)	4.22 (18)	3.44 (19)	1.62 (08)	0.37 (02)	1.418 (003)	n.d.	94.48 (50)	6.11 (13)	n.d.	0	1.05						-	
<i>P=202 MPa, PH₂=9.4 bar,</i>																											
<i>log fO₂=-9.4/FMQ+0.7, 45 h</i>																											
KRA 0_0			19	61.44 (53)	0.85 (05)	15.76 (28)	5.12 (40)	0.16 (02)	1.38 (09)	4.47 (18)	3.82 (25)	1.79 (09)	0.37 (03)	n.d.	0.000 (000)	95.16 (90)	5.72 (10)	6.16 (01)	-	0.96						-	
KRA 0_2			20	61.08 (55)	0.88 (04)	15.45 (24)	5.02 (33)	0.16 (03)	1.44 (10)	4.41 (16)	3.93 (21)	1.83 (08)	0.36 (06)	n.d.	0.002 (000)	94.57 (81)	5.66 (11)	6.06 (03)	-	0.94						-	
KRA 0_5			20	61.23 (45)	0.86 (05)	15.50 (21)	5.05 (24)	0.15 (03)	1.37 (07)	4.42 (21)	3.97 (25)	1.79 (09)	0.37 (04)	n.d.	0.021 (000)	94.72 (63)	5.64 (16)	6.14 (04)	-	0.94						-	
KRA 0_10			20	61.99 (38)	0.87 (05)	15.83 (23)	4.47 (32)	0.16 (03)	1.39 (09)	4.58 (18)	3.98 (32)	1.79 (07)	0.35 (04)	n.d.	0.037 (000)	95.45 (73)	5.40 (07)	5.87 (03)	<1	0.94						FeS*	
KRA 0_15			20	62.09 (35)	0.87 (06)	15.79 (22)	4.02 (36)	0.16 (03)	1.46 (08)	4.42 (22)	3.94 (29)	1.80 (07)	0.36 (06)	n.d.	0.039 (000)	94.94 (70)	5.50 (06)	5.90 (02)	1	0.96						FeS*	

Notes: $S^{57}/\Sigma S$ is the S^{57} /total sulfur ratio determined by $\Delta \lambda$ (S K α) (Carroll & Rutherford, 1988), detailed description in the text; $\log fO_2$ [bar] derived from $S^{57}/\Sigma S$ (Wallace & Carmichael, 1994) (detailed description is given in the text); ΔFMQ is $\log fO_2$ [bar] relative to that of the FMQ-buffer reaction; n is the number of analyses. Number in parenthesis is 1 σ standard deviation of the mean x 100. FeO_{tot} is the total iron content. H₂O KFT and H₂O FTIR are the water concentrations in the melt determined by Karl-Fischer-Titration and Infrared Spectroscopy, respectively; Phase cont. is the total content of condensed phases in the product melt [vol.%] approximated by BSE pictures of EMP. A/CNK is the molar ratio of Al₂O₃/(CaO + Na₂O + K₂O). Phases are the mineral- or condensed S-bearing phases contained in the product melt. * composition of phases were quantitatively analysed by EMPA; the composition of FeS is shown in Table 10. The composition of OL, Cpx and Fe-oxides (Spl), is listed in the Appendix, Table A, B and C, respectively. ¹ subhedral anhydrite.

3. Analytical methods

3.1 Electron microprobe analysis (EMPA)

The experimental products were composed of homogeneous glass and in some experiments FeS, anhydrite (anh), spinel (spl), clinopyroxene (cpx) and olivine (OL). The chemical composition of experimental product glasses, minerals (spl, cpx and OL) and FeS was determined by EMPA. Anhydrite was qualitatively identified by EDX. The H₂O concentration in product glasses was measured by KFT and FTIR.

3.1.1 Analysis of glasses, FeS and mineral phases

EMPA of experimental glasses and mineral phases (OL, cpx and spl) was performed at the same beam conditions and counting times given in Chapter I §3.1. FeS phases were measured at 15 nA beam current and 8 s counting times of peak and background for Fe, Si, Ti, Al, Mg, Ca, Fe, Mn, Na and K and 40 nA beam current and 10 s counting times of peak and background for S analysis. The chemical composition of run products is given in Table 8 (product glasses), Table 10 (FeS) and in the Appendix: Table A, B and C (Ol, cpx and Fe-oxides, respectively).

3.2 Determination of sulfur speciation and fO_2

The S⁶⁺/ΣS ratio in most of the S-rich product glasses was determined by $\Delta\lambda(S\ K\alpha)$ peak shift method using EMPA (Carroll & Rutherford, 1988), where fO_2 was calculated using the S⁶⁺/ΣS ratios after Wallace & Carmichael (1994). A detailed description and the quantification of errors for the values of S⁶⁺/ΣS ratio and fO_2 is given in Chapter I §3.2.

3.3 Determination of H₂O concentration in the glasses

The concentration of the dissolved H₂O in all run product glasses was determined by Karl-Fischer-Titration (KFT) and FTIR spectroscopy as described in Chapter I (§3.3). Glass densities in g/l for dacitic product glasses were calculated, using the equation of Yamashita et al. (1997), modified in terms of density-water content relationship given by Ohlhorst et al. (2001):

$$\rho = (-11.8 \pm 2)c_{\text{water}} + (2515 \pm 6.6) \quad (4),$$

where the standard deviation is 6.6 g/l; C_{water} in wt.%.

It is noteworthy, although all glasses analyzed were nearly bubble free, some glasses (in particular at 100 MPa runs) contain up to ~10 vol.% anhydrous mineral phases (visually approximated at BSE images). Thus, the H₂O concentrations in these glasses are underestimated at KFT analysis for approximately ~10 rel.% (0.4 wt.% H₂O) at a maximum (considering vol.% and wt.% minerals being similar). The large uncertainties of approximated mineral contents do not allow for correction of KFT-data (absolute uncertainty of about 0.03-0.17wt.% H₂O). The experimental run conditions, specification and proportions of mineral- and S-bearing phases and the chemical composition of product glasses are listed in Table 8.

3.4 Determination of fluid composition

Fluid properties at experimental conditions will not be preserved after quenching and equations of state for a multicomponent S-Cl-O-H fluid is hitherto not satisfactorily verified. Thus in the following “fluid” will be used in terms of a simplified single fluid, defined to be solely composed of the volatile components S and/or Cl and H₂O added to the system.

Since partial extraction of alkalis (e.g., CaO, K₂O and Na₂O) from the melt into the fluid is expected (e.g., Candela & Piccoli, 1995; Williams et al., 1995, 1997; Student and Bodnar, 1999; Stelling et al., 2008), the fluid composition could not be reliably measured due to the small amounts (~2-3 μl) remaining in the capsules. The calculated loss of melt components to the fluid

was in most cases below the corresponding errors of EMPA. Thus, the fluid composition was determined by mass balance calculation taking the dissolved mass of S, Cl and H₂O into account (H₂O in the glass by KFT):

$$Cl_{melt} [mg] = \frac{Cl_{melt} [wt.\%] \times sample\ powder [mg]}{100 - (Cl_{melt} + S_{melt} + H_2O_{melt}) [wt.\%]} \quad (5)$$

$$S_{melt} [mg] = \frac{S_{melt} [wt.\%] \times sample\ powder [mg]}{100 - (Cl_{melt} + S_{melt} + H_2O_{melt}) [wt.\%]} \quad (6)$$

$$H_2O_{melt} [mg] = \frac{H_2O_{melt} [wt.\%] \times sample\ powder [mg]}{100 - (Cl_{melt} + S_{melt} + H_2O_{melt}) [wt.\%]} \quad (7).$$

The mass (in mg) of S, Cl and H₂O in the fluid ([S], [Cl] and [H₂O], respectively) was calculated by subtracting S_{melt}, Cl_{melt} and H₂O_{melt} from the loaded mass (bulk mass) of each component. We defined a fluid number, assigned as Cl# fluid (chlorine number), S# fluid (sulfur number) and H₂O# fluid (H₂O number) denoting the fluid composition as the weight proportion of S, Cl and H₂O in the fluid:

$$Cl\# fluid = \frac{[Cl]}{[Cl] + [S] + [H_2O]} \quad (8)$$

$$S\# fluid = \frac{[S]}{[Cl] + [S] + [H_2O]} \quad (9)$$

$$H_2O\# fluid = \frac{[Cl]}{[Cl] + [S] + [H_2O]} \quad (10).$$

The partitioning coefficient of Cl (Kd'Cl), S (Kd'S) and H₂O (Kd'H₂O) is the ratio of weight proportion of Cl, S and H₂O in the fluid and the weight proportion in the melt:

$$Kd'Cl = \frac{Cl\# fluid \times 100}{Cl_{melt} [wt.\%]} \quad (11)$$

$$Kd'S = \frac{S\# fluid \times 100}{S_{melt} [wt.\%]} \quad (12)$$

$$Kd'_{H_2O} = \frac{H_2O\#_{fluid} \times 100}{H_2O_{melt} [wt.\%]} \quad (13).$$

The fluid composition in terms of Cl# fluid, S# fluid and H₂O# fluid, the partitioning coefficients Kd'Cl, Kd'S and Kd'H₂O as well as the S/Cl ratios in the fluid and the S/Cl ratios in the melt (in wt.) are listed in Table 9. The fluid numbers and Kd' values do not account for the occurrence of Anh and FeS at sulfur saturation, since the precise amount of these phases is not known. Hence, this does not allow mass balance of sulfur between melt, fluid and S-bearing phases. In the following it is shown, that the anhydrite-saturated experiments follow general observed trends for melt and fluid composition, indicating the calculated fluid composition is not significantly affected by the presence Anh. The Kd'S values for the FeS-saturated melts containing the roughly estimated maximum of ~1 vol.% FeS (Table 8) should be overestimated for ~20-30 % in the Etna basalt resulting in Kd'S ~120-180 and for 35-50 % in the Krakatau dacite resulting in Kd'S ~270-500.

Table 9: Listing of the product fluid compositions in terms of Cl# fluid, S# fluid and H₂O# fluid, the partitioning coefficients Kd'Cl, Kd'S and Kd'H₂O and the S/Cl ratios in the product fluids and the product melts (in wt.):

Run #	S#	Cl#	H ₂ O#	Kd'		Kd'		Kd'		S/Cl	
				S	Cl	H ₂ O	fluid	melt			
0_02_2	0.01 (<0.01)	<0.01 (<0.01)	0.99 (0.14)	3.8 (0.5)	0.2 (<0.1)	19.0 (2.6)	50.8 (7.0)	2.7 (0.4)			
0_05_2	<0.01 (<0.01)	<0.01 (<0.01)	1.00 (0.06)	1.0 (0.1)	0.5 (<0.1)	19.0 (1.3)	17.7 (1.2)	8.1 (0.5)			
0_10_2	0.05 (<0.01)	<0.01 (<0.01)	0.95 (0.06)	6.9 (0.4)	0.3 (<0.1)	18.4 (1.1)	310.2 (19.2)	12.7 (0.8)			
0_15_2	0.14 (0.01)	<0.01 (<0.01)	0.86 (0.04)	16.0 (0.8)	2.5 (0.1)	16.8 (0.8)	118.0 (5.7)	18.1 (0.9)			
01_02_2	<0.01 (<0.01)	<0.01 (<0.01)	1.00 (0.13)	1.3 (0.2)	0.9 (0.1)	19.2 (2.6)	1.5 (0.2)	1.0 (0.1)			
01_05_2	0.01 (<0.01)	<0.01 (<0.01)	0.99 (0.06)	2.3 (0.1)	0.5 (<0.1)	18.8 (1.2)	11.1 (0.7)	2.5 (0.2)			
01_10_2	0.05 (<0.01)	<0.01 (<0.01)	0.95 (0.03)	6.9 (0.3)	1.1 (<0.1)	18.2 (0.9)	28.6 (1.4)	4.5 (0.2)			
01_15_2	0.16 (<0.01)	<0.01 (<0.01)	0.84 (0.02)	19.5 (0.6)	2.8 (0.1)	17.4 (0.6)	39.0 (1.4)	5.7 (0.2)			
05_02_2	0.01 (<0.01)	0.01 (<0.01)	0.98 (0.13)	13.6 (1.8)	1.5 (0.2)	19.3 (2.6)	1.6 (0.2)	0.2 (<0.1)			
05_05_2	0.02 (<0.01)	0.02 (<0.01)	0.96 (0.05)	4.6 (0.3)	3.2 (0.2)	18.4 (1.0)	1.0 (0.1)	0.7 (<0.1)			
05_10_2	0.06 (<0.01)	0.01 (<0.01)	0.93 (0.03)	10.3 (0.3)	1.4 (<0.1)	17.4 (0.6)	7.6 (0.3)	1.1 (<0.1)			
05_15_2	0.15 (<0.01)	0.02 (<0.01)	0.83 (0.01)	18.6 (0.4)	3.2 (0.1)	16.7 (0.4)	9.1 (0.2)	1.6 (<0.1)			
15_02_2	<0.01 (<0.01)	0.06 (0.01)	0.94 (0.12)	-	4.2 (0.5)	16.8 (2.2)	-	0.1 (<0.1)			
15_05_2	0.03 (<0.01)	0.06 (<0.01)	0.91 (0.04)	8.2 (0.4)	3.7 (0.2)	15.5 (0.8)	0.5 (<0.1)	0.2 (<0.1)			
15_10_2	0.05 (<0.01)	0.06 (<0.01)	0.89 (0.03)	7.2 (0.3)	3.8 (0.2)	16.1 (0.7)	0.9 (<0.1)	0.5 (<0.1)			
15_15_2	0.18 (<0.01)	0.07 (<0.01)	0.74 (0.02)	23.1 (0.6)	5.4 (0.1)	12.7 (0.3)	2.4 (0.1)	0.6 (<0.1)			
30_02_2	0.04 (0.01)	0.34 (0.05)	0.63 (0.09)	95.7 (15.6)	15.2 (2.2)	10.6 (1.6)	0.1 (<0.1)	<0.1 (<0.1)			
30_05_2	0.04 (<0.01)	0.32 (0.02)	0.64 (0.04)	12.5 (0.8)	13.9 (0.8)	11.4 (0.7)	0.1 (<0.1)	0.1 (<0.1)			
30_10_2	0.08 (<0.01)	0.32 (0.01)	0.60 (0.02)	14.3 (0.6)	14.3 (0.7)	10.3 (0.5)	0.2 (<0.1)	0.2 (<0.1)			
30_15_2	0.24 (0.01)	0.29 (0.02)	0.47 (0.03)	37.8 (2.8)	14.7 (0.9)	8.2 (0.5)	0.8 (0.1)	0.3 (<0.1)			

Table 9: Continued

Run #	S#	Cl#	H ₂ O#	Kd'		Kd'		Kd'		S/Cl		S/Cl	
				S	Cl	Cl	H ₂ O	fluid	melt				
0_15_2 ox	0.18 (0.01)	<0.01 (<0.01)	0.82 (0.04)	24.0 (1.3)	4.0 (0.3)	15.7 (0.8)	101.8 (5.5)	17.0 (0.9)					
01_15_2 ox	0.15 (0.01)	0.01 (<0.01)	0.85 (0.03)	19.4 (0.7)	4.0 (0.2)	16.0 (0.6)	27.5 (1.1)	5.7 (0.2)					
05_15_2 ox	0.17 (<0.01)	0.02 (<0.01)	0.81 (0.02)	23.8 (0.7)	4.8 (0.1)	14.6 (0.5)	7.3 (0.2)	1.5 (<0.1)					
15_15_2 ox	0.21 (0.01)	0.11 (<0.01)	0.68 (0.02)	32.5 (1.1)	10.5 (0.3)	12.5 (0.4)	2.0 (0.1)	0.6 (<0.1)					
30_15_2 ox	0.21 (0.01)	0.30 (0.01)	0.49 (0.01)	35.8 (1.3)	17.4 (0.5)	8.9 (0.3)	0.7 (<0.1)	0.3 (<0.1)					
0_15_2 red	0.20 (0.02)	<0.01 (<0.01)	0.80 (0.06)	163.7 (16.4)	0.3 (<0.1)	16.6 (1.3)	1090.5 (87.3)	2.2 (0.2)					
01_15_2 red	0.20 (0.02)	<0.01 (<0.01)	0.80 (0.08)	236.4 (32.5)	0.7 (<0.1)	18.4 (1.9)	180.1 (18.3)	0.5 (0.1)					
05_15_2 red	0.22 (0.01)	0.01 (<0.01)	0.77 (0.04)	172.8 (13.4)	1.7 (0.1)	16.0 (1.0)	22.6 (1.4)	0.2 (<0.1)					
15_15_2 red	0.25 (0.03)	0.05 (0.01)	0.70 (0.08)	225.1 (37.0)	3.1 (0.4)	14.3 (1.7)	5.5 (0.7)	0.1 (<0.1)					
30_15_2 red	0.23 (0.02)	0.20 (0.01)	0.57 (0.04)	210.4 (21.3)	8.8 (0.7)	12.9 (1.0)	1.2 (0.1)	<0.1 (<0.1)					
0_02_1	0.01 (<0.01)	<0.01 (<0.01)	0.99 (0.13)	8.6 (1.3)	-	29.0 (4.0)	-	2.3 (0.3)					
0_05_1	0.02 (<0.01)	<0.01 (<0.01)	0.98 (0.09)	6.3 (0.6)	-	27.5 (2.6)	-	8.9 (0.9)					
0_10_1	0.07 (<0.01)	<0.01 (<0.01)	0.93 (0.07)	13.7 (1.3)	0.2 (<0.1)	26.8 (2.0)	487.7 (37.2)	14.0 (1.3)					
0_15_1	0.17 (0.01)	<0.01 (<0.01)	0.83 (0.04)	34.4 (1.8)	1.6 (0.1)	30.4 (1.7)	204.5 (11.4)	2<0.1 (1.1)					
01_02_1	<0.01 (<0.01)	<0.01 (<0.01)	1.00 (0.22)	1.3 (0.3)	1.0 (0.3)	29.6 (6.6)	1.3 (0.3)	1.1 (0.2)					
01_05_1	0.05 (<0.01)	<0.01 (<0.01)	0.95 (0.05)	15.6 (1.0)	0.1 (<0.1)	24.1 (1.4)	253.7 (14.6)	2.8 (0.2)					
01_10_1	0.07 (0.01)	<0.01 (<0.01)	0.93 (0.13)	13.3 (1.9)	2.4 (0.5)	28.2 (4.1)	21.0 (3.0)	4.9 (0.7)					
01_15_1	0.18 (<0.01)	<0.01 (<0.01)	0.82 (0.02)	30.3 (1.0)	2.9 (0.1)	24.2 (0.7)	48.5 (1.4)	6.3 (0.2)					
05_02_1	-	0.02 (<0.01)	0.98 (0.14)	-	4.1 (0.6)	28.5 (3.8)	-	1.0 (0.1)					
05_05_1	-	<0.01 (<0.01)	1.00 (0.09)	-	0.2 (<0.1)	29.6 (2.7)	-	0.8 (0.1)					
05_10_1	0.07 (<0.01)	0.02 (<0.01)	0.91 (0.03)	12.7 (0.6)	4.4 (0.2)	27.5 (1.3)	3.6 (0.2)	1.2 (0.1)					
05_15_1	0.17 (<0.01)	0.02 (<0.01)	0.81 (0.02)	32.5 (1.1)	6.1 (0.2)	23.9 (1.2)	7.3 (0.4)	1.7 (0.1)					
15_02_1	0.02 (<0.01)	0.05 (0.01)	0.93 (0.14)	45.5 (7.3)	3.9 (0.6)	25.3 (3.8)	0.5 (0.1)	<0.1 (<0.1)					
15_05_1	0.03 (<0.01)	0.04 (<0.01)	0.93 (0.07)	9.1 (0.9)	3.4 (0.3)	24.8 (2.1)	0.7 (0.1)	0.3 (<0.1)					
15_10_1	0.08 (0.01)	0.08 (0.01)	0.84 (0.05)	19.6 (1.6)	7.6 (0.6)	23.0 (1.7)	1.0 (0.1)	0.5 (<0.1)					
15_15_1	0.20 (0.02)	0.10 (0.01)	0.70 (0.05)	49.4 (4.1)	12.6 (1.3)	18.9 (1.6)	2.0 (0.2)	0.6 (0.1)					
30_02_1	0.04 (<0.01)	0.20 (0.03)	0.76 (0.10)	73.0 (11.8)	8.9 (1.2)	19.5 (2.6)	0.2 (<0.1)	<0.1 (<0.1)					
30_05_1	0.05 (<0.01)	0.22 (0.02)	0.73 (0.07)	22.7 (2.4)	10.4 (1.1)	18.4 (1.7)	0.2 (<0.1)	0.1 (<0.1)					
30_10_1	0.10 (0.01)	0.22 (0.01)	0.68 (0.04)	31.1 (2.2)	11.3 (0.7)	17.2 (1.0)	0.5 (<0.1)	0.3 (<0.1)					
30_15_1	0.21 (0.01)	0.23 (0.01)	0.56 (0.02)	47.3 (2.0)	14.1 (0.6)	15.8 (0.6)	0.9 (<0.1)	0.4 (<0.1)					
0_15_1 ox	0.17 (0.01)	<0.01 (<0.01)	0.83 (0.05)	26.1 (1.6)	4.0 (0.3)	21.8 (1.4)	94.4 (6.0)	14.4 (0.9)					
01_15_1 ox	0.23 (0.02)	0.01 (<0.01)	0.76 (0.06)	38.1 (2.9)	4.6 (0.5)	19.2 (1.5)	41.4 (3.2)	6.3 (0.5)					
05_15_1 ox	0.22 (0.01)	0.02 (<0.01)	0.76 (0.05)	36.8 (3.1)	6.9 (0.5)	19.0 (1.3)	9.0 (0.6)	1.4 (0.1)					
15_15_1 ox	0.21 (0.03)	0.09 (0.01)	0.70 (0.08)	40.3 (6.7)	10.4 (1.3)	18.9 (2.4)	2.4 (0.3)	0.7 (0.1)					
30_15_1 ox	0.22 (0.02)	0.25 (0.02)	0.53 (0.05)	51.2 (6.0)	18.9 (1.7)	14.8 (1.3)	0.9 (0.1)	0.3 (<0.1)					
0-1050	-	0.01 (<0.01)	0.99 (0.03)	-	<0.1 (<0.1)	19.2 (0.7)	-	-					
1-1050	-	0.02 (<0.01)	0.98 (0.06)	-	4.0 (0.4)	18.7 (1.6)	-	-					
2-1050	-	0.06 (<0.01)	0.94 (0.07)	-	7.8 (0.8)	18.2 (1.9)	-	-					
3-1050	-	0.12 (0.01)	0.88 (0.06)	-	6.3 (0.6)	16.0 (1.6)	-	-					
4-1050	-	0.32 (0.03)	0.68 (0.05)	-	14.2 (1.6)	12.2 (1.4)	-	-					
KRA 0_0	-	-	1.00 -	-	-	17.4 (0.4)	-	-					
KRA 05_0	-	0.04 (<0.01)	0.96 (0.05)	-	9.0 (0.7)	16.8 (1.3)	-	-					
KRA 10_0	-	0.07 (<0.01)	0.93 (0.05)	-	8.2 (0.6)	15.8 (1.2)	-	-					
KRA 20_0	-	0.27 (0.02)	0.73 (0.05)	-	20.4 (1.9)	12.1 (1.1)	-	-					
KRA 30_0	-	0.49 (0.05)	0.51 (0.05)	-	34.2 (4.7)	8.4 (1.2)	-	-					
KRA 0_0	-	-	1.00 -	-	-	17.5 (1.8)	-	-					
KRA 0_2	0.04 (<0.01)	-	0.96 (0.10)	-	-	17.0 (1.9)	-	-					
KRA 0_5	0.11 (0.01)	-	0.89 (0.06)	541.6 (84.6)	-	15.7 (2.5)	-	-					
KRA 0_10	0.20 (0.01)	-	0.80 (0.02)	531.6 (38.2)	-	14.9 (1.1)	-	-					
KRA 0_15	0.29 (0.01)	-	0.71 (0.02)	744.9 (47.1)	-	12.9 (0.8)	-	-					

Notes: m is the mass. S#, Cl# and H₂O# ist the S, Cl or H₂O ratio (in wt.) in a simplified single fluid, defined to be solely composed of the volatile components S and/or Cl and H₂O (detailed description is given in the text). The partitioning coefficient of Cl (Kd'Cl), S (Kd'S) and H₂O (Kd'H₂O) is the ratio of weight proportion of Cl, S or H₂O in the fluid and the weight proportion of Cl, S or H₂O in the melt, respectively; S/Cl fluid is the ratio (in wt.) of S and Cl content in the fluid and S/Cl melt is the ratio (in wt.) of the S and Cl concentration in the melt.

4. Results

4.1 Description of experimental products

All experimental products contain hydrous glass and fluid phase, indicated by the occurrence of vesicles and a weight loss after piercing the capsule accompanied by the intensive smell of H₂S in the S-bearing reduced runs. The composition of all product glasses was trachybasaltic to basaltic using Etna basalt starting glass and dacitic using Krakatau dacite starting glass (Table 8). Most glasses contained mineral- or S-bearing phase (cpx, OL, spl, anh or FeS). The mineral content range between ~0-6 vol.% for glasses obtained at 200 MPa and ~1-10 vol.% for glasses obtained at 100 MPa. At all reduced runs (~FMQ+0.7) FeS (Chapter I, Fig. 2a) was stable. In the moderate oxidized H₂-buffered runs (~FMQ+2 to ~FMQ+3 or slightly below ~FMQ+4.2) mainly spinifex anhydrite and in one glass (intrinsic fO_2 ~FMQ+4.2) subhedral anhydrite was present (exp. 01_15_1 ox) (Fig. 15a,b) (where given fO_2 derive from monitored PH₂ (Shaw-membrane), from the intrinsic redox conditions or by approximation between the monitored PH₂ and the PH₂-load to the vessel (detailed description is given in the following §4.2)).

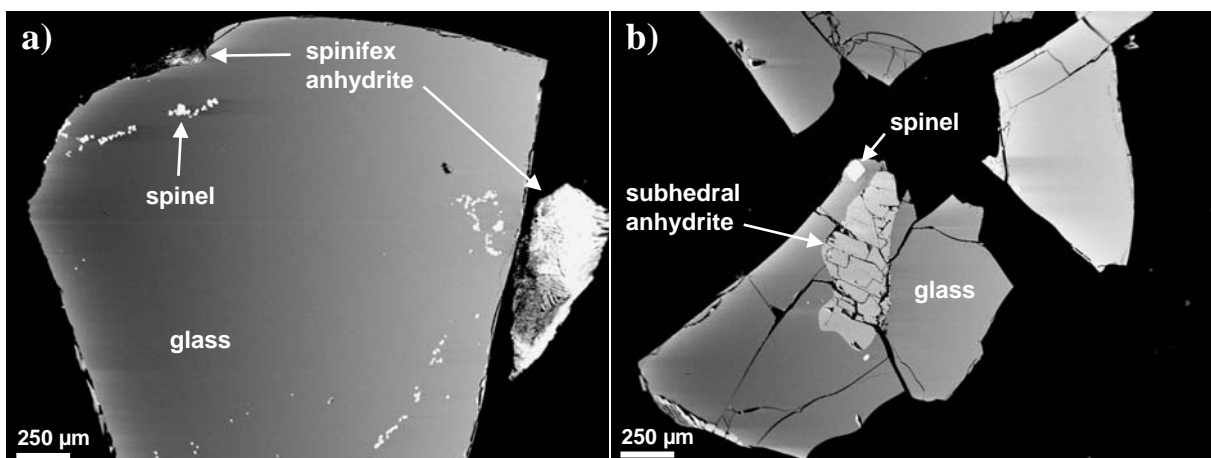


Fig. 15: BSE-pictures of spinifex anhydrite (exp. 05_15_1) (a) and subhedral anhydrite (exp. 01_15_1 ox) (b).

The crystal content of glasses decrease with increasing bulk Cl and bulk S and increases with fO_2 mainly as the spl content increases. At low fO_2 (\sim FMQ+0.7) the crystallinity of basaltic glasses is mainly increased by the presence of cpx, OL, FeS and minor spl.

4.2 Oxidation state of experimental glasses

The oxygen fugacity, calculated by monitored PH_2 at the IHPV runs (fO_2 [IHPV]) and fO_2 determined by melt S-speciation ($S^{6+}/\Sigma S$ ratio, error of \sim 0.13, detailed description in chapter I) is listed in Table 8. It is noteworthy, that in three experimental series at 100 MPa the monitored PH_2 was significantly below the expected values (exp. 01_02_1 to 01_15_1, 05_02_1 to 05_15_15 and 15_02_1 to 15_15_1), yielding fO_2 [IHPV] to be just below or higher than at intrinsic redox conditions. For these series fO_2 [IHPV] should be overestimated, because H_2 was added to the Ar-gas and thus fO_2 should be lower than at intrinsic redox conditions (fO_2 [IHPV] for these series are shown in parenthesis, Table 8). For all other experiments fO_2 [IHPV] ranged between \sim FMQ+0.7 to \sim FMQ+0.9 in the reduced series, \sim FMQ+1.9 to \sim FMQ+2.9 in the moderate oxidized series and \sim FMQ+4.2 in the most oxidizing series. The fO_2 determined by S-speciation (fO_2 [$S^{6+}/\Sigma S$]) ranged between \sim FMQ+0.3 to FMQ+0.5 ($S^{6+}/\Sigma S = 0.16$ -0.21) in the reduced melts, \sim FMQ+1.6 to FMQ+2.6 ($S^{6+}/\Sigma S = 0.78$ -0.98) in the moderate oxidized melts and \sim FMQ+1.9 to FMQ+2.3 ($S^{6+}/\Sigma S = 0.89$ -0.95) in the melts at intrinsic fO_2 IHPV. As it is shown by the S-speciation curve in chapter I (Fig. 24), fO_2 can not be calculated accurately by $S^{6+}/\Sigma S$ below \sim FMQ and above \sim FMQ+2, because $S^{6+}/\Sigma S$ becomes less dependent on oxygen fugacity, if fO_2 is below or above that of sulfide-sulfate transition. However, fO_2 [$S^{6+}/\Sigma S$] in the melts performed at intrinsic redox conditions is about 2 log units lower than fO_2 [IHPV]. Thus we suppose fO_2 [IHPV] being more accurate for the oxidized series. In the reduced series fO_2 [IHPV] and fO_2 [$S^{6+}/\Sigma S$] are in good agreement (reduced series: \sim FMQ+0.7 vs. \sim FMQ+0.3 to \sim FMQ+0.5, respectively). In the mediate oxidized series fO_2 [IHPV] and fO_2 [$S^{6+}/\Sigma S$] agree for

experiments at 200 MPa (≤ 0.6 log units difference), where at 100 MPa fO_2 [IHPV] is generally 0.5-1.0 log units higher. Thus, in the following we define fO_2 to be (1) FMQ+0.5 for the reduced series, (2) FMQ+2 at 200 MPa and FMQ+2.5 at 100 MPa for the H₂-buffered moderate oxidized series and (3) FMQ+4 at intrinsic fO_2 [IHPV].

4.3 Sulfur fugacity at FeS-saturation

The sulfur fugacity ($\log fS_2$ [bar]) in the FeS-saturated melts (Table 10) was determined by the equation of Bockrath et al. (2004) modified by Liu et al. (2007) to be -0.05 and -0.20 (for exp. 0_15_2 red and 01_15_2 red, respectively) taking fO_2 based on $[S^{6+}/\Sigma S]$ into account and calculated to be 0.2 in the whole FeS-saturated series by using the intrinsic fO_2 of the IHPV. The sulfur yielded values of 0.51 using fO_2 [IHPV] (where the given uncertainty of model is ± 0.5 log units). Applying the method of Toulmin & Barton (1964) fS_2 was determined to be -1.0 ± 0.9 in the basaltic melt (exp. 0_15_2 red) and 0.6 ± 0.3 and 1.2 ± 0.2 for the dacitic melts (exp. KRA 0_10 and KRA 0_15, respectively). Within error, fS_2 determined by both methods are in good agreement.

Table 10: Composition of FeS-phases contained in the basaltic and dacitic product glasses (in wt.%):

Run #	0_15_2 red	01_15_2 red	05_15_2 red	KRA 0_10	KRA 0_15
n	4	6	8	4	4
Fe	60.08 (76)	60.02 (67)	60.00 (98)	57.93 (57)	58.30 (20)
S	37.17 (87)	32.86 (295)	35.03 (400)	37.52 (41)	38.53 (16)
Total	97.25 (127)	92.88 (288)	95.03 (395)	95.45 (88)	96.82 (18)
Fe#	0.48 (01)	0.51 (02)	0.50 (03)	0.47 (00)	0.46 (00)
$\log fS_2$ (B;L):					
$[S^{6+}/\Sigma S]$	-0.20	-0.05	-	-	-
IHPV	0.20	0.20	0.20	0.42	0.51
N_{FeS}	0.963 (012)	-	-	0.940 (004)	0.930 (003)
$\log fS_2$ (T&B)	-1.0 (9)	-	-	0.6 (3)	1.2 (2)

Notes: Fe# is the molar ratio of $Fe_{tot}/(Fe_{tot} + S) \times 100$, assuming all iron is present as Fe^{2+} ; $\log fS_2$ (B;L) is $\log fS_2$ [bar], calculated by Bockrath et al. (2004) and Liu et al. (2007) taking fO_2 required in this model from S K α peak shift ($[S^{6+}/\Sigma S]$) or derived from monitoring of PH₂ in the vessel (IHPV). N_{FeS} is the molar fraction of FeS in pyrrhotite FeS-FeS₂; $\log fS_2$ (T&B) is $\log fS_2$ [bar] calculated by the method of Toulmin & Barton (1964).

4.4 Major element composition of experimental glasses (melts)

The major element composition of the glasses is listed in Table 8. The compositional variation illustrated in Fig. 16 and Fig. 17 is shown with respect to the S-, Cl- and H₂O-free basis normalized to 100%. The Cl-bearing melts vary mainly in concentration of alkalis (CaO, Na₂O and K₂O) (Fig.16) and FeO- and MgO content (Fig.17) (Table 8). In contrast, basaltic melts obtained at FMQ+0.5 do not show any significant variations in major element composition. The Cl-free S-bearing dacitic melts varying mainly in FeO content (exp. KRA0_0 to KRA 0_15) (Fig 17b, Table 8).

4.4.1 Concentration of alkalis (Na₂O, K₂O and CaO) in the melt

In this study, the Na₂O and K₂O concentrations in the basaltic melts decrease with bulk Cl (ranging from 0.05-3.6 wt.% Cl) for a maximum of 11 rel.% and 20 rel. %, respectively. Increasing bulk S (ranging from 0-2.0 wt.% S) leads to a maximum decrease in Na₂O for about 16 rel.% and in K₂O of about 12 rel.% (in total Na₂O decreases from 3.46 to 2.90 wt.% and K₂O decreases from 1.96 to 1.52 wt.% with increasing S and Cl). The CaO concentration is not significantly affected at lower bulk S (≤ 0.5 wt.% S) or at low fO_2 (FMQ+0.5) in the investigated range of Cl concentration in the system. At high bulk S (1.7-2.0 wt.% S, anhydrite-saturation) CaO decreases with bulk Cl for 15 rel.% at a maximum. At lower bulk S (≤ 1.0 wt.% S) CaO decreases for 13 and 15 rel.% at FMQ+2.5 and FMQ+4, respectively and for 12 rel.% at FMQ+2 (in total CaO decreases from 10.81 to 9.19 wt.%). At 100 MPa and anhydrite-saturation the decrease in alkali-concentration at FMQ+2.5 and FMQ+4 is nearly similar, whereas at FMQ+2 the decrease in alkali concentration is less pronounced (Fig. 16 a-d). In the S-free dacitic melts (FMQ+0.5) Na₂O and K₂O decrease with bulk Cl for about 9 rel.% (Na₂O decreases from 4.06 to 3.69 wt.% and K₂O decreases from 1.92 to 1.74 wt.%), whereas the CaO concentration remains constant.

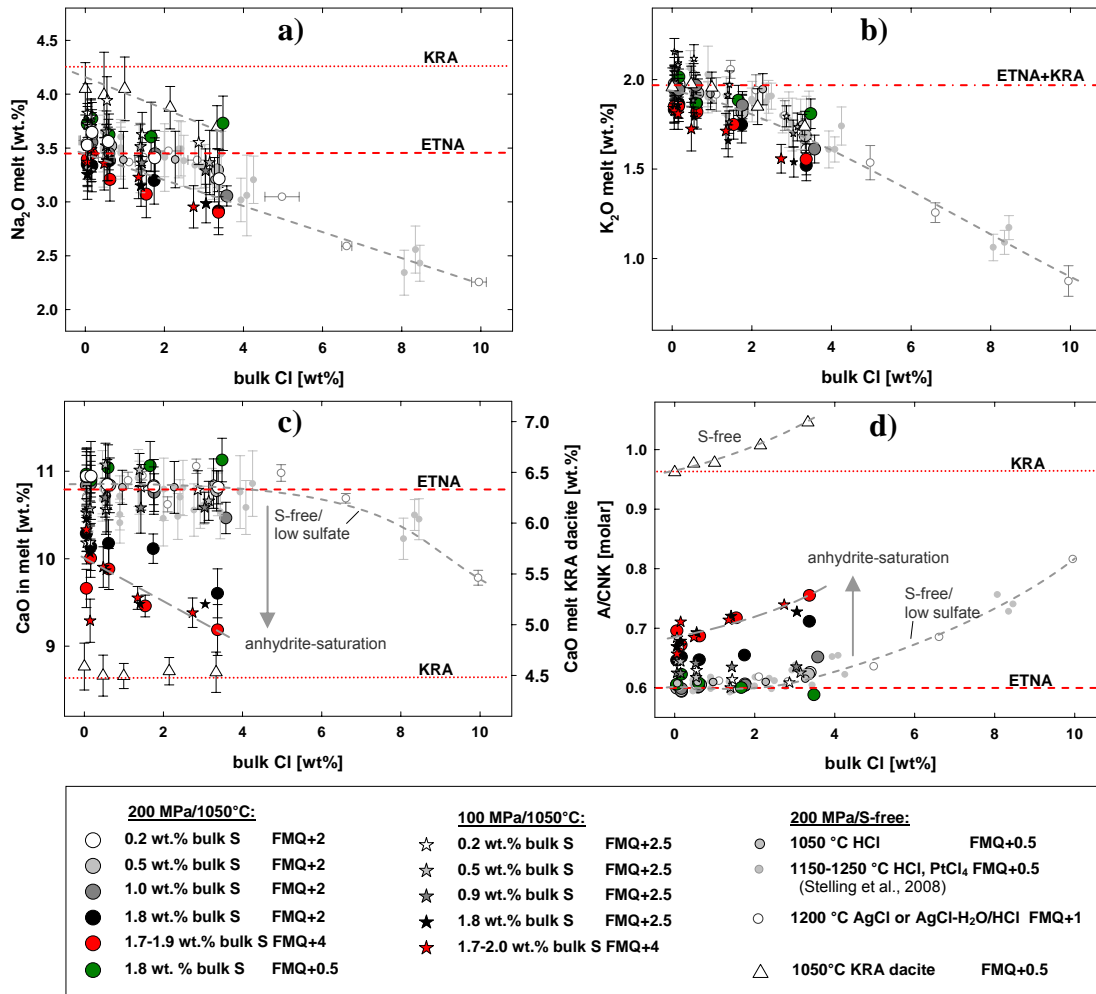


Fig. 16: Concentrations of Na₂O (a), K₂O (b), CaO (c) and the molar Al₂O₃/(CaO+Na₂O+K₂O) ratio as a function of the total amount of chlorine added to the system (bulk Cl). The alkali concentrations and A/CNK ratios of the basaltic and dacitic starting composition are illustrated by the red dashed lines (basalt) and the red dotted lines (dacite) or the red dashed-dotted line (basalt and dacite) (Fig.16b). Also shown are S-free data for Etna basalt at 200 MPa 1150-1250°C using HCl or PtCl as chlorine-source (Stelling et al., 2008) (small gray dots) and at 1200°C by using AgCl or AgCl-H₂O/HCl mixture as chlorine source (small open grey dots) and at 1050°C for Krakatau dacite (exp. KRA 0_0 to KRA 0_15) (open triangles). The S-free data for Etna basalt at 1050°C reported herein (exp. 0-1050 to 4-1050, small grey filled dots) are published by Stelling et al. (2008). The trends in the decrease of alkali concentrations and increasing A/CNK ratio with increasing Cl-concentration in the system are schematically shown for the S-free or sulfate-poor melts (short-dashed grey curves) and for the sulfate-bearing melts (long-dashed grey curves).

The variations in alkali contents are shown by the peraluminosity of the melt in terms of the A/CNK ratio (A/CNK = molar Al₂O₃/CaO+Na₂O+K₂O ratio) (Table 8, Fig.16d). The A/CNK ratio of the basaltic melts in this study increase with bulk Cl and bulk S (to the opposite as CaO decreases). The highest A/CNK ratios are observed at anhydrite-saturated melts at

FMQ+2.5 and FMQ+4 (where the A/CNK ratio increases in total from 0.60 to 0.72). It is remarkable, that in the S-free dacitic melts A/CNK ratios increase from 0.96 to 1.05 with bulk Cl, whereas in both, the S-free basaltic melts and S-bearing basaltic melts at FMQ+0.5 A/CNK is not affected by Cl at investigated chlorine concentration in the system. It is noteworthy, that the CaO concentration in the sulfate-bearing melts are decreased to a greater extend at bulk Cl of ~3 to 3.5 wt.% compared to the S-free basaltic melts of Stelling et al. (2008) and the AgCl-data (Fig.16c). The decrease of K₂O is more likely a function Cl concentration in the system (Fig.16b) and the decrease in Na₂O (Fig.16a) is effected by both S and Cl concentration in the system.

4.4.2 MgO and FeO concentration in the melt

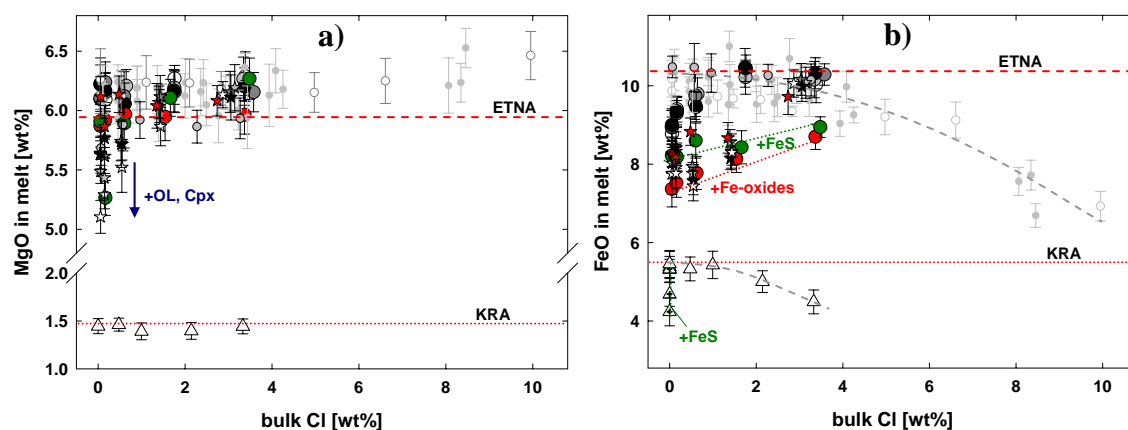


Fig. 17: Concentrations of MgO (a) and FeO (b) in the basaltic and dacitic melts dependent on the total amount of chlorine added to the system (bulk Cl); same symbols as used for Fig.16. In addition the FeO content of the (Cl-free) FeS-saturated dacitic melts (crossed triangles) is shown. The change in MgO- and FeO concentrations in the basaltic melts compared to the starting compositions is mainly effected by the occurrence of crystalline phases: melts coexisted with OL and cpx were depleted in MgO, where the FeS-saturated melts (as indicated by the green dotted line) or those coexisting with Fe-oxides (spl) (illustrated by the red dotted line) were depleted in FeO. The increase in MgO- and FeO contents in the basaltic melts with up to ~3.5 wt.% bulk Cl is mainly the result of a decrease in mineral content with increasing chlorine concentration in the system. It is remarkably shown by the data of Stelling et al. (2008) (small gray dots) and by the those (crystal-free) AgCl-data (small open grey dots) (see text for description), that for more than 4 wt.% Cl in the system, the FeO content in the basaltic melts significantly decreases with a further increase of bulk Cl. The (FeS-free) dacitic melts (open triangles) become depleted in FeO, if bulk Cl increases for more than ~1 wt.% Cl in the system (as illustrated for both starting compositions by the gray dashed curves). The S-bearing dacitic melts (crossed triangles) are depleted in FeO, if FeS is present.

The MgO concentration in the melt (Fig.17a) mainly decreases with increasing abundance of Mg-bearing mineral phases (OL and cpx). Since the crystallinity of the melt decreases as bulk Cl and bulk S increase (except at coexistence of a S-bearing mineral phase), the decrease in MgO becomes less as bulk Cl and bulk S increase. The lowest MgO content is observed at exp. 0_02_1 at 100 MPa (FMQ+2.5) (Fig.17a) (5.12 ± 0.18 wt.% MgO, 14 rel.% less than the starting glass), where the crystal content (mainly OL and cpx) is approximately 10 vol.%. At 200 MPa MgO-bearing mineral phases are less abundant. Except at exp. 01_15_2 red (FMQ+0.5) containing ~6 vol.% minerals (FeS, spl, OL, cpx) MgO is decreased for about 12 rel.%. The MgO content in the dacitic melts ($1.39-1.54 \pm 0.8-0.11$ wt.% MgO; MgO contents of the (Cl-free) S-bearing dacitic melts are not graphically shown) was within error mainly constant and similar to the MgO content of the starting glass (Fig.17a), which is expected by their low crystallinity (mineral content ≤ 1 vol.%).

The FeO content in the basaltic melts (Fig. 17b) is mainly decreasing with increasing content of Fe-oxides (spl) in the melt (observed at FMQ+2 and above). Since Fe-oxides become less abundant with increasing bulk Cl, the decrease in FeO content of the melt becomes less with increasing bulk Cl. At low fO_2 (FMQ+0.5) FeO mainly decreases due to the precipitation of FeS (Fig.17b). In the Cl-free dacitic melts the FeO content decreases with bulk S for about 22 rel.% at a maximum. The FeS-saturated basaltic melts (constant bulk S of about 1.8 wt.%) are depleted in FeO content for about 16-22 rel.%. In the S-free dacitic melts FeO decreases, if the Cl concentration in the system increases to values above ~1 wt.% Cl, whereas the maximum decrease in FeO content (20 rel.%) is observed at highest investigated bulk Cl (~ 3.5 wt.% Cl) (Fig.17b).

4.5 H₂O, Cl and S concentrations of melt and fluid phase

The concentrations of H₂O, Cl and S (in wt.%) analysed in the product glasses are listed in Table 8. In the investigated range of system composition, the concentrations of H₂O, Cl and S dissolved in the basaltic melts range between 4.43-5.86 wt.% H₂O, 0.05-2.27 wt.% Cl and 0-0.85 wt.% S at 200 MPa and 2.72-4.01 wt.% H₂O, 0.05-2.20 wt.% Cl and 0.05-0.64 wt.% S at 100 MPa. In the dacitic melts (200 MPa and FMQ+0.5) the H₂O, Cl and S contents range between 5.40-6.11 wt.% H₂O, 0-1.42 wt.% Cl (S-free) or 0-0.04 wt.% S (Cl-free).

The composition of fluid phase is listed in Table 9 and plotted in Fig.18 in terms of H₂O# fluid, Cl# fluid and S# fluid. The composition of fluid coexisting with the basaltic melts ranges between 47-99 wt.% H₂O, 0-32 wt.% Cl and 0-23 wt.% S at 200 MPa and 52-100 wt.% H₂O, 0-25 wt.% Cl and 0-25 wt.% S at 100 MPa. The composition of fluid coexisting with the dacitic melts (200 MPa) ranges between 51-100 wt.% H₂O and 0-49 wt.% Cl in the S-free system and 71-100 wt.% H₂O and 0-29 wt.% S in the Cl-free system.

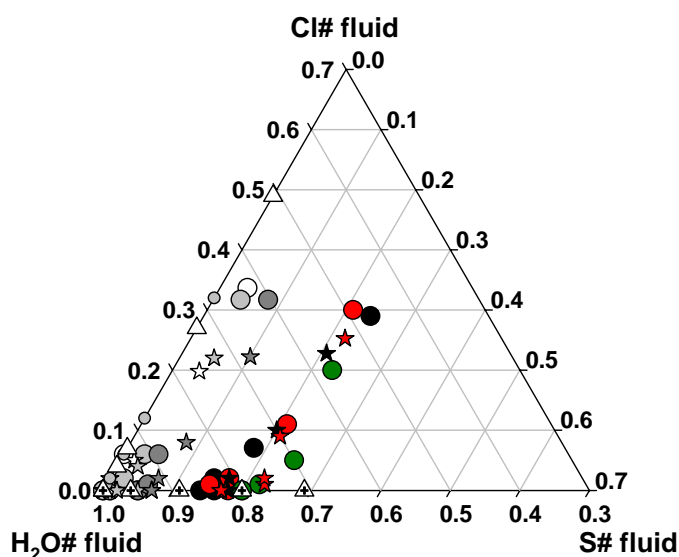


Fig. 18: Composition of the fluids accounting for the simplified three component fluid system Cl-S-H₂O coexisting with the basaltic and dacitic melts (calculated by mass balance, as described in §3.4); same symbols as used in Fig.16 and Fig.17. The chlorine-, sulfur- and H₂O numbers (Cl# fluid, S# fluid and H₂O# fluid) are the weight proportion of Cl, S or H₂O, respectively accounting for a three component fluid system solely composed of Cl-S-H₂O.

4.5.1 Effect of chlorine on the H₂O concentration in the melt

Fig. 19 illustrates, that the H₂O content in the melt slightly increases with the Cl concentration in the melt confirming the results Stelling et al. (2008) for crystal-free melts (including the S-free experiments: 0-1050 to 4-1050, reported herein).

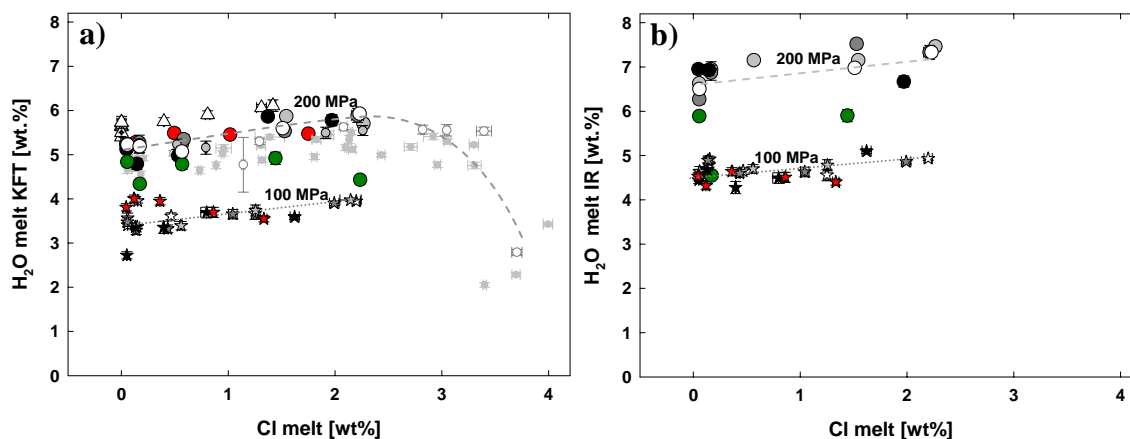


Fig. 19: Illustration of the slightly positive relationship between Cl content in the melt and H₂O content in the melt (increasing H₂O content with Cl melt to a maximum at ~2-3 wt.% Cl melt) (H₂O determined by KFT, Fig.19a and by IR, Fig.19b). The slightly increase in H₂O melt is observed for both P investigated in this study (200 MPa and 100 MPa). At low Cl concentrations in the melt (in particular at 100 MPa) H₂O melt determined by KFT (Fig.19a) is in some cases underestimated (for a maximum of approximately 0.4 wt.% H₂O, detailed description in §3.3). The IR-data also exhibit a positive correlation between Cl melt and H₂O melt in the investigated range of system composition (Fig.19b). The decrease of H₂O melt at Cl melt above ~3 wt.% Cl as observed by Stelling et al. (2008) (small gray dots) is also indicated by the AgCl-data (small open grey dots) (description is given in the text). The dashed grey curve and the dashed grey lines are guides to the eye representing the observed trends; same symbols as used in Fig.16.

By using H₂O melt [wt.%] determined by KFT, we have to omit those melts containing higher amounts of mineral phase(s) in order to describe the dependence of Cl concentration in the melt on H₂O concentration in the melt. However, although H₂O melt determined by FTIR is overestimated, these data (supposed to be not affected by the presence of mineral phase(s)) display a slight generally increase of H₂O melt with Cl melt (Fig.19b). It is remarkable, that the H₂O content determined by KFT systematically increase with the Cl concentration (Fig.19a) in those melts containing less amounts of mineral phase(s) (approximately below 4 vol.%, mainly observed at 200 MPa and FMQ+2 in the S-bearing and FMQ+0.5 in the S-free basaltic melts and

observed for all dacitic melts). The H₂O content (by KFT) in the low crystalline basaltic melts at FMQ+2 (S-bearing) and FMQ+0.5 (S-free) increases for about 10-15 rel.%, if Cl melt increases from about 0.05 to ~1.97-2.26 wt.% Cl (total increase in H₂O from 5.13-5.23 to 5.70-5.93 wt.%). The H₂O concentration in the dacitic melts (by KFT) increase for about 7 rel.% (in total from 5.73-6.11 wt.% H₂O), if Cl melt increases from 0 (Cl-free runs) to 1.42 wt.% Cl. An effect of sulfur on the H₂O concentration in the melt was not observed. These data are in good agreement to the observed positive correlation between Cl melt and H₂O melt with a maximum H₂O content at about ~2.5 wt.% Cl in the melt (Fig.19a). Our data for the fluid system AgCl-HCl and AgCl-H₂O follow the same trend of Cl melt and H₂O melt as observed in this study and to data of Stelling et al. (2008) where PtCl₄ was used as Cl-source.

4.5.2 Mutual effects of chlorine and sulfur on S and Cl concentration in the melt

The Cl and S concentrations in the melt respectively increase non-linear with Cl and S content in the system and Cl and S concentration in the fluid phase (Fig.20a-d). This indicates non-ideal distribution of Cl and S between melt and aqueous fluid, in agreement to former studies (e.g., Webster et al., 1992, 1999; Signorelli & Carroll, 2000, Stelling et al., 2008). Non-ideal mixing properties of S between silicate melt and hydrous fluid are indicated by few experimental studies addressed from rhyolitic to phonolitic-trachytic melt composition (e.g., in a Cl-free system: e.g., Parat & Holtz, 2005 (rhyolite at ~FMQ+4); in a Cl-bearing system: e.g., Botcharnikov et al., 2004 (rhyolite at ~FMQ+0.7); Scaillet & McDonald, 2006 (rhyolite at ~FMQ-1.5 to ~FMQ+0.5) and Webster et al., 2009b (phonolites-trachytes at ~FMQ+1.2 to FMQ+2.3).

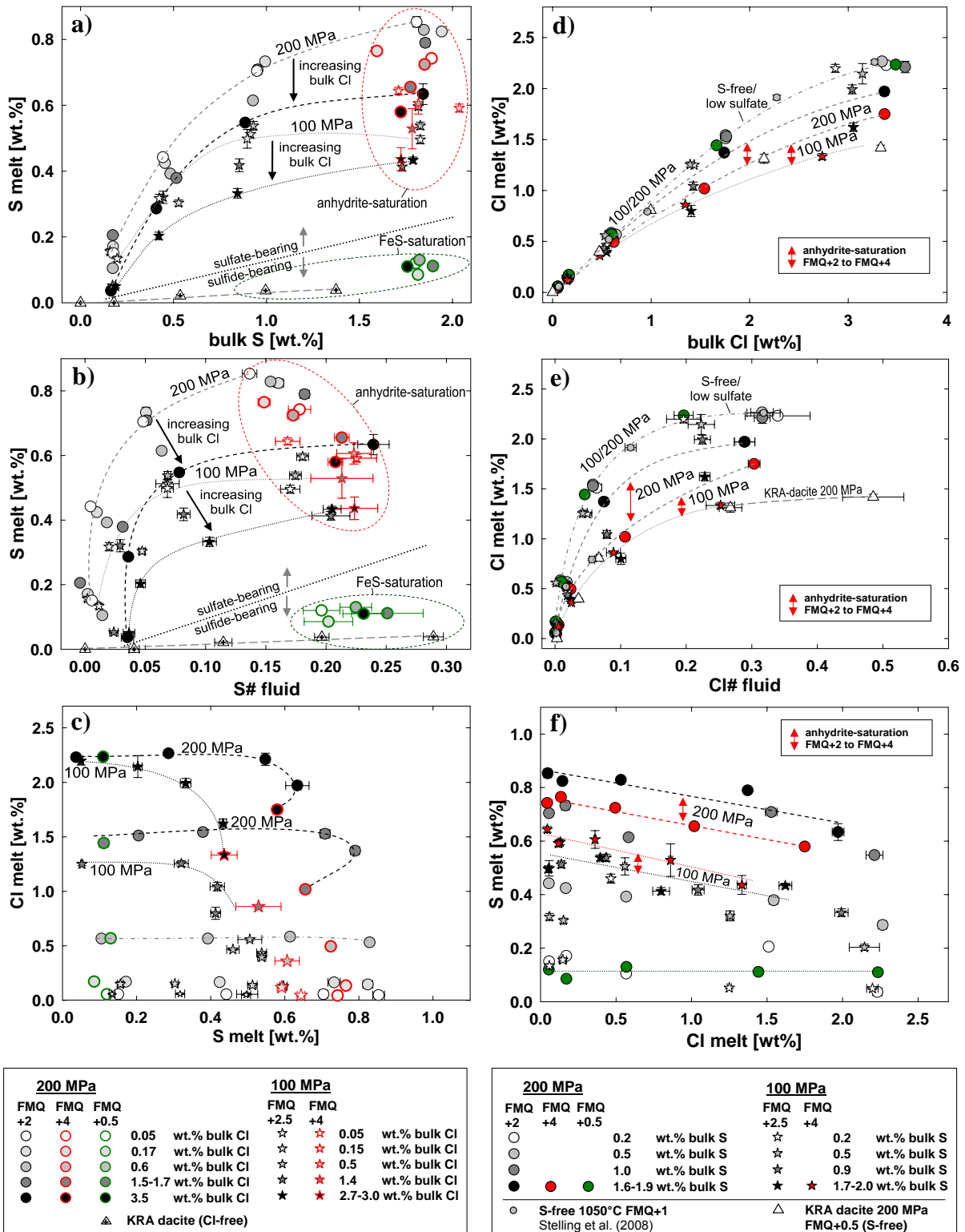


Fig. 20: Illustration of the mutual effects of Cl and S (a-d). Fig. 20a,b show the correlation between bulk S (Fig.20a) or S# fluid (Fig.20b) on the S concentration in the (dominantly) sulfate-bearing basaltic melts (shown above the black dotted line, which separates the sulfate- from the (dominantly) sulfide-bearing systems, indicated by the two gray arrows) with respect to increasing chlorine concentration in the system (bulk Cl). The anhydrite-saturated data are covered by the red ellipse, where the FeS-saturated data of basalt and dacite are covered by the green ellipse. The sulfide-dominated systems of (Cl-free) dacite (crossed triangles) and (Cl-containing) basalt (green dots) show significant lower amounts of S dissolved in the melt, compared to the sulfate-bearing system. The dashed and the

small dotted curves representing eye-guiding lines for data at 200 MPa and 100 MPa, respectively, where gray denotes a Cl-poor system and black denotes a Cl-rich system. The relationship between bulk S and S# fluid on the S content in the dacite is shown by the gray long-dashed curve. Fig.20d,e illustrate the relationship between bulk Cl (Fig.20d) or Cl# fluid (Fig.20e) on the Cl content in the melt with respect to the S concentration in the system. The dashed-dotted curves are guides to the eye representing the data at 100 and 200 MPa for the sulfate-poor systems and the S-free system; other line-symbols are the same as in Fig. 20a,b. The red arrows indicate the difference in Cl-content at anhydrite-saturation for QFM+4 and FMQ+2 (200 MPa) or FMQ+2.5 (100 MPa) (detailed description is given in the text at §4.2). The data of the KRA dacite are marked with an eye-guiding line (Fig.20e). It is remarkable, that the Cl solubility data for the S-free dacitic melts are comparable to the data of the basaltic melts obtained at anhydrite-saturation and 100MPa (at FMQ+4) (red stars). Fig.20c,f display the inverse relationship of S and Cl concentration in the melt. Fig.20c shows that the S content mainly in the anhydrite-(sub)saturated melts (where the data of anhydrite-saturation can be taken from Fig.20a,b) decrease, if Cl melt increases from 1.4-1.8 wt.%. It is noteworthy, that the eye-guiding lines for the 200 MPa data are reversing, because S- and Cl concentration of the anhydrite-saturated melts at FMQ+4 (red encircled dots) are lower at comparable system composition (detailed description is given in the text). Fig.20f illustrates the effect of Cl melt on S melt. S melt decreases mainly constant with Cl melt only in the sulfate-bearing systems. The trend of the effect of Cl melt on S melt is accentually shown for the anhydrite-saturated data, where the red dashed and the red dotted curve represent data at FMQ+4 (at 200 MPa and 100 MPa, respectively) and the black dashed and dotted curves represent data at FMQ+2 and FMQ+2.5 (at 200 MPa and 100 MPa, respectively). The S content in the FeS-saturated melts is not affected by Cl melt (shown by the green dotted line).

The correlation between S and Cl concentrations in the system and Cl and S concentrations in the fluid and melt phase was investigated for basaltic melt composition at 200 and 100 MPa at various redox conditions (FMQ+0.5, FMQ+2, FMQ+2.5 and FMQ+4). Fig 20a-d illustrates, that the relationship between Cl and S is complex and strongly dependent on the redox conditions of the system. The concentration of S and Cl in the melt vary inversely with one another at oxidizing conditions (\geq FMQ+2), where S^{6+} is the dominating S species (Fig.20f). At nearly similar system composition (with respect to slightly lower bulk Cl and bulk H₂O at 100 MPa (Table 7 and described in §2.3) and similar fluid composition (Fig.18), the Cl and S concentrations in the melt are in general about 0-15 rel.% lower for Cl and 30 rel.% for S at 100 MPa compared to 200 MPa (Fig.20a,b). The difference in Cl melt between 100 MPa and 200 MPa becomes larger with increasing bulk S and S# fluid. At reduced conditions (FMQ+0.5 and 200MPa) no mutual effects of Cl and S was observed (Fig.20a-d). The Cl and S concentrations

in the FeS-saturated melts vary between 0.06-2.24 wt.% Cl (Fig.20b,d) and 0.09-0.13 wt.% S (which is about 10-15 rel.% of the S content at anhydrite-saturation at 200 MPa and various bulk Cl) (Fig. 20a,c).

4.5.3 Effect of Cl on the S concentration in the melt

Fig.20a,b illustrates the effect of Cl concentration in the system and the effect of Cl concentration in the melt, respectively on the S concentration in the melt. At $fO_2 \sim FMQ+2$ and above, increasing bulk Cl at fixed bulk S leads to a significant decrease in S concentration in the melt (and a slight increase in S concentration in the fluid, resulting from mass balance calculation). At 200 MPa S melt decreases with bulk Cl for a maximum of about 12 rel.% at FMQ+2 and 23 rel.% at FMQ+4, observed at anhydrite-saturation. In total the S content at anhydrite-saturation decreases from 0.85 to 0.63 wt.% S at FMQ+2 and 0.74 to 0.58 wt.% S at FMQ+4, if bulk Cl increases from ~ 0.05 to 3.5 wt.% Cl (and Cl# fluid increases from ~ 0 to 0.3). It is noteworthy, that at 200 MPa the S concentration (at fixed bulk Cl) in the anhydrite-saturated melts is about 9-13 rel.% lower at FMQ+4 than at FMQ+2.

At 100 MPa and FMQ+2.5 the S content in the melt is decreased to a maximum of about 27 rel.% at highest bulk Cl (3.0 wt.% Cl) and highest Cl# fluid (0.23), observed at anhydrite-saturation. At these P- and fO_2 -conditions the S melt concentration at anhydrite-saturation is about 20 rel.% higher at slightly higher bulk Cl (0.15 wt.% and Cl# fluid ~ 0) compared to lowest bulk Cl (0.05 wt.% and Cl# fluid ~ 0) (in total 0.60 wt.% S vs. 0.50 wt.% S, respectively). However, no systematic effect of Cl on the S concentration in the melt for bulk Cl ≤ 0.55 wt.% was observed. Since the composition of these melts follow the general observed trends in main element concentration depending on bulk S, bulk Cl and fO_2 , this deviation from the expected systematic relationship of Cl on S content in the melt can not be directly explained by S- and Cl enforced alkali extraction and coexistence of mineral phases (Fig.16a-d, Table 8) or by possible larger deviation in fO_2 from $\sim FMQ+2.5$ (in particular for those runs with lower monitored PH_2

than expected). However, the maximum decrease of S concentration in the melt is observed at anhydrite-saturation, high bulk Cl and high Cl# fluid (decrease in S content of about 32 rel.% (at 1.41 wt.% bulk Cl and Cl# fluid ~0.10) and 28 rel.% (at 3.05 wt.% bulk Cl and Cl# fluid ~0.23), resulting in S contents in the melt of 0.41 and 0.43 wt.% S, respectively) (Fig.20a,c). It is remarkable, that at 100 MPa and FMQ+4 the S content in the melt systematically decreases with bulk Cl for a maximum of about ~31 rel.% (at 2.74 wt.% bulk Cl and Cl# fluid ~0.25), observed at anhydrite-saturation (with a total decrease in S content from 0.64 to 0.44 wt.% S). In contrast to lower S contents at anhydrite-saturation observed for FMQ+4 and 200 MPa, the S content at anhydrite-saturation at 100 MPa is in general about 7 rel.% higher at FMQ+4 compared to FMQ+2.5 (for similar system composition).

4.5.4 Effect of S on the Cl concentration in the melt

Fig.20b,d illustrates the effect of S concentration in the system and the S concentration in the melt, respectively on the Cl concentration in the melt. Increasing S concentration in the system at fixed bulk Cl leads to a decrease in Cl concentration of the melt. This effect is more pronounced at FMQ+4 compared to FMQ+2 and FMQ+2.5. Thus, at 200 MPa Cl melt decreases for about 10-12 rel.% at FMQ+2 and for about 10-32 rel.% at FMQ+4, if bulk S increases from ~0.2 to 2 wt.% S. This results in a total Cl concentration of about 1.97 and 1.75 wt.% Cl at highest bulk Cl (~3.5 wt.%) and highest Cl# fluid (~0.3). At low bulk S (~0.2 wt.%) and low S# fluid (~0 to 0.01) (not investigated at FMQ+4) the Cl concentration in the melt at FMQ+2 (2.23 wt.% Cl) is similar to that observed at reduced conditions (FMQ+0.5) for both, S-free and S-bearing systems (2.26 and 2.24 wt.% Cl, respectively). At 100 MPa the Cl concentration in the melt decreases for about 13-26 rel.% at FMQ+2.5 and for about 20-40 rel.% at FMQ+4, if bulk S increases from ~0.2 to 2 wt.%. In total the Cl content in those melts obtained at highest bulk Cl (~3 wt.%) and highest Cl# fluid (~0.25) is decreased to 1.62 wt.% Cl at FMQ+2.5 and 1.33 wt.% Cl at FMQ+4. The maximum observed Cl concentration at 100 MPa, obtained at low bulk S

(0.19 wt.%) and low S# fluid (0.04) was determined to be 2.20 wt.% Cl. It is worthy noted, that all S-free basaltic melts reported herein (exp. 0-1050 to 4-1050) (Stelling et al., 2008) containing 2.26 wt.% Cl at a maximum (at 200 MPa) were below Cl-saturation, which is expected to be about 4 wt.% Cl (Stelling et al., 2008).

4.5.5 Correlation between Cl and S concentrations in the melt

The direct relationship between Cl melt and S melt is illustrated in Fig. 20c,f. At both investigated pressures (200 and 100 MPa) sulfur reduces the Cl concentration in the melt, if (1) the Cl concentration in the system is higher than ~0.5-0.6 wt.% Cl (Cl# fluid > ~0.02) and (2) the melt is anhydrite-(sub)saturated (Fig.20c). In contrast chlorine decreases the S concentration in the melt approximately linear with increasing Cl concentration in the melt for a maximum of about 0.1-0.2 wt.% S independent on P and the S concentrations in the system (Fig.20f). At low fO_2 (FMQ+0.5) no mutual effects of Cl melt and S melt can be observed.

5. Discussion

5.1 S and Cl partitioning between melt and fluid

In Fig.21 the partitioning coefficients K_d^S and K_d^{Cl} are shown as a function of S- and Cl concentrations in the melt- (a, c) and the S- and Cl proportions in the fluid phase (Cl# fluid and S# fluid) (b, d) at fixed S and Cl concentration in the system. Since we observed non-linear (non-ideal) mixing properties of Cl and S between fluid and melt (shown in Fig. 20a,b,d,e), K_d^{Cl} and K_d^S increase with increasing Cl- and S concentration in the melt- and increasing Cl- and S concentration in the fluid (Cl# fluid and S# fluid), except for K_d^S at low S content in the system, as described in the following. The partitioning coefficients of sulfur (a,b) range between $K_d^S = 1.3 \pm 0.2$ to 37.8 ± 2.8 in the sulfate-rich systems at FMQ+2 to FMQ+4. In the sulfate-poor systems K_d^S ranges between $162-236 \pm 16$ to 37 for the FeS-saturated basaltic melts and ranges between $532-745 \pm 38$ to 65 for the FeS(sub)-saturated dacitic melts. The partitioning behavior of sulfur is largely influenced by increasing bulk Cl, if sulfate is the dominating S species and the S concentration in the system is low (0.2 wt. % bulk S). Thus, in the sulfate dominated systems (FMQ+2 to FMQ+4), K_d^S increases from 1.3 ± 0.2 to 95.7 ± 15.6 at low bulk S (0.2 wt.% S) (illustrated by the grey thin dotted curves in Fig.21a,b), if bulk Cl increases from 0.05 to ~3.5 wt.% Cl (observed at FMQ+2 and 200 MPa). At higher S concentrations in the (sulfate dominated) system the influence of Cl on S partitioning is still significant and K_d^S increases systematically at fixed bulk S (mainly independent on P) with increasing bulk Cl (from ~0.05 to 3-3.5 wt.% Cl) to a maximum of about 200 rel.%. The partitioning coefficients of chlorine (Fig.21c,d) increase with Cl melt (Fig.21b) and Cl# fluid (Fig.21d) from $K_d^{Cl} \sim 0$ to 18.9 ± 1.7 in the basaltic melts and from $K_d^{Cl} \sim 0$ to 34.2 ± 4.7 in the dacitic melts. In general chlorine partitions into the fluid to a greater extent at S-rich (sulfate-rich), oxidizing systems (~FMQ+2 and above).

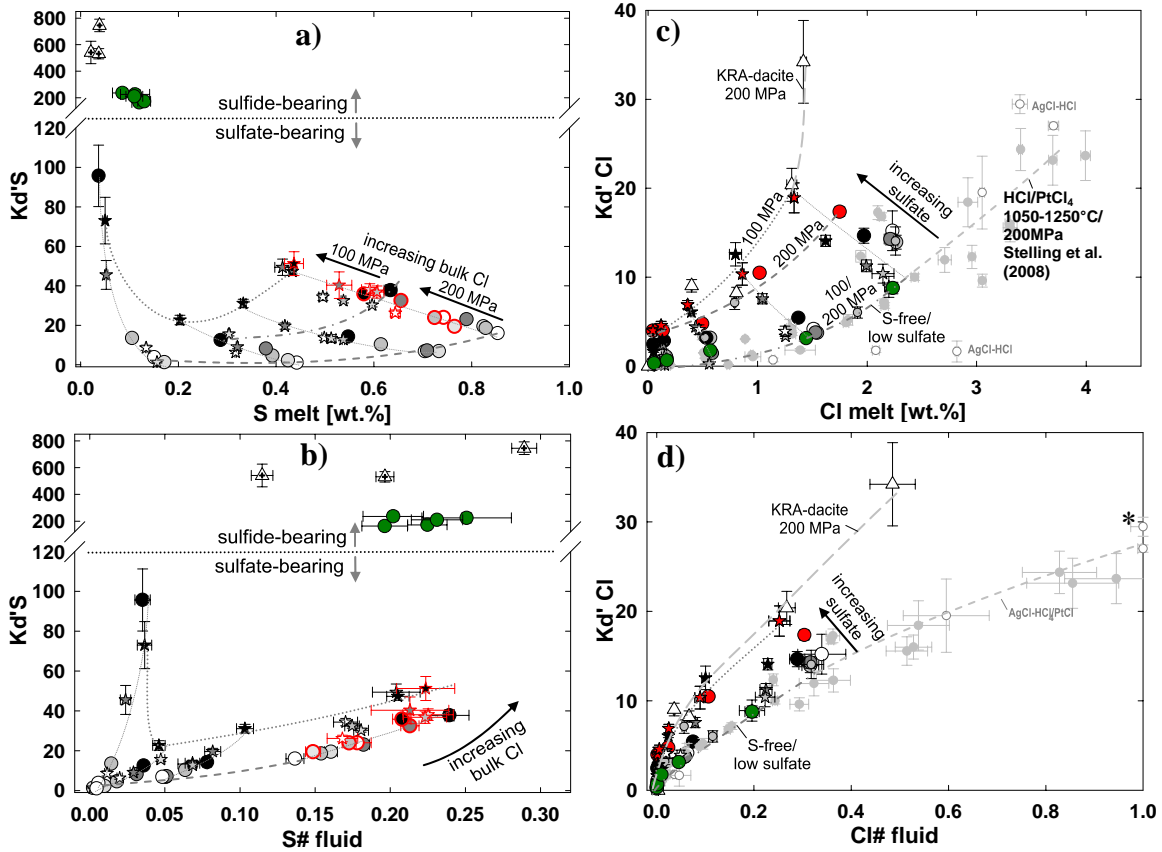


Fig. 21: Fig. 21a-d show the partitioning coefficients of sulfur and chlorine ($K_d'S$ and $K_d'Cl$) as a function of the S- and Cl concentration in the melt (a, c) and the S- and Cl proportion in the fluid ($S\#$ fluid and $Cl\#$ fluid) (b, d). Fig. 21a,b illustrate that $K_d'S$ for the sulfide-bearing systems of (Cl-free) dacite (crossed triangles) and (Cl-bearing) FeS-saturated basalt (green dots) are about one and two orders of magnitude higher (for basalt and dacite, respectively) than compared to $K_d'S$ of the sulphate-bearing systems. The effect of increasing Cl concentration in the system on $K_d'S$ is illustrated by the black arrow, where the grey thin dotted curves represent the changes in $K_d'S$ with bulk Cl at fixed S content in the system. It is well demonstrated, that chlorine enforces the S partitioning into the fluid being mostly pronounced at low S contents in the system, resulting in low S concentration in the melt (a) and comparable high $S\#$ fluid (b). In general $K_d'S$ at 100 MPa is about 2-times higher than for comparable system compositions at 200 MPa (a, b), where both series at different pressure are separated by the grey dashed-dotted curve (a), although there is a slight overlap of data between both series, in particular at lower S melt and lower $S\#$ fluid. The grey thick dotted and the grey thick dashed curves representing data for high bulk Cl and low bulk Cl, respectively (a, b). Fig. 21c,d illustrate the effect of sulfur as sulfate on $K_d'Cl$ over the whole range of investigated system composition. The grey thin dotted lines follow the trend of $K_d'Cl$ changing with sulfate at comparable system compositions (accentuated by the black arrows). The dark grey dashed-dotted curve represents data at 100 and 200 MPa for basalt, the grey dotted and the grey dashed curves are eye-guiding lines for the sulfate-rich (anhydrite-saturated) data at 100 and 200 MPa, respectively (c, d). Also shown are data for KRA-dacite at 200 MPa (long-dashed grey curve), S-free data of Stelling et al. (2008) at 1050-1250°C and 200 MPa, including HCl and $PtCl_4$ as Cl-source (small gray dots) and the AgCl-data (small open grey dots); * $Cl\#$ fluid for both AgCl-data were set to 1 (as described in the text and in the Appendix Table E); other symbols are explained in Fig. 20.

This effect is most pronounced at highest investigated fO_2 (FMQ+4), where $Kd'Cl$ at fixed Cl# fluid is in general increased for about 250 rel.% compared to S-rich (dominantly sulfide-rich) reduced systems at $fO_2 \sim FMQ+0.5$ (with $Kd'Cl$ at FMQ+4 up to 17.4 ± 0.6 (at 200 MPa) and 18.9 ± 1.7 (at 100 MPa) and $Kd'Cl$ at FMQ+0.5 up to 8.8 ± 0.7 at 200 MPa). At low S (sulfate-dominated) concentration in the system, $Kd'Cl$ at 100 MPa and $Kd'Cl$ at 200 MPa at fixed system composition and comparable fO_2 are mainly similar. At high S (sulfate-dominated) concentration in the system (FMQ+4) $Kd'Cl$ increases with Cl melt to a larger extend ($\sim 200\%$) at 100 MPa compared to 200 MPa (c,d). The Cl partitioning-behavior in the system AgCl-H₂O/HCl-fluid and basaltic melt at 1200°C differs significantly from that observed for the system HCl-fluid and basaltic melt at 1050-1250°C (Fig.21c) (including data of Stelling et al., 2008). Thus, Cl seems to partition more preferentially into the melt with up to 2.8 wt.% of dissolved Cl in the melt, if an AgCl-H₂O/HCl mixture is used as Cl source, instead of HCl. At higher Cl concentrations in the melt (≥ 3 wt.% Cl), $Kd'Cl$ of the AgCl-data and those of Stelling et al. (2008), where PtCl or PtCl-H₂O mixtures were used as Cl source are similar at comparable chlorine content in the melt (as illustrated by the grey dashed-dotted curve in Fig.21c,d. It is noteworthy, that the amounts of H₂O dissolved in the melt for the marked (*) two AgCl-data (exp. A-10 and HClA 3, Appendix Table E, F) were higher than the H₂O contents initially added to the system, indicating that H₂O was generated by reducing the melt (e.g., Fe³⁺ to Fe²⁺) due to equilibration of PH₂ between vessel and sample capsule. Since we assume that nearly all H₂O at these experiments was dissolved in the melt, we defined the chlorine number of the product fluid to Cl# fluid = 1. As a result $Kd'Cl$ for both AgCl-data might be overestimated.

5.2 Cation extraction from the melt into the fluid

The losses of cations (mainly Ca^{2+} , Na^+ and K^+) from the melt with increasing Cl melt as shown in Fig.16 can be well explained by the dissolution of Ca-, Na- or K-sulphates in the Cl-enriched fluids.

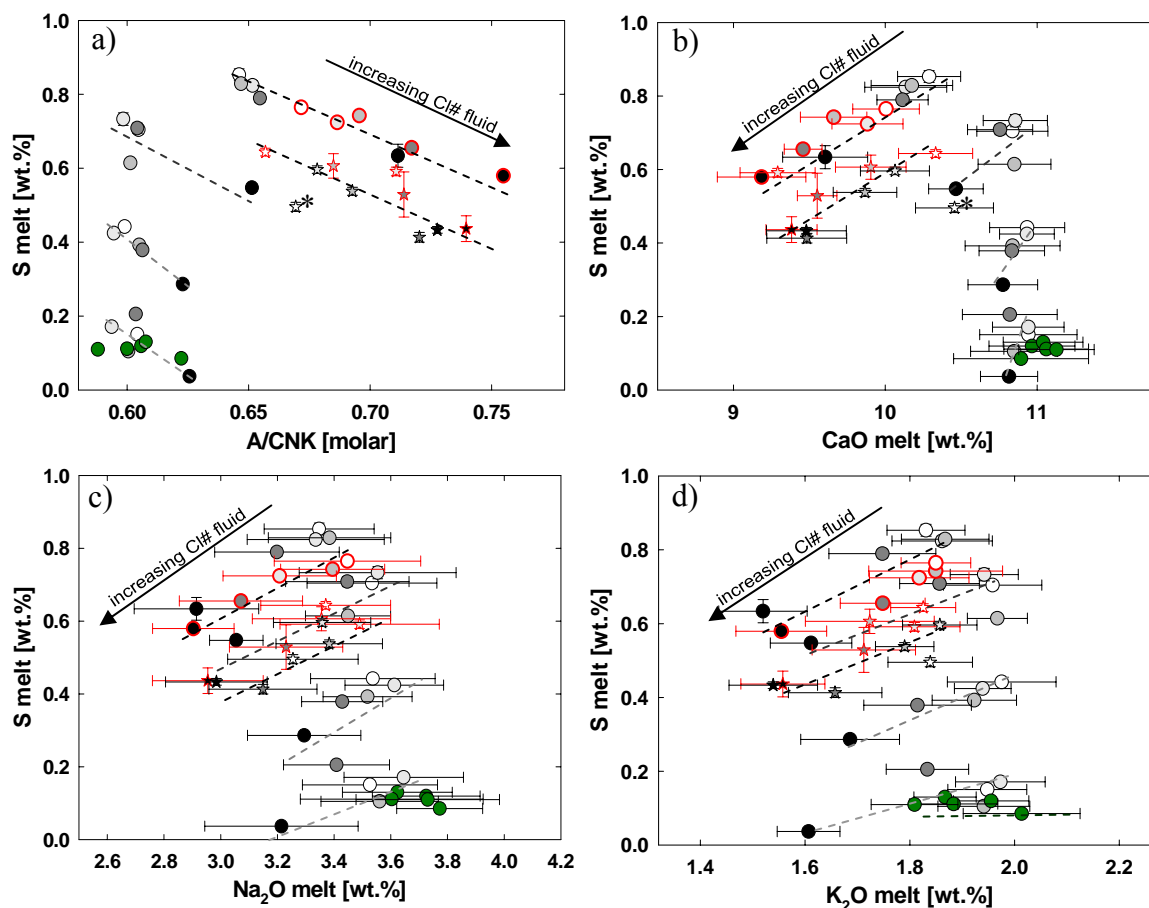
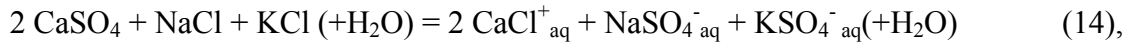


Fig.22: Fig.22a-d illustrates the chlorine enforced cation-extraction from the basaltic melts due to the Cl-enforced dissolution of cation-sulfates (CaSO_4 , Na_2SO_4 and K_2SO_4) from the melt into the fluid (as discussed in the text). The dashed lines showing the almost linear correlation between the A/CNK ratio (a) or the alkali contents (b-d) and the amounts of sulfur dissolved in the melt at fixed S concentrations in the system (same symbols as in Fig. 16). The black and red symbols represent data at anhydrite-saturation. The black arrows indicate the increase in Cl# fluid ranging from ~ 0 to 0.25-0.34 for all sulfate-dominated systems and Cl# fluid from ~ 0 to 0.20 in the FeS-saturated basaltic melt; *exp. 0_15_01 at 100 MPa (crystallinity ~ 3 vol.%): H_2O melt (KFT) is about 25-35 rel.% less than for other melts obtained at 100 MPa, containing comparable amounts of crystals (~ 1 -3 vol.%); same symbols as in Fig.20.

Newton & Manning determined the solubility of CaSO_4 in NaCl - H_2O solutions being about 200 times higher at X_{NaCl} of 0.3 (or Cl# fluid = 0.3) (5-6 molal) compared to pure H_2O

(0.03 molal) (at 800°C and 10kbar). Webster et al. (2009b) observed a dramatic increase of CaSO₄ solubility with increasing X_{(Na,K)Cl} in aqueous fluids determined to be 22 molal at X_{(Na,K)Cl} ~0.3 (at 904-927°C and 200 MPa) and proposed a strong positive effect of T on the CaSO₄ solubility. Webster et al. (2009b) observed S-bearing fluids stripping alkalis from the melt (where they used NaCl and KCl as chlorine source) due to the reaction:



where they referred X[±]_{aq} to be the charged species dissolved in the aqueous fluids. Since we used HCl solutions as Cl source, we suppose following reaction occurring in our sulfate-bearing system enforcing the extraction of alkalis mainly CaO (and to a minor content Na₂O and K₂O) from the melt into the fluid:

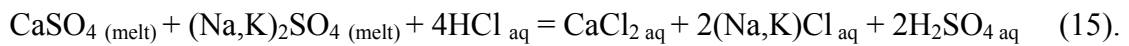


Fig.22 illustrates the approximately linear relationship between Cl-enforced cation loss from the melt (also shown in terms of A/CNK ratio, Fig.22a) and decreasing S content in the melt due to eq.15. Because the statistical errors of EMPA analyses for Na₂O and K₂O were mostly larger than the observed differences in Na₂O and K₂O concentrations in the melts, we can not provide accurate quantification of Na- and K load from the melt into the fluid.

Furthermore, precipitation of anhydrite in our sulfate-saturated melts do not allow for precise calculation of Ca contents load to the fluid. However, taking a positive T-dependence on CaSO₄ solubility in NaCl-H₂O solutions together with the solubility data at 800°C (Newton & Manning, 2005) and ~900°C (Webster et al., 2009b) into account, we conclude our fluids obtained at higher T (1050°C) become significantly enriched in Ca and to a minor extend enriched in Na and K with increasing Cl# fluid and increasing S# fluid.

5.3 The effect of cation extraction on S and Cl fluid/melt-partitioning

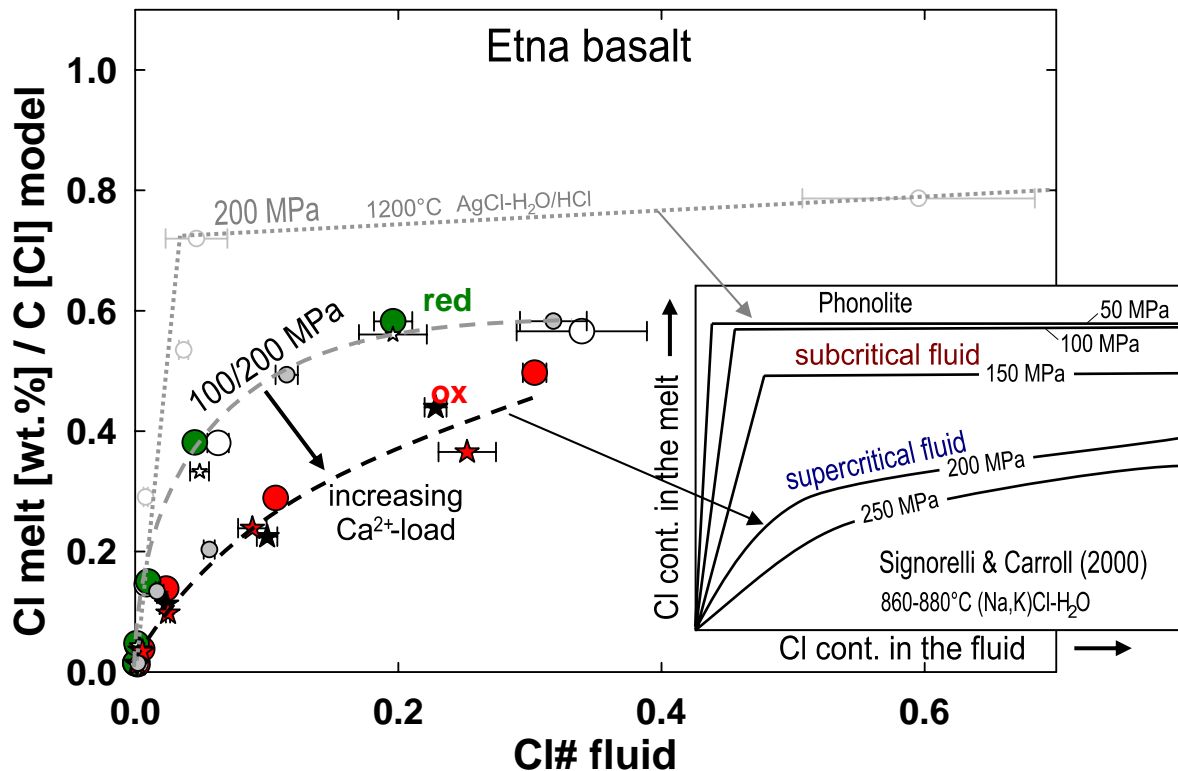


Fig.23: Fig 23. shows the correlation between the chlorine concentration in the fluid ($Cl\#$ fluid) and the Cl concentration in the melt normalized to the maximum Cl solubility given by the model of Webster & DeVivo (2002), by excluding correction terms recommended by the model for our melt compositions (as explained in the text). The shown data correspond to the basaltic S-free or sulfate-poor melts (marked with “red”, means data include reduced runs at FMQ+0.5, green dots) and the anhydrite-saturated melts (marked with “ox”, means oxidized runs at FMQ+2 to FMQ+4), same symbols as in Fig.16. The dashed lines follow our datasets (at 1050°C, 100 and 200 MPa) (grey dashed line: S-free or sulfate-poor systems, black dashed line: anhydrite-saturated systems). The black thick arrow illustrates the change in the partitioning-behavior of chlorine with increasing Ca^{2+} -load to the fluid, in particular occurring at sulfate-rich systems. The dotted grey line illustrates the partitioning-behavior of chlorine in the system $AgCl-H_2O/HCl$ fluid-basaltic melt at 1200°C and 200 MPa. The Figure included on the right is a sketch given by Signorelli & Carroll (2000) (modified) illustrating their data for Cl partitioning in the system $(Na,K)Cl-H_2O$ fluid-phonolitic melt at $T=860-880^\circ C$ and a P range of 50-250 MPa (where Cl cont. means the chlorine concentration). With respect to the data of Signorelli & Carroll (2000) our data at 1050°C for 100 and 200 MPa (HCl as Cl source) indicate the presence of a supercritical fluid (shown by the thin black arrow), whereas the $AgCl$ -data may represent subcritical fluid properties (fluid-unmixing) (shown by the gray arrow). The strong linear increase of the chlorine concentration in the melt at low $Cl\#$ fluid is supposed to be the result by the nearly ideal partitioning-behavior of chlorine between a single hydrous Cl fluid phase and silicate melt occurring at low P (e.g., Shinohara et al., 1989, Shinohara, 1994; Williams et al., 1997; Signorelli & Carroll, 2000; Shinohara, 2009).

Fig.23 shows the Cl melt concentration normalized to the maximum solubility calculated for each data point by the model of Webster & Vivo (2002). Therefore we excluded correction terms recommended by the authors for our melt compositions, because the uncorrected Cl solubility ranging between 3.5-4 wt.% Cl for our melts is similar to the experimental determined Cl solubility in Etna basalt of ~4 wt.% (Stelling et al., 2008). Fig.23 indicates, that the difference of the chlorine partitioning-behavior between the S-free or low sulfate containing melts and the anhydrite-saturated melts is more likely the result of changing the fluid properties than changing the Cl-solubility due to variations in melt composition. The data Signorelli & Carroll (2000) for Cl partitioning between (Na,K)Cl-H₂O fluid and phonolitic melt at 860-880°C and P ranging from 50 to 250 MPa illustrate, that the partitioning-behavior of chlorine is strongly dependent on pressure (at ~constant T) (sketch in Fig.23). The non-linear partitioning-behavior of chlorine for our investigated range of system composition at 1050°C and P=100 and 200 MPa is comparable to that observed by Signorelli & Carroll (2000) at similar or higher P (200 and 250 MPa) and may represent the presence of a supercritical fluid. However, for the in system AgCl-H₂O/HCl fluid and basaltic melt at 1200°C and 200 MPa the chlorine partitioning-behavior is comparable to that obtained by Signorelli & Carroll (2000) at T=860-880°C and low to moderate P (50-150 MPa), being the result of subcritical fluid properties, where the fluid unmixes into a H₂O-rich Cl vapor phase and a hydrosaline liquid (or hydrosaline brine) (e.g. Webster, 2004).

We would expect the occurrence of fluid unmixing in our sulfate-rich systems, because of the significant alkali-extraction from the melt into the fluid (mainly Ca²⁺, but also Na⁺ and K⁺, Fig.22b-d), because of two aspects (1) the higher fluid immiscibility for the ternary system H₂O-NaCl-KCl compared to that of the binary systems H₂O-NaCl- or H₂O-KCl (e.g., Gunter et al., 1983; Chou et al., 1992; Sterner et al., 1992) and (2) shifting the critical pressure to higher values, due to the increases Ca-load in the fluid (e.g., Bischoff et al., 1996; Duan et al., 2006). However, the fluid composition for the experiments of Signorelli & Carroll (2000) obtained at higher pressures (200 and 250 MPa) may have been more complex than the ternary system

(Na,K)Cl-H₂O fluid, because (1) increasing chlorine concentration in the fluid enforces the extraction of cation from the melt (e.g., Candela & Piccoli, 1995; Williams et al., 1995, 1997; Student and Bodnar, 1999; Stelling et al., 2008) and (2) the solubility of cations in hydrous fluids increase with increasing P (e.g. Gunter et al., 1983; Bischoff & Rosenbauer, 1985, 1988; Bodnar et al., 1985; Chou, 1987; Bischoff & Pitzer, 1989; Chou et al., 1992; Sterner et al., 1992; Bischoff et al., 1996; Duan et al., 2006; Driesner et al., 2007a, 2007b). Thus, we suppose the partitioning-behavior of chlorine in our sulfate-rich or anhydrite-saturated systems is mainly similar to that observed by Signorelli & Carroll (2000) at higher pressure, because of the higher complexity of fluid composition for both systems. Our AgCl-data (at 1200°C and 200 MPa) indicate that the critical pressure is shifted to higher values in the fluid system AgCl-H₂O/HCl compared to that of HCl and ± alkali-cations, because Stelling et al.(2008) did not observed any difference in the partitioning-behavior of chlorine at 200 MPa and T ranging from 1050-1250°C by using HCl as Cl source, where the data of Stelling et al. (2008) at 1050°C are shown in Fig.23 (small gray dots).

Webster et al. (2009b) determined Cl concentrations in phonolitic to trachytic melts coexisting with Cl-S-H₂O vapour (S dominantly as sulfate) and saline liquids (e.g., NaCl, KCl, CaCl₂) decreased to a maximum of 33 rel.% compared to S-deficient systems (at 200 MPa, T = 896-1022 °C and ~FMQ+1.2 to ~FMQ+2.3). The same authors suggested that the presence of sulfur in the melt and fluid phase reduces the Cl activity. A change of Cl activity due to the presence of S-bearing hydrous fluid was also mentioned by Botcharnikov et al. (2004) suggesting H₂S and SO₂ complexing with Cl⁻ and hence effecting H₂O-Cl mixing properties. We suppose the Cl-enforced Ca-cation load to the fluid due to the dissolution of CaSO₄ from the sulfate-rich melts causes an increase of fluid complexity and significantly effect the Cl activity in the fluid.

The effect of chlorine on the partitioning behavior of sulfur in our fluid-melt systems (Fig.20a,b and Fig.21a,b) can be interpreted to be directly the result of decreasing S

concentration in the melt, due to the Cl enforced dissolution of sulfates (mainly CaSO_4) from the melt into the fluid (Fig.22 and eq.15). This relationship is well demonstrated by the high observed K_d 's at low bulk S and high bulk Cl (Fig.21a,b). For this system composition, mainly all S (complexed to sulphate) dissolves in the fluid and only a negligible amount of S remains dissolved in the melt. The fact, that anhydrite-saturation occurs, even though the S concentrations in the melt decreased with bulk Cl (Fig.20a,c) or Cl melt (Fig.20f) may be a result in decreasing sulfate capacity of the melt by the Cl enforced extraction of CaO (and $\text{Na}_2\text{O} + \text{K}_2\text{O}$) from the melt (Fig.22a-d, eq.15).

However, the partitioning-behavior of sulfur between aqueous fluid and multicomponent silicate melts is hitherto not well constrained. Experimental data of Moune et al. (2008) indicate linear partitioning of sulfur (dominantly as sulfide) between aqueous fluid and basaltic and andesitic melts at 1050°C and 300 and 200 MPa, respectively (but only few S-undersaturated data are included in this study). Furthermore, Keppler (2010) determined S partitioning coefficients between aqueous fluid and haplogranitic melt at 750-850°C, 50 to 300 MPa and $f\text{O}_2$ ranging from ~FMQ-1 to ~FMQ+3 being constant (indicating ideal partitioning behavior of sulfide and sulfate) at given P-, T- and redox conditions with up to 7 wt.% S in the fluid (corresponding to S# fluid of 0.07) (where K_d 's ranged in total from 47-468). In contrast, non-ideal partitioning behavior of sulfur (dominantly as sulfide) between aqueous fluid and rhyolitic melts in Cl-bearing systems was observed by Botcharnikov et al. (2004) (at ~FMQ+0.7) (K_d 's of 18 to 108) and is indicated by data of Scaillet & McDonald (2006) (at ~FMQ-1.5 to ~FMQ+0.5). Further non-linear mixing properties of sulfur (dominantly as sulfate) between Cl- H_2O fluid and phonolitic-trachytic melts was observed by Webster et al. (2009b) (at ~FMQ+1.2 to FMQ+2.3) yielding K_d 's of ~2.4 to 1095. In Cl-free systems non-linear S partitioning (S dominantly as sulfate) between aqueous fluid and rhyolitic melts was obtained by Parat & Holtz (2005) (at ~FMQ+4). However, the studies cited above indicate, that the partitioning-behavior of sulfur between hydrous fluid and natural multicomponent melts is complex. However according

to Keppler (2010) obtaining a linear partitioning-behavior of sulfur in a comparably low complex fluid-melt system, we suppose, that the mixing properties of sulfur between aqueous fluid and silicate melt strongly depend on the complexity of the system composition (total composition of fluid and melt). Thus, the S partitioning behavior between aqueous fluid and multicomponent natural melts will differ from ideality.

5.4 Implication to the natural magmatic system of Mt.Etna

Variations in the S/Cl ratio of volcanic gases were observed to be directly correlated to the volcanic activity for instance at the andesitic magmatic system of the Soufrière Hills volcano (Montserrat, West Indies) (Edmonds et al., 2001, 2002), the shoshonitic and potassic alkaline system of Vulcano (Vulcano Island, Aeolian Islands, Italy) (Di Liberto et al., 2002) or the basaltic system of Mt.Etna (Sicily, Italy) (e.g., Aiuppa et al., 2002, 2004, 2007, 2008).

In the case of Mt.Etna it is argued that Mt.Etna's eruption can be triggered by injection of juvenile volatile-rich, S-rich magma (Corsaro et al., 2007, 2009; Métrich et al., 1993; Clocchiatti et al., 2004; Andronico et al., 2005; Viccaro et al., 2006, 2008; Spilliaert et al., 2006a,b; Ferlito et al., 2008, 2009). During passive degassing stages at Mt.Etna's 2002-2003 eruption the highest S/Cl ratios in the emitted gases were observed (~7, in wt.%). On the contrary those gases emitted at high volcanic explosivity yielded S/Cl ratios of ~0.4-2 (Aiuppa et al., 2004). The volatile contents of Mt.Etna's OL melt-inclusion (OL-MI) range between ~0.27-0.35 wt.% S and ~2-3.5 wt.% H₂O for the most primitive OL-MI and between 0.03-0.18 wt.% S and 0.3-1.3 wt.% H₂O for the more evolved OL-MI and OL-glass embayments, where the Cl concentration increases from ~0.15-0.26 wt.% Cl accompanied to the degree of melt evolution (Spilliaert et al., 2006a,b). Aiuppa et al. (2002, 2004, 2008) and Spilliaert et al. (2006a,b) interpreted magmatic gas-/fluid phases with high S/Cl ratios were released by primitive volatile, S-rich magma, as represented by the primitive OL-MI described above (Spilliaert et al., 2006a,b).

Our presented data provide valuable information about the Cl- and S partition between basaltic melt and hydrous fluid and allow estimation of the S content in the melt and the oxygen fugacity in the system, if the S/Cl ratio of the coexisting fluid is known (considering fluid-melt equilibrium and aphyric conditions). Since our experimental pressure (100 and 200 MPa) is very close to P-conditions of Mt.Etna's magma storage (~250 MPa) (e.g., Métrich et al., 2004) and P at the onset of initial S degassing (~140 MPa) (Spilliaert et al., 2006b), we compared the S/Cl ratios of our fluids with the in situ measured S/Cl- ratios of emitted gases at Mt.Etna (Aiuppa et al., 2004) and compared the S concentration of our coexisting melts to the S contents of the primitive and the more evolved OL-MI of Mt.Etna.

The experimental T (1050°C) is slightly lower than temperatures estimated for the primitive Mt. Etnean melts (1100-1150°C) (Clocchiatti & Métrich, 1984; Métrich 1985; Archambault & Tanguy, 1976; Kamenetzkiy et al., 1986; Métrich & Clochiatti, 1989). However, the OL-saturated data (OL-melt equilibrium) (Chapter I) indicate that the temperature of Mt.Etna's S-rich magma containing ~5.5 wt.% MgO, might be somewhat lower (~1025°C) and the more evolved OL-MI containing less than 5 wt.% MgO indicate to be in equilibrium with OL at T about <1025°C (Fig.15, Chapter I). The range of our investigated fO_2 of ~FMQ+0.5 (sulfide-dominated system) and ~FMQ+2 to ~FMQ+4 (sulfate-dominated system) accounts for the relatively high oxidation-state of Mt.Etna magma determined to be FMQ+1 ($S^{6+}/\Sigma S$ ratio of $\sim 0.44 \pm 0.07$) and to the high fO_2 -dependence on the sulfur solubility (and S partitioning) at fO_2 FMQ+1 (e.g., Carroll & Rutherford, 1985, 1987; Luhr, 1990; Jugo et al., 2005a, 2009, *subm.*; Parat et al., 2008; Botcharnikov, *subm.*).

Fig.24 illustrates the experimentally constrained correlation between the S/Cl ratio in the fluid and the S content in the coexisting melts containing $\sim 0.15 \pm 0.02$ and 0.5 ± 0.1 wt.% Cl for the sulfate-dominated system (~FMQ+2 to ~FMQ+4) and ~ 0.05 -2.24 wt.% Cl for the FeS-saturated melts (FMQ+0.5).

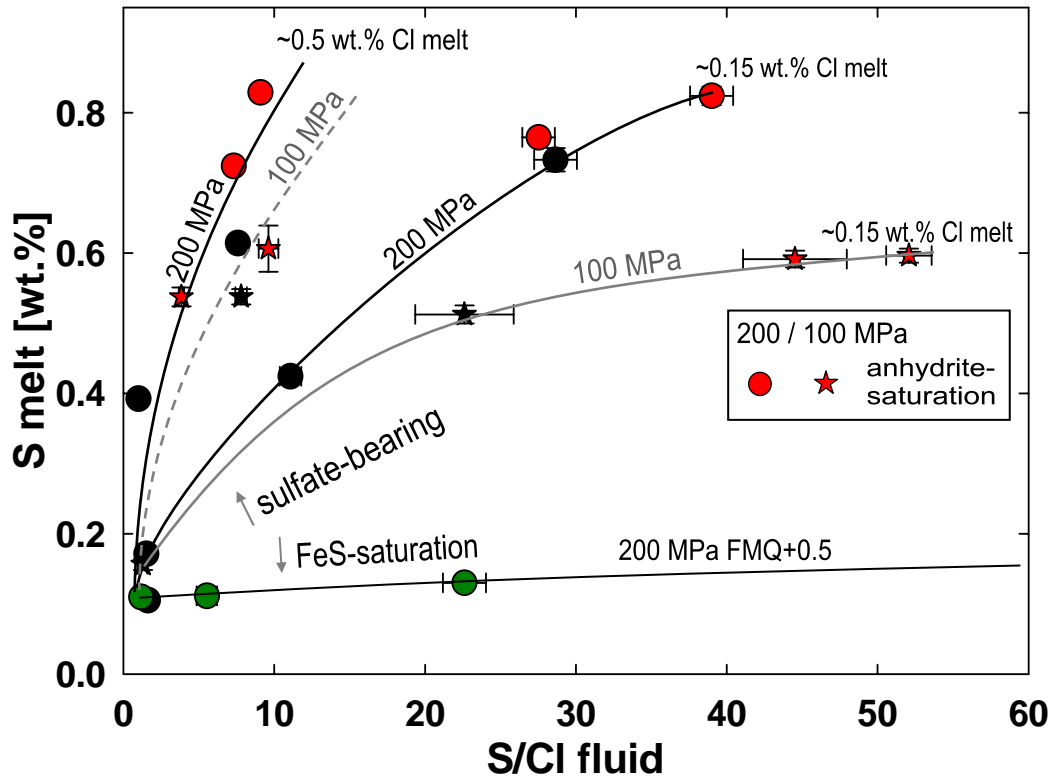


Fig.24: Correlation between the S/Cl ratio in the fluid and the S concentration in the coexisting melts containing ~0.15 and ~0.5 wt.% Cl, comparable to Cl-concentrations of natural Mt Etnean melts (0.15-0.26 wt.% Cl) Spilliaert et al. (2006a,b). The grey arrows illustrate the observed differences in S/Cl-fluid and S melt between the FeS-saturated basaltic melts in a sulfide-dominated system at ~FMQ+0.5 (green dots) and the sulfate-dominated basaltic melts (black symbols) including anhydrite-saturated data (red symbols). The curves are guiding-lines to the observed trends for each series at fixed Cl melt and constant P.

The here presented data demonstrate, that in the range of investigated system compositions the natural fluid S/Cl ratios (0.2-7) and the natural S contents of the primitive and slightly evolved melts (0.27-0.35 and 0.13-0.18 wt.% S, respectively) have been experimentally reproduced only in the sulfate-bearing systems (at ~0.15-0.5 wt.% Cl in the melt). With respect to the H₂O contents of the natural OL-MI, our data primarily account for the primitive juvenile melts, containing similar amounts of H₂O than the experimental data at 100 MPa (2.72-4.01 wt.% H₂O, Table 8, Fig.19). However, Fig.24 shows the trend of decreasing S content in the melt with decreasing S/Cl-fluid ratio in the fluid as supposed by Aiuppa et al. (2004, 2009) and Spilliaert et al. (2006a, 2006b). In Fig.25 the obtained correlation between the S/Cl ratio in the

fluid and the S concentration of the coexisting melt are schematically drawn in the field of interest.

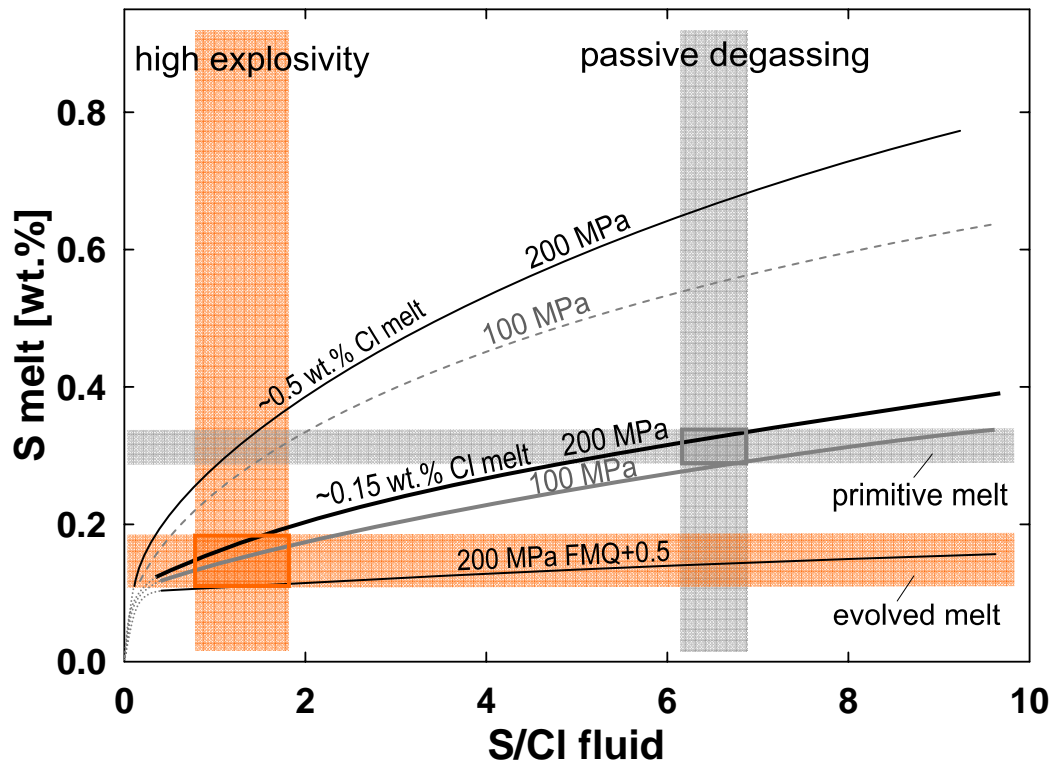


Fig.25: Similar diagram as shown in Fig.24, magnified to the field of interest by taking the natural in situ measured S/Cl ratios in volcanic gases at Mt.Etna's 2002-2003 eruption by Aiuppa et al. (2004) into account (the light red coloured vertical bar illustrating S/Cl ratios of $\sim 0.4-2$ correlates to high volcanic explosivity; S/Cl ratios of $\sim 6-7$ correlate to passive degassing stages as indicated by the gray vertical bar). The S content of Mt.Etna's olivine melt inclusions (OL-MI) and glass embayments is shown by the horizontal bars. The gray horizontal bar represents primitive volatile-rich OL-MI and the red horizontal bar represents more evolved OL-MI and glass embayments. The gray and the red square illustrated the supposed correlation between the S/Cl ratio in the fluid and the S content in the melt at passive degassing and stages of high explosivity (e.g. Métrich et al., 1993, Aiuppa et al., 2004, Spilliaert et al., 2006a, 2006b). Shown curves are derived from interpolation of data plotted in Fig.24.

The experiments show that at a S/Cl ratio in the fluid of ~ 7 (representing stages of passive degassing) is obtained at ~ 0.25 and 0.3 wt.% S for 100 and 200 MPa, respectively and 0.15 wt.% Cl in the melt or slightly above ~ 0.5 and 0.6 wt.% S for 100 and 200 MPa, respectively and ~ 0.5 wt.% Cl in the melt. Our estimated required melt S contents (at 200 MPa and 0.15 wt.% Cl dissolved in the melt) completely coincide with the S concentration of

Mt. Etna's primitive volatile-rich, S-rich melts. Taking the estimated S solubility of Etna basalt at 1050°C and FMQ+1 of ~0.35 wt.% S into account (Chapter I), we conclude primitive Mt. Etna melt containing 0.35 wt.% at a maximum, were close to be sulfur-saturated. However, at sulfur-saturation these melts are expected to condense S-bearing phases at QFM+1, as observed in the more evolved MI, containing \leq ~0.15 wt.% S (e.g., Métrich, 1989; Spilliaert et al., 2006b). According to data of Spilliaert et al. (2006a) Mt. Etna S-rich melts become S-depleted, if their water content become less than 2 wt.% H₂O.

Our results for sulfur partitioning show that at fluid saturated conditions, and 0.3-0.4 wt.% S dissolved in the melt (and Cl melt between 0.15 and 0.5 wt.%), sulfur partitions into the fluid in a larger extend at 100 MPa (K_d^S ~12-16) compared to 200 MPa (K_d^S ~2-5). This indicates that the onset of S degassing at P ~140 MPa (Spilliaert et al., 2006b) might be caused by accompanied degassing of water. Therefore, these melts are expected to release S-rich volatiles at fluid saturated conditions, in particular, if P decreases (during magma ascent).

Another possibility for S degassing with decreasing P at water saturated conditions may be due to the observed positive effect of water on S-solubility as indicated by our experiments and those of Luhr (1990) and Moune et al. (2008). Our data show that decreasing S/Cl ratios represent degassing of S-depleted more evolved magma. However, the presented model does not account for fractional crystallisation, which is expected to enforce the degassing of sulfur (without formation of S-bearing solid phase), because (1) the sulfur/melt-proportion increases and (2) with increasing melt differentiation the S solubility decreases. Experimental constraints of the crystallization path of Mt. Etna's primitive juvenile magma showed that at T ~1060°C and P down to ~27 MPa (~1.6 wt.% H₂O in the melt, water-saturated conditions) the residual melt fraction was about 0.5 and the composition of the residual melts were comparable to that of the primitive starting glass (except the product melts were depleted in about 45 rel.% MgO, containing ~4 wt.% MgO vs. 7.7 wt.% MgO in the starting glass) (Métrich & Rutherford, 1998). The composition of the more evolved OL-MI and OL-glass embayments significantly differ

from that of the primitive OL-MI (mainly in higher K_2O and lower CaO and MgO contents), assuming the S solubility in the more evolved melts should be lower than in the primitive ones. Although the dynamics of volcanic degassing are complex (e.g., Sparks, 2003; Corsaro & Pompilio, 2004) our data can be applied accurately to the volcanic system of Mt. Etna and probably to other basaltic relatively oxidized S-rich volcanic systems.

6. Conclusions

The results of our S- and Cl partitioning experiments at $1050^\circ C$ between aqueous fluid and basaltic melt at 100 and 200 MPa (FMQ+0.5 to FMQ+4) and dacitic melt at 200 MPa (FMQ+0.5) show a non-linear partitioning-behavior of chlorine and at $fO_2 \geq FMQ+2$ a non-linear partitioning-behavior of sulfur. In a Cl-free/poor system the sulfide saturation at FMQ+0.5 was determined to be 0.04 wt.% S in the dacitic melts and to be in the range of 0.09 ± 0.01 to 0.13 ± 0.01 wt.% S in the basaltic melts. The S content at anhydrite-saturation in the Cl-poor basaltic melt was 0.85 ± 0.02 wt.% S at FMQ+2 and 0.74 ± 0.01 wt.% S at FMQ+4 at 200 MPa and 0.60 ± 0.01 wt.% S at FMQ+2.5 and 0.64 ± 0.01 wt.% S at FMQ+4 at 100 MPa.

The maximum chlorine concentration, observed at highest Cl content in the system (~ 3 - 3.6 wt.% Cl) in the sulfate-poor and S-free melts was determined to be 2.26 ± 0.02 wt.% Cl at 200 MPa and 2.20 ± 0.04 wt.% Cl at 100 MPa in the basaltic melts and 1.42 ± 0.03 wt.% in the dacitic melts (at 200 MPa).

Four most important observations have been reported. (1) Mutual effects of chlorine and sulfur were only observed in the sulfate-dominated systems ($fO_2 \geq FMQ+2$). (2) The addition of chlorine reduces the S content at anhydrite-saturation for a maximum of about 23-27 rel.%, observed at FMQ+4 for both investigated pressures. (3) The addition of chlorine to the sulfate-dominated systems increases the extraction of cations from the melt (mainly Ca^{2+} and to a minor

extend Na^+ and K^+) into the fluid, which can be explained by the increased solubility of cation-sulfates mainly CaSO_4 in Cl-bearing aqueous fluids as quantified by Newton & Manning (2005) and Webster et al. (2009b). The partitioning-behavior of chlorine is significantly affected by the increased cation-load to the fluid in the sulfate-bearing systems, leading to an increase of fluid complexity, which is supposed to influence the chlorine activity in the fluid. (4) The effect of chlorine on the partitioning-behavior of sulfur can be explained by decreasing S concentrations in the melt, due to the Cl enforced dissolution of sulfates from the melt (mainly CaSO_4) into the fluid. This effect is most pronounced at low S contents in the system, where mainly all sulfur dissolves in the fluid, resulting in a dramatic increase of K_d^S (~10 to 100-fold increase) compared to Cl-poor systems containing comparably amounts of sulfur.

The results allow to estimate the S concentration in basaltic melts and to constrain the oxygen fugacity in the system, if the Cl content in the melt and the S/Cl ratio of the coexisting fluid is known. Applied to the natural system of Mt. Etna, the estimated sulfur concentration is 0.3 wt.% S for a melt being in equilibrium with a fluid representing passive degassing stages of Mt. Etna's 2002-2003 eruption (S/Cl ratio of ~7) (Aiuppa et al., 2004), which is completely comparable to the S contents of primitive S-rich melts ranging between ~0.27-0.35 wt.% S (Spilliaert et al., 2006a, 2006b). Thus, the results confirm the assumption that the S-rich volatiles emitted during passive degassing stages originate from primitive S-rich magma (e.g., Aiuppa et al., 2002, 2004, 2008; Spilliaert et al., 2006a, 2006b). Calculating the S concentration in the melt, responsible for lower S/Cl fluid ratios observed at increasing volcanic explosivity (Aiuppa et al., 2004) yielded values of about 0.1-0.2 wt.% S and thus being similar to the S contents of more evolved S-depleted melts (e.g., Métrich et al., 2004; Spilliaert et al., 2006a, 2006b). Although our data do not account for magma crystallization and the dynamics of degassing processes, the estimated sulfur concentrations are surprisingly accurate and can be therefore applied to other relatively oxidized S-rich basaltic volcanic systems.

References

- Aiuppa, A., Baker, D. R., Webster, J. D. (2009) Halogens in volcanic systems. *Chem. Geol.* 263, 1-18.
- Aiuppa, A., Federico, C., Giudice, G., Gurrieri, S., Liuzzo, M., Shinohara, H., Favara, R., Valenza, M. (2006) Rates of carbon dioxide plume degassing from Mount Etna volcano. *J. Geophys. Res.* 111, B09207. doi:10.1029/2006JB004307.
- Aiuppa, A., Federico, C., Giudice, G., Gurrieri, S., Paonita, A., Valenza, M. (2004) Plume chemistry provides insights into mechanisms of sulfur and halogen degassing in basaltic volcanoes. *Earth Planet. Sci. Lett.* 222, 469-483.
- Aiuppa, A., Federico, C., Paonita, A., Pecoraino, G., Valenza, M. (2002) S, Cl and F degassing as an indicator of volcanic dynamics: the 2001 eruption of Mount Etna. *Geophys. Res. Lett.* 29, 54-1 - 54-4. doi:10.1029/2002GL015032.
- Aiuppa, A., G. Giudice, S. Gurrieri, M. Liuzzo, M. Burton, T. Caltabiano, A. J. S. McGonigle, G. Salerno, H. Shinohara, and M. Valenza (2008) Total volatile flux from Mount Etna. *Geophys. Res. Lett.* 35, L24302. doi:10.1029/2008GL035871.
- Aiuppa, A., Moretti, R., Federico, C., Giudice, G., Gurrieri, S., Liuzzo, M., Papale, P., Shinohara, H., Valenza, M. (2007) Forecasting Etna eruptions by real-time observation of volcanic gas composition. *Geology* 35, 1115-1118.
- Allard, P. (1997) Endogenous magma degassing and storage at Mount Etna. *Geophys. Res. Lett.* 24, 2219-2222.
- Alletti, M., Baker, D. R., Scaillet, B., Aiuppa, A., Moretti, R., Ottolini, L. (2009) Chlorine partitioning between a basaltic melt and H₂O–CO₂ fluids at Mount Etna. *Chem. Geol.* 263, 37-50.
- Andronico, D., Branca, S., Calvari, S., Burton, M., Caltabiano, T., Corsaro, R. A., Del Carlo, P., Garfi, G., Lodato, L., Miraglia, L., Murè, F., Neri, M., Pecora, E., Pompilio, M., Salerno, G., Spampinato, L. (2005) A multi-disciplinary study of the 2002-03 Etna eruption: insights into a complex plumbing system. *Bull. Volcanol.* 67, 314-330.
- Archambault, C. & Tanguy, J. C. (1976) Comparative temperature measurements on Mount Etna Lavas: Problems and Techniques. *J. Volcanol. Geotherm. Res.* 1, 113-125

- Ballhaus, C., Bockrath, C., Wohlgemuth-Ueberwasser, C., Laurenz, V., Berndt, J. (2006) Fractionation of the noble metals by physical processes. *Contrib. Mineral. Petrol.* 152, 667-684.
- Behrens, H. (1995) Determination of water solubilities in highviscosity melts: an experimental study of NaAlSi₃O₈ and KAlSi₃O₈ melts. *Eur. J. Mineral.* 7, 905-920.
- Berndt, J., Liebske, C., Holtz, F., Freise, M., Nowak, M., Ziegenbein, D., Hurkuck, W., Koepke, J. (2002). A combined rapid-quench and H₂-membrane setup for internally heated pressure vessels: Description and application for water solubility in basaltic melts. *Am. Min.* 87, 1717-1726.
- Bischoff, J. L. & Pitzer, K. S. (1989) Liquid–vapor relations for the system NaCl–H₂O: summary of the P–T–x surface from 300°C to 500°C. *Am. J. Sci.* 289, 217-248.
- Bischoff, J. L. & Rosenbauer, R. J. (1985) An empirical equation of state for hydrothermal seawater (3.2 percent NaCl). *Am. J. Sci.* 285, 725-763.
- Bischoff, J. L. & Rosenbauer, R. J. (1988) Liquid–vapor relations in the critical region of the system NaCl–H₂O from 380°C to 415°C: a refined determination of the critical point and two-phase boundary of seawater. *Geochim. Cosmochim. Acta.* 52, 2121-2126.
- Bischoff, J. L., Rosenbauer, R. J., Fournier, R. O. (1996) The generation of HCl in the system CaCl₂-H₂O: vapor–liquid relations from 380°C-500°C. *Geochim. Cosmochim. Acta.* 60, 7-16.
- Bockrath, C., Ballhaus, C., Holzheid, A. (2004) Stabilities of laurite RuS₂ and monosulfide liquid solution at magmatic temperature. *Chem. Geol.* 208, 265-271.
- Bodnar, R. J., Burnham, C. W., Sterner, S. M. (1985) Synthetic fluid inclusions in natural quartz. III. Determination of phase equilibrium properties in the system H₂O-NaCl to 1000 °C and 1500 bars. *Geochim. Cosmochim. Acta* 49, 1861-1873.
- Bortnikov, N. S. & Vikent'ev, I. V. (2005) Modern base metal sulphide mineral formation in the world ocean. *Geol. Ore Deposits* 47, 13-44.
- Botcharnikov, R. E., Almeev, R. R., Koepke, J., Holtz, F. (2008) Phase relations and liquid lines of descent in hydrous ferrobasalt – implications for the Skaergaard intrusion and Columbia river flood basalts. *J Petrol.* 49, 1687-1727.
- Botcharnikov, R. E., Behrens, H., Holtz, F., Koepke, J., Sato, H. (2004) Sulfur and chlorine solubility in Mt. Unzen rhyodacitic melt at 850°C and 200 MPa. *Chem. Geol.* 213, 207-225.

- Botcharnikov, R. E., Holtz, F., Behrens, H. (2007) The effect of CO₂ on the solubility of H₂O-Cl fluids in andesitic melt. *Eur. J. Mineral.* 19, 671-680.
- Botcharnikov, R. E., Linnen, R. L., Holtz, F. (2010) Solubility of Au in Cl- and S-bearing hydrous silicate melts. *Geochim. Cosmochim. Acta* 74, 2396-2411.
- Botcharnikov, R. E., Linnen, R. L., Wilke, M., Holtz, F., Jugo, P. J., Berndt, J. (subm.) Magmatic extraction of noble metals from the Earth's mantle. *Nature Geoscience*.
- Brenan, J. M. (2008) Re-Os fractionation by sulfide melt-silicate melt partitioning: A new spin. *Chem. Geol.* 248, 140-165.
- Brey, G. P., Bulatov, V. K., Gurnis, A. V., Lahaye, Y. (2008) Experimental melting of Carbonated Peridotite at 6-10 GPa. *J. Petrol.* 49, 797-821.
- Candela, P. A., Piccoli, P. M. (1995) Model ore-metal partitioning from melts into vapor and vapor/brine mixtures. In: Thompson, J.F.H. (Ed.), *Magma, Fluids, and Ore Deposits*, Vol. 23. Min. Ass. Canada, 101-127.
- Carroll, M. R. & Rutherford, M. J. (1985) Sulfide and sulfate saturation in hydrous silicate melts. *J. Geophys. Res.* 90, 601-612.
- Carroll, M. R. & Rutherford, M. J. (1987) The stability of igneous Anhydrite: experimental results and implications for sulfur behavior in the 1982 El Chichon trachyandesite and other evolved magmas. *J. Petrol.* 28, 781-801
- Carroll, M. R. & Rutherford, M. J. (1988). Sulfur speciation in hydrous experimental glasses of varying oxidation state: results from measured wavelength shifts of sulfur X-rays. *Am. Min.* 73, 845-849.
- Carroll M. R., Webster J. D. (1994) Solubilities of sulfur, noble gases, nitrogen, chlorine, and fluorine in magmas. In: Carroll, M. R., Holloway, J. R. (eds) *Volatiles in magmas*. Mineral Society of America, Washington DC, 231-271.
- Cervantes, P. & Wallace, P. (2003) Magma degassing and basaltic eruption styles: a case study of 2000 year BP Xitle volcano in central Mexico. *J. Volcanol. Geotherm. Res.* 120, 249-270.
- Chevychelov, V. Y., Botcharnikov, R. E., Holtz, F. (2008a) Partitioning of Cl and F between fluid and hydrous phonolitic melt of Mt. Vesuvius at ≈850–1000°C and 200 MPa. *Chem. Geol.* 256, 172-184.

- Chevychelov, V. Y., Botcharnikov, R. E., Holtz, F. (2008b) Experimental study of fluorine and chlorine partitioning between fluid and subalkaline basaltic melt. *Doklady Earth Sciences*, 422, 1089-1092.
- Chou, I.-M. (1987) Phase relations in the system NaCl–KCl–H₂O. III. Solubilities of halite in vapor-saturated liquids above 445°C and redetermination of phase equilibrium properties in the system NaCl–H₂O to 1000°C and 1500 bars. *Geochim. Cosmochim. Acta* 51, 1965-1975.
- Chou, I.-M., Sterner, S. M., Pitzer K. S. (1992) Phase relations in the system NaCl–KCl–H₂O: IV. Differential thermal analysis of the sylvite liquidus in the KCl–H₂O binary, the liquidus in the NaCl–KCl–H₂O ternary, and the solidus in the NaCl–KCl binary to 2 kb pressure, and a summary of experimental data for thermodynamic-PTX analysis of solid–liquid equilibria at elevated P–T conditions. *Geochim. Cosmochim. Acta* 56, 2281-2293.
- Clocchiatti R., Condomines M., Guenot N., Tanguy, J. C. (2004) Magma changes at Mount Etna: the 2001 and 2002-2003 eruptions. *Earth Planet. Sci. Lett.* 226, 397-414.
- Clocchiatti, R. & Métrich, N. (1984) Témoignages de la contamination dans les produits des éruptions explosives des Mts. Silvestri (1892) et Mts. Rossi (1669), Mt. Etna. *Bull. Volcanol.* 47/2, 909-928.
- Clemente, B., Scaillet, B., Pichavant, M. (2004) The solubility of sulphur in rhyolitic melts. *J. Petrol.* 45, 2171-2196.
- Corsaro, R. A., Métrich, N., Allard, P., Andronico, D., Miraglia, L., Fourmentaux, C. (2009) The 1974 flank eruption of mount etna: an archetype for deep dike-fed eruptions at basaltic volcanoes and a milestone in etna's recent history. *J. Geophys. Res.* 114-7, B07204. doi:10.1029/2008JB006013.
- Corsaro, R. A., Miraglia, L., Pompilio, M. (2007), Petrologic evidence of a complex plumbing system feeding the July August 2001 eruption of Mt. Etna, Sicily, Italy. *Bull. Volcanol.* 69, 401-421.
- Corsaro, R. A. & Pompilio, M. (2004) Magma dynamics in the shallow plumbing system of Mt. Etna as recorded by compositional variations in volcanics of recent summit activity (1995-1999). *J. Volcanol. Geotherm. Res.* 137, 55- 71.
- De Hoog, J. C. M., Koetsier, G. W., Bronto, S., Sriwana, T., van Vergen, M. J. (2001) Sulfur and chlorine degassing from primitive arc magmas: temporal changes during the 1982-1983 eruptions of Galunggung (West Java, Indonesia) *J. Volcanol. Geotherm. Res.* 108, 55-83.

- Devine, J. D. & Gardner, J. E. (1995) Comparison of microanalytical methods for estimating H₂O contents of silicic volcanic glasses. *Am. Min.* 80, 319-328.
- Devine, J. D., Sigurdsson, H., Davis, A. N., Self, S. (1984) Estimates of sulphur and chlorine yield to the atmosphere from volcanic eruptions and potential climatic effects. *J. Geophys. Res.* 89, 6309-6325.
- Duan, Z., Moller, N., Weare, J. H. (2006) A high temperature equation of state for the H₂O-CaCl₂ and H₂O-MgCl₂ systems. *Geochim. Cosmochim. Acta* 70, 3765–3777.
- Di Liberto, V., Nuccio, P., Paonita, A. (2002) Genesis of chlorine and sulphur in fumarolic emissions at Vulcano island (Italy): assessment of pH and redox conditions in the hydrothermal system. *J. Volcanol. Geotherm. Res.* 116, 137-150.
- Driesner, T. & Heinrich, C. A. (2007a) The system H₂O–NaCl. Part I: Correlation formulae for phase relations in temperature–pressure–composition space from 0 to 1000 °C, 0 to 5000 bar, and 0 to 1 X_{NaCl}. *Geochim. Cosmochim. Acta* 71, 4880-4901.
- Driesner, T. & Heinrich, C. A. (2007b) The system H₂O–NaCl. Part II: Correlations for molar volume, enthalpy, and isobaric heat capacity from 0 to 1000 °C, 1 to 5000 bar, and 0 to 1 X_{NaCl}. *Geochim. Cosmochim. Acta* 71, 4902-4919.
- Ehlers, K., Grove, T. L., Sisson, T. W., Recca, S. I., Zervas, D. A. (1992) The effect of oxygen fugacity on the partitioning of nickel and cobalt between olivine, silicate melt, and metal. *Geochim. Cosmochim. Acta* 56, 3733-3743.
- Edmonds, M., Pyle, D., Oppenheimer, C. (2001) A model for degassing at the Soufrière Hills volcano, Montserrat, West Indies, based on geochemical data. *Earth Planet. Sci. Lett.* 186, 159-173.
- Edmonds, M., Pyle, D., Oppenheimer, C. (2002) HCl emissions at Soufrière Hills Volcano, Montserrat, West Indies, during a second phase of dome building: November 1999 to October 2000. *Bull. Volcanol.* 64, 21-30.
- Feig, S. T., Koepke, J., Snow, J. E. (2006) Effect of water on tholeiitic basalt phase equilibria: an experimental study under oxidizing conditions. *Contrib. Mineral. Petrol.* 152, 611-638.
- Feig, S. T., Koepke, J., Snow, J. E. (2010) Effect of oxygen fugacity and water on phase equilibria of a hydrous tholeiitic basalt. *Contrib. Mineral. Petrol.* DOI: 10.1007/s00410-010-0493-3.

- Ferlito, C., Viccaro, M., Cristofolini, R. (2008) Volatile-induced magma differentiation in the plumbing system of Mt. Etna volcano (Italy): evidence from glass in tephra of the 2001 eruption. *Bull. Volcanol.* 70, 455-473.
- Ferlito, C., Viccaro, M., Cristofolini, R. (2009) Volatile-rich magma injection into the feeding system during the 2001 eruption of Mt. Etna (Italy): its role on explosive activity and change in rheology of lavas. *Bull. Volcanol.* 71, 575-587.
- Gaetani, G. A. & Grove, T. L. (1998) The influence of water on melting of mantle peridotite. *Contrib. Mineral. Petrol.* 131, 323-346.
- Gaetani, A. G. & Grove, T. L. (1999) Wetting of mantle olivine by sulfide melt: implications for Re/Os ratios in mantle peridotite and late-stage core formation. *Earth Planet. Sci. Lett.* 169, 147-163.
- Gaetani, G. A. & Watson, E. B. (2002) Modeling the major-element evolution of olivine-hosted melt inclusions. *Chem. Geol.* 183, 25-41.
- Graf, H.-F., Feichter, J., Langmann, B. (1997) Volcanic sulfur emissions: estimates of source strength and its contribution to the global sulfate distribution. *J. Geophys. Res.* D102, 10727-10728.
- Grainger, R. & Highwood, E. (2003) Changes in stratospheric composition, chemistry, radiation and climate caused by volcanic eruptions. In: *Volcanic Degassing*, Special publication of Royal Geological Society 329-347.
- Gunter, W. D., Chou, I.-M., Girsberger, S. (1983) Phase relations in the system NaCl–KCl–H₂O. II. Differential thermal analysis of the halite liquidus in the NaCl–H₂O binary above 450°C. *Geochim. Cosmochim. Acta* 47, 863-873.
- Hammer, J. E. & Rutherford, M. J. (2003) Petrologic indicators of preeruption magma dynamics. *Geology* 31, 79-82.
- Haughton, D. R., Roeder P. L., Skinner, B. J. (1974) Solubility of sulfur in mafic magmas. *Econ. Geol.* 69, 451-467.
- Heinrich, C. A. (2005) The physical and chemical evolution of low salinity magmatic fluids at the porphyry to epithermal transition: a thermodynamic study. *Miner. Deposita* 39, 864-889.
- Heinrich, C. A. (2007) Fluid-fluid interactions in magmatic-hydrothermal ore formation. *Rev. Mineral. Geochem.* 65, 363-387.

- Holloway, J. R. (1971) Internally heated pressure vessels. In: Ulmer, G.C., Ed., *Research techniques for high temperature and pressure*, 217-258. Springer Verlag, New York.
- Holloway, J. R., Pan, V., Gudmundsson, G. (1992). High-pressure fluid-absent melting experiments in the presence of graphite: oxygen fugacity, ferric/ferrous ratio and dissolved CO₂. *Eur. J. Mineral.* 4, 105-114.
- Holzheid, A. & Grove, L. (2002) Sulfur saturation limits in silicate melts and their implications for core formation scenarios for terrestrial planets. *Am. Min.* 87, 227-237.
- Jugo, P. J. (2009) Sulfur content at sulfide saturation in oxidized magmas. *Geology* 37, 415-418.
- Jugo, P. J., Luth, R. W., Richards, J. P. (2005a) An Experimental Study of the Sulfur Content in Basaltic Melts Saturated with Immiscible Sulfide or Sulfate Liquids at 1300 °C and 1.0 GPa. *J. Petrol.* 46, 783-798.
- Jugo, P. J., Luth, R. W., Richards, J. P. (2005b) Experimental Data on the Speciation of Sulfur as a Function of Oxygen Fugacity in Basaltic Melts: *Geochim. Cosmochim. Acta* 69, 497-503.
- Jugo, P. J., Wilke, M., Botcharnikov, R. E. (subm.) Sulfur K-edge XANES analysis of natural and synthetic basaltic glasses: Implications for S speciation and S content as function of oxygen fugacity. submitted.
- Kamenetskiy, V., Sobolev, A., Clocchiatti, R., Métrich, N. (1986) Première estimation de la teneur en eau du magma de l'Etna à partir des inclusions fluides et vitreuses. *CR Acad. Sci. Paris.* 302 II, 1069-1074.
- Katsura, T., Nagashima, S. (1974) Solubility of sulphur in some magmas at 1 atmosphere. *Geochim. Cosmochim. Acta* 38, 517-531.
- Keppler, H. (2010) The distribution of sulfur between haplogranitic melts and aqueous fluids. *Geochim. Cosmochim. Acta* 74, 645-660.
- Koepke, J. (1997) Analyse von wasserhaltigen silikatischen Gläsern mit der Mikrosonde: Wassergehalte und Alkaliverluste. *Berichte der Deutschen Mineralogischen Gesellschaft, Beiheft in Eur. J. Mineral.* 9, 200.
- Kravchuk, I. F., Keppler, H. (1994) Distribution of chloride between aqueous fluids and felsic melts at 2 kbar and 800°C. *Eur. J. Mineral.* 6, 913-923.
- Kress, V. C., Carmichael, I. S. E. (1991) The compressibility of silicate liquids containing Fe₂O₃ and the effect of composition, temperature, oxygen fugacity and pressure on their redox states. *Contrib. Mineral. Petrol.* 108, 82-92.

- Legrand, M. & Delmas, R. J. (1987) A 220-year continuous record of volcanic H₂SO₄ in the Antarctic ice sheet. *Nature* 327, 671-676.
- Li, C. & Ripley, E. M. (2009). Sulfur Contents at Sulfide-Liquid or anhydrite Saturation in Silicate Melts: Empirical Equations and Example Applications. *Econ. Geol.* 104, 405-412.
- Liu, Y., Samaha, N.-T., and Baker, D. R. (2007). Sulfur concentration at sulfide saturation (SCSS) in magmatic silicate melts. *Geochim. Cosmochim. Acta* 71, 1783-1799.
- Luhr, J. F. (1990) Experimental Phase-Relations of Water-Saturated and Sulfur-Saturated Arc Magmas and the 1982 Eruptions of El Chichon Volcano. *J. Petrol.* 31, 1071-1114.
- Mandeville, C. W., Carey, S., Sigurdsson, H. (1996) Magma mixing, fractional crystallisation and volatile degassing during the 1883 eruption of Krakatau volcano, Indonesia. *J. Volcanol. Geotherm. Res.* 74, 243-274.
- Mathez, E. A., Webster, J. D. (2005) Partitioning behavior of chlorine and fluorine in the system apatite–silicate melt–fluid. *Geochim. Cosmochim. Acta* 69, 1275-1286.
- Mavrogenes, J. A. & O'Neill, H. S. C. (1999) The relative effects of pressure, temperature and oxygen fugacity on the solubility of sulfide in mafic magmas. *Geochim. Cosmochim. Acta* 63, 1173-1180.
- Métrich, N. (1985) Mécanismes d'évolution à l'origine des roches potassiques d'Italie centrale et méridionale. Exemples du Mt Somma Vesuve, des Champs Phlégréens et de l'île de Ventotène. Thèse Doctorat, Université d'Orsay. *Bull PIRPSEV* 110, 1-130.
- Métrich, N., Allard, P., Spilliaert, N., Andronico, D., Burton, M. (2004) 2001 flank eruption of the alkali and volatile-rich primitive basalt responsible for Mount Etna's evolution in the last three decades. *Earth Planet. Sci. Lett.* 228, 1-17, doi:10.1016/j.epsl.2004.09.036.
- Métrich, N. & Clocchiatti, R. (1989) Melt inclusion investigation of the volatile behaviour in historic alkaline magmas of Etna. *Bull. Volcanol.* 51, 185-198.
- Métrich, N. & Clocchiatti, R. (1996) Sulfur abundance and its speciation in oxidized alkaline melts. *Geochim. Cosmochim. Acta* 60, 4151-4160.
- Métrich, N., Clocchiatti, M., Mosbah, M., Chaussidon, M. (1993) The 1989-1990 activity of Etna magma mingling and ascent of H₂O-Cl-S-rich basaltic magma. Evidence from melt inclusions. *J. Volcanol. Geotherm. Res.* 59, 131-144.
- Métrich, N. & Rutherford, M. J. (1992) Experimental study of chlorine behavior in hydrous silicic melts. *Geochim. Cosmochim. Acta* 56, 607-616.

- Métrich, N. & Rutherford, M. J. (1998) Low pressure crystallization paths of H₂O saturated basaltic-hawaiitic melts from Mt Etna: implications for open-system degassing volcanoes. *Geochim. Cosmochim. Acta* 62, 1195-1205.
- Moune, S., Gauthier, P. J., Gislason, S. R., Sigmarsson, O. (2006) Trace element degassing and enrichment in the eruptive plume of the 2000 eruption of Hekla volcano, Iceland. *Geochim. Cosmochim. Acta* 70, 461-479.
- Moune, S., Holtz, F., Botcharnikov, R. E. (2009). Sulphur solubility in andesitic to basaltic melts: implications for Hekla volcano. *Contrib. Min. Petrol.* 157, 691-707.
- Mysen, B. O. & Popp, R. K. (1980) Solubility of sulfur in CaMgSi₂O₆ and NaAlSi₃O₈ melts at high pressure and temperature with controlled f_{O_2} and f_{S_2} . *Am. J. Sci.* 280, 78-92.
- Newton, R. C. & Manning, C. E. (2005) Solubility of anhydrite, CaSO₄, in NaCl-H₂O solutions at high pressures and temperatures. *J. Petrol.* 46, 701-716.
- Nicholis, M. G. & Rutherford, M. J. (2006) Vapor/melt partitioning behavior of S and Cl in a C-O gas mixture (abs.). *Lun. Planet. Sci.* XXXVII, 2061.
- Nikolaev, G. S., Borisov, A. A., Ariskin, A. A. (1996) Calculation of the ferric-ferrous ratio in magmatic melts: Testing and additional calibration of empirical equations for various magmatic series. *Geochem. Int.* 34, 641-649.
- O'Neill, H. St. C. & Mavrogenes, J. A. (2002) The sulfide capacity and sulfur content at sulfide saturation of silicate melts at 1400 °C and 1 bar. *J. Petrol.* 43, 1049-1087.
- Ohlhorst, S., Behrens, H., Holtz, F. (2001) Compositional dependence of molar absorptivities of near-infrared OH- and H₂O bands in rhyolitic to basaltic glasses. *Chemical Geol.* 174, 5-20.
- Oppenheimer, C. (2003) Volcanic degassing. In: Rudnick, R. L., Holland, H. D., Turekian, K. K. (Eds.), *The Crust, Treatise on Geochemistry* 3. Elsevier-Pergamon, Oxford, 123-166.
- Oppenheimer, C., Bani, P., Calkins, J. A., Burton, M. R., Sawyer, G. M. (2006) Rapid FTIR sensing of volcanic gases released by Strombolian explosions at Yasur volcano, Vanuatu. *Appl. Phys., B Lasers Opt.* 85, 453-460.
- Parat, F. & Holtz, F. (2005) Sulphur partition coefficient between apatite and rhyolite: the role of bulk S content. *Contrib. Mineral. Petrol.* 150, 643-651.
- Parat, F., Holtz, F., Feig, S. (2008) Pre-eruptive conditions of the Huerto Andesite (Fish Canyon system, San Juan volcanic field, Colorado): Influence of volatiles (C-O-H-S) on phase equilibria and mineral composition. *J. Petrol.* 49, 911-935.

- Partzsch, G. M., Lattard, D., McCammon, C. (2004) Mössbauer spectroscopic determination of $\text{Fe}^{3+}/\text{Fe}^{2+}$ in synthetic basaltic glass: A test of empirical $f\text{O}_2$ equations under superliquidus and subliquidus conditions. *Contrib. Mineral. Petrol.* 147, 565-580.
- Pavlova, G. G. & Borovikov, A. A. (2008) Physicochemical factors of formation of Au-As, Au-Sb, and Ag-Sb deposits. *Geol. Ore Deposits* 50, 433-444.
- Rampino, M. R. & Self, S. (1992) Volcanic Winter and Accelerated Glaciation Following the Toba Super-Eruption. *Nature.* 359, 50-52.
- Roeder, P. L. & Emslie, R. F. (1970) Olivine-liquid equilibrium. *Contrib. Mineral. Petrol.* 29, 275-289.
- Robock, A. (2000) Volcanic eruptions and climate. *Reviews of Geophysics* 38, 191-219.
- Roux, J. & Lefèvre, A. (1992) A fast-quench device for internally heated pressure vessels. *Eur. J. Mineral.* 4, 279-281.
- Scailliet, B., Clemente, B., Evans, B. W., Pichavant, M. (1998) Redox control of sulfur degassing in silicic magmas. *J. Geophys. Res.* 103, 23 937-23 949.
- Scailliet, B. & MacDonald, R. (2006) Experimental and thermodynamic constraints on the sulphur yield of peralkaline and metaluminous silica flood eruption. *J. Petrol.* 47, 1413-1437.
- Schuessler, J. A., Botcharnikov, R. E., Behrens, H., Misiti, V., Freda, C. (2008) Amorphous materials: properties, structure, and durability: oxidation state of iron in hydrous phonotephritic melts. *Am. Min.* 93, 1493-1504.
- Self, S. (2006) The effects and consequences of very large explosive volcanic eruptions *Phil. Trans. R. Soc. A.* 364, 2073-2097 doi:10.1098/rsta.2006.1814
- Self, S. & King, A. J. (1996) Petrology and sulfur and chlorine emissions of the 1963 eruption of Gunung Agung, Bali, Indonesia. *Bull. Volcanol.* 58, 263-285.
- Shinohara, H. (1994) Exsolution of immiscible vapor and liquid phases from a crystallizing silicate melt: Implications for chlorine and metal transport, *Geochim. Cosmochim. Acta* 58, 5215-5221.
- Shinohara, H. (2009) A missing link between volcanic degassing and chloride partitioning experiments. *Chem. Geology* 263, 51-59.
- Shinohara, H., Iiyama, J. T., Matsuo, S. (1989) Partition of chlorine between silicate melt and hydrothermal solutions: I. Partition of NaCl-KCl. *Geochim. Cosmochim. Acta* 53, 2617-2630.

- Signorelli, S. & Carroll, M. R. (2000) Solubility and fluid-melt partitioning of Cl in hydrous phonolitic melts. *Geochim. Cosmochim. Acta* 64, 2851-2862.
- Signorelli, S. & Carroll, M. R. (2001) Experimental constraints on the origin of chlorine emissions at the Soufrière Hills Volcano, Montserrat. *Bull. Volcanol.* 62, 431-440.
- Signorelli, S. & Carroll, M. R. (2002) Experimental study of Cl solubility in hydrous alkaline melts: constraints on the theoretical maximum amount of Cl in trachytic and phonolitic melts. *Contrib. Mineral. Petrol.* 143, 209-218.
- Sisson T. W. (2003). Native gold in a Hawaiian alkalic magma. *Econ. Geol.* 95, 643-648.
- Sparks, R. S. J. (2003) Dynamics of magma degassing. In: Oppenheimer, C., Pyle, D. M., Barclay, J. (Eds.), *Volcanic Degassing: Special Publications*, vol. 123. Geol. Society London, UK. 5-22.
- Spilliaert, N., Allard, P., Métrich, N., Sobolev, A. V. (2006a) Melt inclusion record of the conditions of ascent, degassing and extrusion of volatile-rich alkali basalt during the powerful 2002 flank eruption of Mount Etna (Italy). *J. Geophys. Res.* 111 (B4), art. no. B04203.
- Spillaert, N., Metrich, N., Allard, P. (2006b) S-Cl-F degassing pattern of water rich alkali basalt: modelling and relationship with eruption styles of Mount Etna volcano. *Earth Planet. Sci. Lett.* 248, 772-786.
- Stefansson, A. & Seward, T. M. (2003) Stability of chloridogold (I) complexes in aqueous solutions from 300 to 600°C and from 500 to 1800 bar. *Geochim. Cosmochim. Acta* 67, 4559-4576.
- Stefansson, A. & Seward, T. M. (2004) Gold(I) complexing in aqueous sulphide solutions to 500°C at 500 bar. *Geochim. Cosmochim. Acta* 68, 4121-4143.
- Stelling, J., Botcharnikov, R. E., Beermann, O., Nowak, M. (2008) Solubility of H₂O- and chlorine bearing fluids in basaltic melt of Mount Etna at T=1050-1250°C and P=200 MPa. *Chem. Geol.* 256, 101-109.
- Sterner, S. M., Chou, I.-M., Downs, R. T., Pitzer, K. S. (1992) Phase relations in the system NaCl–KCl–H₂O. V. Thermodynamic PTX analysis of solid–liquid equilibria at high temperatures and pressures. *Geochim. Cosmochim. Acta* 56, 2295-2309.

- Textor, C., Graf, H.-F., Herzog, M., Oberhuber, J. M. (2003) Injection of gases into the stratosphere by explosive volcanic eruptions. *J. Geophys. Res.* 108, 4606. doi:10.1029/2002JD002987. ist nicht zitiert!!!
- Thordarson, Th., Self, S. (2003) Atmospheric and environmental effects of the 1783-1784 Laki eruption: a review and reassessment. *J. Geophys. Res.* 108 (D1), 4011.
- Thordarson, Th., Self, S., Óskarsson, N. (1996) Sulfur, chlorine, and fluorine degassing and atmospheric loading by the 1783-1784 AD Laki (Skaftár Fires) eruption in Iceland. *Bull. Volcanol.* 58, 205-225.
- Toplis, M. J. (2005) The thermodynamics of iron and magnesium partitioning between olivine and liquid: criteria for assessing and predicting equilibrium in natural and experimental systems. *Contrib. Mineral. Petrol.* 149, 22-39.
- Toulmin, P. I. & Barton, P. B. J. (1964) A thermodynamic study of pyrite and pyrrhotite. *Geochimica et Cosmochimica Acta* 28, 641-671.
- Viccaro, M., Carmelo, F., Cristofolini, R. (2008) Complex evolution processes in the upper feeding system of Mt. Etna (Italy) as revealed by the geochemistry of recent lavas. *Per. Mineral.* (2008), 77, 3, 21-42. doi:10.2451/2008PM0017
- Viccaro, M., Ferlito, C., Cortesogno, L., Cristofolini, R., Gaggero, L. (2006) Magma mixing during the 2001 event at Mount Etna (Italy): effects on the eruptive dynamics. *J. Volcanol. Geotherm. Res.* 149, 139-159.
- Wallace, P. J. (2005) Volatiles in subduction zone magmas: concentrations and fluxes based on melt inclusion and volcanic gas data. *J. Volcanol. Geotherm. Res.* 140, 217-240.
- Wallace, P. J. & Carmichael, I. S. E. (1992) Sulfur in basaltic melts. *Geochim. Cosmochim. Acta* 56, 1863-1874.
- Wallace, P. J. & Carmichael, I. S. E. (1994) S-Speciation in Submarine Basaltic Glasses as Determined by Measurements of SK-Alpha X-Ray Wavelength Shifts. *Am. Min.* 79, 161-167.
- Webster, J. D. (1992) Water solubility and chlorine partitioning in Cl-rich granitic systems: Effects of melt composition at 2 kbar and 800°C. *Geochim. Cosmochim. Acta.* 56, 679-687.
- Webster, J. D. & De Vivo, B. (2002) Experimental and modeled solubilities of chlorine in aluminosilicate melts, consequences of magma evolution, and implications for exsolution of hydrous chloride melt at Mt. Somma-Vesuvius. *Am. Min.* 87, 1046-1061.

- Webster, J. D., Kinzler, R. J., Mathiez, E. A. (1999) Chloride and water solubility in basalt and andesite melts and implications for magmatic degassing. *Geochim. Cosmochim. Acta.* 63, 729-738.
- Webster, J. D., Raia, F., DeVivo, B., Rolandi, G. (2001) The behavior of chlorine and sulfur during differentiation of the Mt. Somma-Vesuvius magmatic system. *Mineral. Petrol.* 73, 177-200.
- Webster, J. D., Sintoni, M. F., De Vivo, B. (2009b) The partitioning behavior of Cl, S, and H₂O in aqueous vapor- ± saline-liquid saturated phonolitic and trachytic melts at 200 MPa. *Chem. Geol.* 263, 19-36.
- Webster, J. D., Tappen, C. M., Mandeville, C. W. (2009a) Partitioning behavior of chlorine and fluorine in the system apatite-melt-fluid. II: Felsic silicate systems at 200 MPa. *Geochim. Cosmochim. Acta* 73, 559-581.
- Wendlandt, R. F. (1982) Sulfide saturation of basalt and andesite melts at high pressures and temperatures. *Am. Min.* 67, 877-885.
- Wilke, M., Jugo, P. J., Klimm K., Susini J., Botcharnikov R., Kohn S. C. and Janousch M. (2008) The Origin of S⁴⁺ Detected in Silicate Glasses by XANES. *Am. Min.* 93, 235-240.
- Williams, T. J., Candela, P. A., Piccoli, P. M. (1997) Hydrogen-alkali exchange between silicate melts and two-phase aqueous mixtures: an experimental investigation. *Contrib. Mineral. Petrol.* 128, 114-126.
- Yamashita, S., Kitamura, T., Kusakabe, M. (1997) Infrared spectroscopy of hydrous glasses of arc magma compositions. *Geochem. J.* 31, 169-174.

Appendix

Table A: Chemical composition of experimentally produced olivine

OL										
Run #	0_15_2 red	01_15_2 red	0_05_1	01_02_1	01_05_1	01_10_1	05_05_1	15_05_1	01_15_1 ox	
n	5	2	7	5	7	6	6	4	5	
SiO ₂	40.24 (19)	39.88 (01)	39.65 (21)	39.42 (26)	39.78 (12)	39.19 (33)	40.31 (17)	39.79 (17)	39.70 (22)	
TiO ₂	0.03 (01)	0.03 (01)	0.04 (02)	0.05 (01)	0.04 (01)	0.03 (01)	0.04 (01)	0.04 (01)	0.05 (02)	
Al ₂ O ₃	0.03 (03)	b.d. (01)	b.d. (01)	0.04 (01)	0.04 (02)	b.d. (01)	0.03 (01)	0.03 (01)	0.10 (12)	
FeO _{tot}	13.62 (38)	14.10 (72)	14.49 (31)	15.27 (73)	13.67 (28)	14.33 (55)	12.08 (58)	11.87 (17)	13.08 (25)	
MnO	0.36 (05)	0.36 (06)	0.33 (05)	0.32 (05)	0.30 (05)	0.33 (04)	0.31 (03)	0.24 (08)	0.24 (04)	
MgO	43.90 (55)	43.04 (80)	44.74 (36)	43.98 (81)	45.61 (36)	44.69 (44)	46.83 (48)	47.30 (17)	46.55 (23)	
CaO	0.31 (03)	0.29 (05)	0.30 (03)	0.33 (04)	0.33 (03)	0.28 (03)	0.31 (02)	0.25 (03)	0.29 (04)	
Na ₂ O	b.d.	b.d.	b.d.	b.d.	b.d.	b.d.	b.d.	b.d.	b.d.	
K ₂ O	b.d.	b.d.	b.d.	b.d.	b.d.	b.d.	b.d.	b.d.	b.d.	
Total	98.50 (34)	97.73 (05)	99.61 (51)	99.44 (94)	99.79 (38)	98.90 (44)	99.93 (50)	99.54 (52)	100.05 (30)	
Fo#	85.2 (329)	84.5 (572)	84.6 (246)	83.7 (543)	85.6 (232)	84.8 (406)	87.4 (499)	87.7 (152)	86.4 (205)	
KD ^{Fe/Mg}										
OL-melt	0.28	0.27	0.33	0.36	0.31	0.33	0.30	0.29	0.32	

Notes: n is the number of analyses. Number in parenthesis is 1 σ standard deviation of the mean. FeO_{tot} is the total iron content. Mg# is the Mg-number: molar Mg/(Mg+Fe²⁺) ratio x 100. $K_D^{Fe-Mg}_{OL-melt}$ is the distribution coefficient of Fe and Mg between OL and melt calculated by Roeder & Emslie (1970) ($K_D^{Fe-Mg}_{OL-melt} = X_{FeO}^{OL} * X_{MgO}^{melt} / X_{FeO}^{melt} * X_{MgO}^{OL}$, [molar]).

Table B: Chemical composition of experimentally produced pyroxenes

cpx										
Run #	0_15_2 red	01_15_2 red	0_02_1	0_05_1	01_02_1	01_05_1	05_02_1	05_05_1	15_02_1	0_15_1 red
n	2	6	7	8	6	7	7	6	6	7
SiO ₂	50.27 (08)	50.00 (63)	47.49 (105)	47.51 (73)	47.58 (64)	47.73 (68)	46.92 (38)	46.80 (32)	47.97 (92)	48.28 (94)
TiO ₂	1.43 (09)	1.13 (24)	1.44 (12)	1.38 (14)	1.46 (10)	1.41 (22)	1.60 (10)	1.45 (08)	1.23 (20)	1.46 (20)
Al ₂ O ₃	5.24 (158)	3.79 (100)	7.02 (229)	5.88 (45)	8.57 (315)	9.73 (454)	8.02 (335)	6.74 (118)	5.37 (77)	5.70 (187)
FeO	4.02 (70)	5.06 (78)	7.76 (124)	7.49 (50)	7.52 (27)	7.44 (44)	7.87 (46)	7.75 (44)	7.58 (98)	6.26 (84)
MnO	0.08 (01)	0.14 (02)	0.16 (06)	0.14 (06)	0.12 (03)	0.15 (03)	0.15 (05)	0.18 (05)	0.15 (09)	0.15 (07)
MgO	14.48 (103)	14.62 (68)	12.80 (184)	13.68 (44)	11.97 (244)	10.88 (347)	12.18 (254)	13.33 (83)	14.38 (78)	13.06 (112)
CaO	22.68 (107)	22.83 (62)	21.55 (265)	23.03 (30)	20.41 (375)	18.24 (490)	20.81 (403)	21.74 (121)	22.49 (24)	22.12 (143)
Na ₂ O	0.37 (18)	0.23 (04)	0.50 (22)	0.35 (02)	0.66 (39)	1.03 (69)	0.65 (60)	0.46 (15)	0.34 (03)	0.42 (25)
K ₂ O	0.27 (32)	b.d.	0.25 (42)	0.04 (02)	0.48 (54)	0.73 (70)	0.32 (56)	0.15 (19)	0.06 (02)	0.16 (23)
Total	98.84 (49)	97.80 (33)	98.96 (172)	99.50 (34)	98.77 (171)	97.35 (218)	98.53 (219)	98.60 (102)	99.57 (42)	97.61 (38)
Mg#	86.5	83.7	74.6	76.5	74.0	72.3	73.4	75.4	77.2	78.8

Notes: see Table A.

Table C: Chemical composition of experimentally produced Fe-oxides

spl												
Run #	0_05_2	0_10_2	01_02_2	01_05_2	01_10_2	01_15_2	15_15_2	0_15_2 ox	01_15_2 ox	05_15_2 ox	15_15_2 ox	
n	5	5	6	4	4	6	6	2	7	6	7	7
SiO ₂	0.07 (02)	0.08 (01)	0.09 (11)	0.10 (04)	0.07 (02)	0.06	0.06	0.07 (01)	0.07 (02)	0.06 (02)	0.06 (02)	0.06 (02)
TiO ₂	4.73 (28)	4.68 (22)	5.13 (24)	5.28 (28)	5.45 (11)	3.17	3.17	4.71 (02)	3.18 (06)	3.07 (11)	3.13 (05)	3.13 (05)
Al ₂ O ₃	5.60 (13)	5.74 (06)	5.54 (06)	5.75 (09)	6.01 (12)	7.02	7.02	7.60 (02)	6.41 (12)	6.38 (10)	6.71 (22)	6.71 (22)
FeO _{tot}	76.63 (49)	76.28 (53)	75.90 (63)	75.84 (83)	75.88 (43)	74.12	74.12	70.42 (20)	74.60 (49)	74.13 (239)	74.37 (77)	74.37 (77)
MnO	0.32 (05)	0.32 (06)	0.30 (03)	0.33 (03)	0.26 (05)	0.31	0.31	0.27 (06)	0.34 (06)	0.34 (05)	0.30 (04)	0.30 (04)
MgO	7.00 (10)	6.62 (07)	6.70 (08)	6.58 (06)	6.43 (13)	7.85	7.85	6.61 (07)	8.05 (14)	8.05 (08)	8.00 (13)	8.00 (13)
CaO	b.d	b.d	b.d	b.d	b.d	b.d	b.d	0.02 (0)	b.d	b.d	b.d	b.d
Na ₂ O	b.d	b.d	b.d	b.d	b.d	b.d	b.d	b.d	b.d	b.d	b.d	b.d
K ₂ O	0.06 (07)	0.08 (03)	0.09 (12)	0.09 (09)	0.07 (04)	0.06	0.06	0.08 (02)	0.09 (07)	0.05 (03)	0.08 (03)	0.08 (03)
Total	94.47 (54)	93.84 (56)	93.78 (51)	94.01 (82)	94.20 (45)	92.63	92.63	89.83 (32)	92.77 (42)	92.12 (256)	92.67 (86)	92.67 (86)

Table C: continued

spll												
Run #	30_15_2 ox	0_02_1	0_05_1	0_10_1	01_02_1	01_05_1	01_10_1	01_15_1	05_02_1	05_05_1	05_15_1	
n	4	7	8	6	4	6	6	8	6	4	6	7
SiO ₂	0.10 (03)	0.14 (03)	0.42 (89)	0.06 (02)	0.10	0.53 (91)	0.53 (91)	0.42 (89)	0.06 (02)	0.10	0.53 (91)	0.13 (09)
TiO ₂	3.28 (03)	4.61 (08)	4.45 (11)	3.17 (08)	3.28	3.79 (07)	3.79 (07)	4.45 (11)	3.17 (08)	3.28	3.79 (07)	3.97 (05)
Al ₂ O ₃	7.75 (14)	7.16 (08)	6.99 (27)	7.02 (12)	7.75	7.01 (35)	7.01 (35)	6.99 (27)	7.02 (12)	7.75	7.01 (35)	7.70 (06)
FeO _{tot}	73.37 (50)	73.62 (31)	73.80 (98)	74.12 (95)	73.37	73.65 (130)	73.65 (130)	73.80 (98)	74.12 (95)	73.37	73.65 (130)	73.57 (45)
MnO	0.23 (08)	0.34 (05)	0.34 (08)	0.31 (04)	0.23	0.35 (06)	0.35 (06)	0.34 (08)	0.31 (04)	0.23	0.35 (06)	0.38 (04)
MgO	7.65 (03)	7.60 (10)	7.32 (21)	7.85 (09)	7.65	8.13 (14)	8.13 (14)	7.32 (21)	7.85 (09)	7.65	8.13 (14)	7.82 (10)
CaO	b.d	0.03 (01)	0.04 (06)	b.d	b.d	0.04 (03)	0.04 (03)	0.04 (06)	b.d	b.d	0.04 (03)	0.02 (01)
Na ₂ O	b.d	b.d	b.d	b.d	b.d	b.d	b.d	b.d	b.d	b.d	b.d	b.d
K ₂ O	0.08 (04)	0.26 (05)	0.28 (10)	0.06 (03)	0.08	0.25 (10)	0.25 (10)	0.28 (10)	0.06 (03)	0.08	0.25 (10)	0.21 (06)
Total	92.48 (55)	93.77 (47)	93.69 (73)	92.63 (96)	92.48	93.83 (49)	93.83 (49)	93.69 (73)	92.63 (96)	92.48	93.83 (49)	93.79 (53)

Table C: continued

spl												
Run #	15_02_1	15_05_1	15_15_1	30_02_1	30_05_1	30_15_1	0_15_1 ox	01_15_1 ox	05_15_1 ox	15_15_1 ox	30_15_1 ox	
n	7	6	12	4	7	13	7	7	6	5	7	
SiO ₂	0.21 (14)	0.13 (03)	0.08 (03)	0.07 (01)	0.10	0.02 (02)	0.08 (02)	0.06 (03)	0.10 (02)	0.09 (01)	0.07 (03)	0.08 (02)
TiO ₂	3.66 (03)	3.61 (03)	3.99 (13)	4.12 (03)	3.92	4.12 (28)	4.09 (06)	4.49 (08)	4.09 (07)	4.41 (05)	4.39 (06)	
Al ₂ O ₃	6.95 (05)	6.95 (09)	7.65 (38)	7.70 (10)	8.35	8.08 (08)	8.79 (37)	7.24 (10)	7.75 (11)	7.55 (04)	8.39 (11)	9.15 (11)
FeO _{tot}	73.39 (47)	74.15 (67)	73.81 (68)	72.44 (47)	70.83	68 (68)	71.13 (106)	75.19 (64)	73.62 (59)	74.05 (53)	73.99 (32)	73.17 (18)
MnO	0.32 (05)	0.28 (03)	0.29 (04)	0.32 (04)	0.25	0.03 (03)	0.22 (05)	0.34 (05)	0.36 (06)	0.30 (05)	0.26 (05)	0.24 (04)
MgO	8.30 (10)	8.09 (08)	7.96 (11)	7.85 (07)	7.96	07 (07)	7.56 (21)	7.59 (08)	7.70 (17)	7.66 (08)	7.38 (08)	7.60 (10)
CaO	0.03 (01)	0.03 (01)	b.d	b.d	b.d	b.d	b.d	b.d	b.d	b.d	b.d	b.d
Na ₂ O	b.d	b.d	b.d	b.d	b.d	b.d	b.d	b.d	b.d	b.d	b.d	b.d
K ₂ O	0.29 (03)	0.25 (03)	0.15 (06)	0.09 (02)	0.16	0.05 (05)	0.12 (04)	0.06 (02)	0.10 (06)	0.13 (04)	0.05 (01)	0.08 (06)
Total	93.16 (49)	93.50 (71)	93.95 (73)	92.63 (47)	91.61 (68)	92.03 (118)	94.58 (70)	94.13 (75)	93.89 (60)	94.56 (36)	94.72 (25)	

Notes: see Table A.

Table D: Starting mass relations of experimental runs using AgCl or AgCl-H₂O/HCl as Cl-source

Run #	m	m	m	c Cl	m	m	m	m	bulk	bulk	bulk	X Cl	X H ₂ O
	glass	AgCl	HCl	HCl	H ₂ O	Cl _{added}	Cl _{init.}	Cl _{tot}	Cl	H ₂ O	fluid		
	[mg]	[mg]	[mg]	[wt.%]	[mg]	[mg]	[mg]	[mg]	[wt.%]	[wt.%]	[wt.%]	molar	molar
AH-1	26.13	1.27	-	-	3.24	0.31	0.02	0.33	1.11	10.91	12.03	0.05	0.95
AH-2	29.85	2.75	-	-	2.57	0.68	0.02	0.70	2.11	7.76	9.87	0.12	0.88
A-10	21.13	9.39	-	-	0.00	2.32	0.01	2.34	9.96	-	9.96	1.00	0.00
HCIA 1	32.28	1.60	3.00	20.43	2.39	0.99	0.02	1.01	2.83	6.75	9.58	0.18	0.82
HCIA 2	26.40	2.65	2.86	29.42	2.02	1.47	0.02	1.49	4.98	6.84	11.82	0.27	0.73
HCIA 3	18.02	3.78	1.40	29.42	0.99	1.34	0.01	1.35	6.61	4.92	11.53	0.41	0.59

Notes: m is the mass. c Cl is the concentration of Cl in HCl in wt.%; m Cl_{added} is the mass of Cl contained in the added mass of HCl solution and AgCl; m Cl_{init.} is the mass of Cl in the starting material due to the initial Cl concentration of 0.06 wt.% Cl in the starting glass; m Cl_{tot} is the sum of m Cl_{added} and m Cl_{init.}. Bulk Cl and H₂O is the concentration of Cl and H₂O in wt.%, respectively, taking the Ag-free loaded starting mass into account. Bulk fluid is the total sum of bulk Cl and H₂O in wt.%. X Cl and X H₂O is the molar ratio of Cl and H₂O, respectively in the bulk fluid (defined to be solely composed of the volatile components Cl and H₂O).

Table E: Experimental run conditions and chemical composition of experimental product glasses using AgCl or AgCl-H₂O/HCl as Cl-source (in wt.%)

Run #	n	SiO ₂	TiO ₂	Al ₂ O ₃	FeO _{tot}	MnO	MgO	CaO	Na ₂ O	K ₂ O	P ₂ O ₅	Cl	Total	H ₂ O	A/ CNK
<i>T=1200°C, P=209 MPa, PH₂=8.0 bar, log fO₂=-7.2/FMQ+0.9, 23 h</i>															
AH-1**	20	45.80 (39)	1.72 (07)	15.84 (26)	9.19 (40)	0.15 (09)	5.89 (21)	10.29(32)	3.18 (15)	1.81 (09)	0.58 (01)	1.14 (02)	95.59(74)	4.77**(62)	0.61
AH-2	20	45.12(55)	1.64 (06)	15.53(21)	8.93 (33)	0.19 (10)	5.77 (19)	9.84 (20)	3.22 (29)	1.80 (08)	0.58 (02)	2.08 (03)	94.70(119)	5.63 (06)	0.62
A-10*	17	49.88(51)	1.85 (06)	17.32(24)	6.55 (35)	0.09 (08)	6.11 (19)	9.25 (25)	2.13 (18)	0.83 (08)	0.56 (02)	3.70 (05)	98.28(106)	2.79 (07)	0.82
<i>T=1200°C, P=193 MPa, PH₂=6.9 bar, log fO₂=-7.1/FMQ+1.0, 26 h</i>															
HCIA 1	20	44.78(33)	1.71 (07)	15.49(27)	8.59 (12)	0.14 (08)	5.69 (13)	10.16(45)	3.11 (22)	1.65 (08)	0.57 (02)	2.82 (02)	94.72(65)	5.57 (10)	0.61
HCIA 2	19	45.25(33)	1.71 (06)	15.49(16)	8.42 (41)	0.17 (07)	5.63 (15)	10.04(18)	2.79 (40)	1.40 (09)	0.58 (03)	3.05 (02)	94.53(74)	5.55 (13)	0.64
HCIA 3*	20	45.92(35)	1.68 (04)	15.67(24)	8.33 (42)	0.12 (12)	5.70 (17)	9.76 (28)	2.36 (12)	1.15 (05)	0.59 (01)	3.39 (07)	94.67(51)	5.53 (09)	0.69

Notes: log fO₂ [bar] derives from monitoring of experimental PH₂ (Shaw-membrane), ΔFMQ is log fO₂ [bar] relative to that of the FMQ-buffer reaction; n is the number of analyses. Number in parenthesis is 1 σ standard deviation of the mean. FeO_{tot} is the total iron content. H₂O KFT is the water concentration in the melt determined by Karl-Fischer-Titration; A/CNK is the molar ratio of Al₂O₃/(CaO + Na₂O + K₂O); ** water content determined by "by-difference" –method at EMPA.; **Cl# is set to 1 and # H₂O is set to 0, because the fluid composition could not be determined due to higher amounts of H₂O dissolved in the melt than initially added to the system, indicating that H₂O was generated by reducing the melt (e.g., Fe³⁺ to Fe²⁺) due to equilibration of PH₂ between vessel and sample capsule (see description in the text at §4.6).

Table F: composition of product fluids using AgCl or AgCl-H₂O/HCl as Cl-source and partitioning coefficients of Cl (Kd^{Cl}) and H₂O (Kd^{H₂O}) between fluid and melt (in wt.)

Run #	Cl#	H ₂ O#	Kd'	Kd'
			Cl	H ₂ O
AH-1	0.01 (00)	0.99 (24)	0.6 (2)	20.8 (71)
AH-2	0.03 (00)	0.97 (10)	1.6 (2)	17.2 (26)
A-10*	1.00* (01)	0.00* (00)	27.0 (4)	0.0 (00)
HCIA 1	0.04 (02)	0.96 (56)	1.4 (12)	17.2 (14)
HCIA 2**	0.59 (09)	0.41 (06)	19.5 (41)	7.3 (15)
HCIA 3*	1.00* (03)	0.00* (00)	29.5 (11)	0.00 (00)

Notes: Cl# and H₂O# ist the Cl or H₂O ratio (in wt.) in a simplified single fluid, defined to be solely composed of the volatile components Cl and/or H₂O (detailed description is given in the text). The partitioning coefficient of Cl (Kd^{Cl}) and H₂O (Kd^{H₂O}) is the ratio of weight proportion of Cl or H₂O in the fluid and the weight proportion of Cl or H₂O in the melt, respectively. The meaning of the signatures "*" and "**" can be taken from Table E.

Lebenslauf

Persönliche Daten

Name: Beermann
Vorname: Oliver
Anschrift: Geibelstr. 44
D-30171 Hannover
Geburtsdatum: 28.01.1978
Geburtsort: Immenstadt/Allgäu

Schulbildung

1984 – 1988 Grundschule Wunstorf
1988 – 1990 Orientierungsstufe OS Nord Wunstorf
1990 – 1997 Gymnasium Hölty – Gymnasium Wunstorf
1997 Abitur

Zivildienst

1998 – 1999 Diakoniestation Bothfeld/List Hannover

Hochschulausbildung

1999 – 2005 Leibniz Universität Hannover
Studiengang Geowissenschaften
Abschluss Diplom- Geowissenschaftler

Berufliche Tätigkeit

2005 – wissenschaftlicher Mitarbeiter am
Institut für Mineralogie der
Leibniz Universität Hannover

Liste der Veröffentlichungen

Stelling, J., Botcharnikov, R. E., **Beermann, O.**, Nowak, M. (2008) Solubility of H₂O- and Chlorine-bearing fluids in basaltic melt of Mount Etna at T=1050-1250°C and P=200 MPa. Chem. Geol. 256, 101-109.

René M., Holtz F., Luo C., **Beermann O.**, Stelling J. (2008) Compositional dependence of biotite on dehydration melting reactions: application to the generation of two-mica granites in the South Bohemian batholith (Bohemian Massif, Czech Republic). Lithos 102, 538-553.